PNL-12154
UC-400

Annual Report 1998
Chemical Structure and Dynamics

Steven D. Colson, Associate Director
Robin S. McDowell, Program Manager
and the Staff of the Chemical Structure and Dynamics Program

March 1999

Prepared for the U.S. Department of Energy
under Contract DE-AC06-76RLO 1830

Pacific Northwest
National Laboratory
Operated by Battelle for the
U.S. Department of Energy

Contents

4. Cluster Models of the Condensed Phase

5. Miscellaneous

6. Appendix

Funding Support

[a] DOE Office of Basic Energy Sciences, Chemical Sciences Division, Fundamental Interactions Branch.

[b] Pacific Northwest National Laboratory (PNNL) Laboratory Directed Research and Development (LDRD).

[c] DOE Environmental Management Science Program (EMSP).

[d] National Science Foundation.

[e] Agency of Industrial Science and Technology, Japan.

[f] Cooperative Research and Development Agreement (CRADA) with the Low Emissions Technology Research and Development Partnership.

[g] EMSL Operations, supported by DOE Office of Biological and Environmental Research.

[h] Department of Energy.

1. Introduction

Purpose

The Chemical Structure and Dynamics (CS&D) program is a major component of the William R. Wiley Environmental Molecular Sciences Laboratory (EMSL), developed by Pacific Northwest National Laboratory (PNNL) to provide a state-of-the-art collaborative facility for studies of chemical structure and dynamics. We respond to the need for a fundamental, molecular-level understanding of chemistry at a wide variety of environmentally important interfaces by (1) extending the experimental characterization and theoretical description of chemical reactions to encompass the effects of condensed media and interfaces; (2) developing a multidisciplinary capability for describing interfacial chemical processes within which the new knowledge generated can be brought to bear on complex phenomena in environmental chemistry and in nuclear waste processing and storage; and (3) developing state-of-the-art analytical methods for characterizing complex materials of the types found in stored wastes and contaminated soils, and for detecting and monitoring trace atmospheric species.

This research effort was initiated in 1989 as a program of rigorous studies of fundamental molecular processes in model systems, such as well-characterized surfaces, single-component solutions, clusters, and biological molecules; and studies of complex systems found in the environment (multispecies, multiphase solutions; solid/liquid, liquid/liquid, and gas/surface interfaces; colloidal dispersions; ultrafine aerosols; and functioning biological systems).

Our program aims at achieving a quantitative understanding of chemical reactions at interfaces and, more generally, in condensed media, comparable to that currently available for gas-phase reactions. This understanding will form the basis for the development of *a priori* theories for predicting macroscopic chemical behavior in condensed and heterogeneous media, which will add significantly to the value of field-scale environmental models, predictions of short- and long-term nuclear waste storage stabilities, and other areas related to the primary missions of the U.S. Department of Energy (DOE).

The CS&D group has particular expertise in the preparation and spectroscopic analysis of molecular clusters (S. D. Colson, D. Ray, S. W. Sharpe, and L. S. Wang); ultrafast and nonlinear optical spectroscopies (D. Ray, G. R. Holtom, and X. Xie); ultrahigh resolution spectroscopy for measurements of electronic and geometric structures and dynamics (S. W. Sharpe and R. S. McDowell); surface and interface structure, chemical reaction dynamics, and kinetics (J. P. Cowin, W. P. Hess, S. A. Joyce, B. D. Kay, and T. M. Orlando); ion-molecule traps and storage technology (S. E. Barlow); and specialized chambers and instruments for chemical reactivity and analysis of atmospheric aerosols (S. E. Barlow and R. S. Disselkamp).

Environmental Problems

Pollution prevention and remediation and restoration of contaminated environments present major scientific challenges because they require information about the relevant chemistry and physics at many scales: from spatial scales of meters to kilometers and temporal scales of days to hundreds of years that are important in the field, to distances of 10^{-10} meters and times on the order of 10^{-12} seconds that are important for processes at the molecular level. Developing the knowledge base needed to address the environmental restoration issues of the DOE, as well as aiding industry in minimizing its environmental impact, requires understanding of the problems at the field scale, identification of the important processes at macroscopic scales, and more detailed insight into mechanisms at microscopic scales (from grain to colloid size) and molecular scales. Our research is focused on the molecular scale in order to develop a fundamental understanding of molecules and their interactions in isolation and in liquids, on surfaces, and at interfaces (condensed media).

The focus of our research is defined primarily by DOE's environmental problems: fate and transport of contaminants in the subsurface environment, processing and storage of waste materials, cellular effects of chemical and radiological insult, and atmospheric chemistry as it relates to air quality and global change. The CS&D program is part of a broader response by EMSL staff and programs to the following problem areas:

Fate and Transport of Contaminants in the Subsurface Environment. Past practices of DOE have resulted in the discharge of chemical and radioactive materials into the environment at many DOE sites, which has resulted in extensive contamination of soils and groundwater. The use of conventional technology to remediate the unique mix of chemical and radioactive wastes at the DOE sites are cost prohibitive, and new technologies are sought to reduce the expense of remediation.

The development of improved technologies for remediating subsurface contamination requires an understanding of the factors that control how fast the contaminants move (mass transport) and their fate (degradation or reaction). At the macroscopic level, hydrologic processes (e.g., fluid flow through porous media) and geologic processes (e.g., sorption on soil particles) play important roles. At this scale, soil composition and heterogeneity have a profound influence on contaminant fate and transport. At the microscopic level it is important to know the speciation of contaminants, that is, the chemical form of the contaminant (e.g., the oxidation state of a metal and whether it is complexed, or whether a contaminant is adsorbed to a surface or not), the mechanisms for changing between different species (adsorption/desorption, redox chemistry, etc.), and the influence of colloidal particles on transport and transformation. Molecular-level studies can provide fundamental understanding and critical information about microscopic mechanisms and macroscopic processes. For example, molecular approaches can provide equilibrium constants, reaction rate coefficients, and transport coefficients that determine the partitioning of contaminants between different phases, their speciation, and the microscopic rates at which equilibrium is attained.

Processing and Storage of Waste Materials. Fifty years of production of defense-related nuclear materials has generated large volumes (hundreds of millions of gallons) of complex wastes that contain large amounts of radioactive materials as well as hazardous chemical wastes. The processing of these mixed wastes is one of the most difficult technical challenges faced by the DOE. Processing tank wastes will require retrieval of the wastes from the underground storage tanks; physical separation of liquids from solids and further processing of solids to remove liquids and soluble compounds; and development of chemical processes to separate specific radionuclides and chemicals from the waste streams as well as to destroy organic compounds. Separations of radionuclides is important to minimize the volume of highly radioactive wastes that will require costly handling and storage. It is also necessary to remove species that may inhibit the formation of a durable waste form or may generate toxic, difficult-to-handle off-gases (e.g., sulfates, halogens, NO_x, and volatile metals such as Cs, Pb, Hg, Rb, Bi, Cd, Ag, and As). Molecular-level studies will provide fundamental information about the factors that control the binding of ionic species (e.g., metal cations, metal-oxide anions, etc.) to sequestering agents. This fundamental information will provide the basis for the design of new agents and new processes for selective and efficient separations.

The long-term storage of much of the tank waste will require converting it to a durable solid form. The waste form must be able to dissolve substantial quantities of wastes without significant loss of durability; it must immobilize hazardous materials for hundreds to thousands of years and be resistant to leaching by water. Most disposal options for the tank wastes use glass as the final waste form. There are still unanswered questions about the best formulation of the glass to meet these requirements. The high variability of the composition of the tank wastes provides a major challenge, since one formulation may not work for all waste streams, although that is the current baseline assumption. Fundamental understanding of the mechanisms of network forming in amorphous materials and of glass dissolution will provide the basis for design of new glass formulations with desired properties. Molecular-level knowledge of the binding of contaminant species in glass, and the polymerization and depolymerization reactions important in glass melts and in the dissolution mechanism will provide insight into the chemistry of these systems that will improve our understanding of the microscopic mechanisms responsible for phenomena such as phase separation, enhanced dissolution with ionic aqueous solutions, etc.

Cellular Effects of Chemical and Radiological Insult. Development of science-based human and environmental health guidelines requires a comprehensive understanding of the response of human cells to insults from radioactive and toxic chemicals. There is thus a critical need for fundamental data on health effects as an integral component of managing waste cleanup activities. In the past, animal and tissue studies furnished the primary basis for understanding the adverse health effects of toxic materials and for establishing regulatory guidelines. A new generation of risk assessment will require a fundamental understanding of crucial cellular mechanisms and processes at the molecular level to provide a more accurate evaluation of risk and the establishment of genuinely protective statutes and standards. This mechanistic extension is required for both accurate extrapolations at high dose levels in animal studies and the low exposure/dose levels needed to set regulatory guidelines for humans. The EMSL focus in this effort is to provide the structural basis at the molecular and cellular level for the mechanisms. To address these problems we have initiated research in cellular processes involved in genomic protection, cellular response to chemical insults, and mechanistic investigations for the basis of bioremediation. The specific research areas include: The Structural Basis for DNA Damage Recognition; Functional Micro-Spectroscopy of Live Single Mammalian Cells; and Structural and Mechanistic Investigations of Proteins Involved in Bioremediation.

The critical research tools, many of which are unique to the EMSL, are high-field liquid and solid state NMR, EPR, high field Fourier-transform ion cyclotron resonance mass spectrometry, laser spectroscopy, novel microscopies, and advanced computational capabilities.

Atmospheric Chemistry. Understanding tropospheric chemistry is key to DOE's response to national concerns about global change and the effects of energy production and use on air quality. Major public concerns include tropospheric ozone levels, decreased visibility due to haze, health effects due to inhalation of particulate matter and oxidants, and climate change (global warming) due to modification of the radiative properties of the atmosphere. The development of emissions standards and rational control strategies requires a detailed knowledge of the physical and chemical processes at work in the atmosphere. The earth's atmosphere is complex, consisting of a multiphase mixture of gases, liquid cloud and precipitation droplets, solid ice crystals, and liquid and solid aerosols. Even though gas-phase processes in the atmosphere have been extensively studied, a number of significant unanswered questions remain. For example, the mechanisms of oxidant formation in the troposphere remain uncertain and the tropospheric chemistry of naturally occurring (e.g. terpenes) and anthropogenic organics are poorly understood. The role of heterogeneous atmospheric processes are even more poorly understood; for example, heterogeneous processes are now known to play an important role in acid rain formation and Antarctic ozone depletion, but they are not understood quantitatively, and the role of heterogeneous processes on oxidant and aerosol formation in the troposphere is even less well understood. The lack of a fundamental molecular-level understanding of important atmospheric processes greatly limits our ability to model the impacts of emissions on atmospheric chemistry, air pollution, and global change, and to design effective control strategies that have minimal impact on human activities.

The EMSL program in atmospheric sciences focuses on the molecular chemistry of tropospheric oxidants and aerosols, research areas with significant impact on all of the major atmospheric quality factors. The research approach has strong, integrated efforts in both experimental and computational chemistry. Important research areas include condensed-phase chemistry, gas-phase–aerosol interactions, and gas-phase chemistry.

Although the primary focus of the research program is on understanding the role of emissions on tropospheric chemistry, the fundamental knowledge gained from this research will have an impact on problems such as ozone depletion in the stratosphere, halohydrocarbon effects on tropospheric and stratospheric chemistry, and on other atmospheric issues related to economic and human health.

Problem Selection for Impact on Environmental Needs

Care must be taken in the selection of the systems to be studied and the types of information that need to be obtained in designing a fundamental science program which is expected to impact specific applications. It is generally not sufficient just to do the correct *type* of fundamental science research (e.g., surface chemistry, interfacial chemistry, development of sensitive spectroscopies, etc.), but the data and understanding themselves must be responsive to specific environmental needs. Thus, we use a combination of several approaches to making these selections.

Multidisciplinary Collaborations: Establishing collaborations with those working more directly on environmental problems is one of the most direct ways to select the most impactful research projects. An example is Thom Orlando's research aimed at providing the DOE with information needed to move old fuel rods from a water storage basin to dry storage. There is a concern about the radiolytic generation of gases (hydrogen and oxygen) from residual water. This collaboration helped focus our DOE work on radiochemistry mechanisms and yields for water on oxidized surfaces. There are numerous similar examples.

Materials Chemistry Selection: Often it can be established that particular chemical process in or on particular materials are of broad importance. Most environmental materials are found in an oxidized form. Hence, the emphasis on the structure and chemistry of oxide materials, particularly when in contact with water. Furthermore, the emphasis must be on naturally occurring oxides (minerals or models of minerals such as silicon, aluminum, and iron oxides) or materials important to energy-related environmental problems (e.g., ZrO cladding of fuel rods). This understanding leads to the design of the solid/liquid and gas/solid interfacial chemistry components of our program.

Chemical Processes Selection: In some cases, the types of chemical processes that are important to addressing environmental needs have not been addressed in the past with sufficient accuracy and detail, or for the correct systems. For example, the design of separations agents for removal of radioactive elements from complex solutions demands a simultaneous understanding of the kinetics and energetics of solvation, complexation, and transport between different fluids for specific elements with specific ligands in specific fluids. The treatment of similar processes with idealized species in simple (atomic) fluids is generally inadequate. This analysis led to the selection of the chemical processes and systems for study in our work on molecular process in liquids and on liquid interfacial chemistry and dynamics.

Capabilities Development: One reason for the current lack of important information is that the demands derived from environmental needs often exceed the present state-of-the-art. The level of theoretical precision for treating complex systems must be advanced. The theoretical approach for treating new materials must be evaluated, requiring benchmarking calculations and experimental data. The existing tools for physical and chemical characterization of materials have been developed around the study of conducting, not insulating oxide, materials. Examples such as these have led to our work on model systems (e.g., clusters) and on methods development which provides the underpinning for the remainder of the DOE program. As an important added advantage, the methods development work enables the broader scientific community to join with the EMSL scientists in addressing DOE's environmental problems by using or building upon these new methods and capabilities.

Principal Research Areas

Molecular Processes in Clusters and Liquids. Research in this area is aimed at providing a molecular-level understanding of solvation and reactions in simple and complex fluids as they relate to remediation of complex wastes and contaminated soils and ground water. A common element in these environmental problem areas is the need to understand molecular processes in aqueous solutions. Model systems, such as molecular clusters and solid amorphous water, provide an opportunity for detailed studies of solvation and the effects of solvation on chemical reactivity, and can provide information about intermolecular interactions that lay the foundation for accurate modeling of solution processes. Studies in this area provide detailed information about the factors controlling the rates of reactions in solution that are important for the fate of contaminants in aqueous environments, and information about the factors influencing the selectivity of ligands for specific ions that is important in developing separations agents for use in waste processing.

Liquid Interfacial Chemistry and Dynamics. Another common element in the environmental problem areas is the need to understand molecular processes at the interface between aqueous solutions and different organic solutions. Some separation processes for tank waste materials use organic liquids to extract species from the aqueous waste solutions. The efficiency of separation process in binary liquids can be significantly influenced by molecular processes occurring at the liquid–liquid interface, such as the interface activity of the separation agent. Molecular processes occurring at liquid–liquid interfaces can also play important roles in the transport of contaminants from organic solvents (such as chlorinated hydrocarbons) into groundwater. This is a newer element of our program, and is driven by the need to develop fundamental molecular information that will improve waste separations processes and provide knowledge about the partitioning of waste species in different organic and aqueous phases in soils contaminated with organic liquids.

Solid/Liquid and Gas/Solid Interfacial Processes. It is also crucial to understand molecular processes at the interface between aqueous solutions and environmentally important materials, such as aerosols, minerals, and glasses, as these are central to addressing fundamental science needs related to contaminant fate and transport and waste immobilization. The adsorption of contaminants on and incorporation in minerals in the soil can affect the transport of contaminants in the subsurface environment. Mineral interfaces can also enhance reactivity (e.g., environmental catalysis), leading to the degradation or transformation of contaminants. A knowledge of molecular processes at solid/liquid interfaces is also important for understanding the stability of glasses proposed for encapsulating high-level radioactive wastes. Over the long half-lives of the radionuclides, nuclear waste glasses that come into contact with water can dissolve, resulting in release of radioactive material into the environment.

Energetic Processes in Condensed Phases. This research area focuses on obtaining a mechanistic understanding of chemical transformations of molecules and materials, be they driven by thermal, radioactive, or optical sources. Energetic processes are important in the degradation of nuclear waste glasses from radiolytic decay, and can drive chemistry occurring in solid and liquid phases of tank wasters. The use of laser techniques for the characterization of waste materials relies on an understanding of molecular processes driven by optical sources.

Aerosol Photochemistry. Understanding the processes that control the loading, geographical distribution, and chemical and physical properties of anthropogenic atmospheric aerosols is a basic problem of atmospheric chemistry and is central to key environmental issues affecting the nation's energy economy. There is an emphasis in EMSL on molecular processes in the gas phase and at gas/liquid and gas/solid interfaces (droplets and aerosols). Our instrumentation and computational capability have also been developed to support investigations of gas-phase and interfacial processes, which are known to provide unique computational and experimental challenges. Examples of techniques that have been developed for these purposes include interfacial second harmonic generation, an analytical method in which the entire signal arises from interfacial molecules, providing information on the thermodynamic driving forces that determine the rates of transport of gas phase atmospheric species into aqueous solutions representing rain drops or heavily hydrated aerosols; and development of a novel free-jet reactor, which can quantitatively measure gaseous products resulting from aerosol surface reactions over a wide range of temperatures and pressures. Apparatus is also being developed to obtain IR absorption spectra and mass spectra of gaseous species resulting from the reactions of atmospheric gases with selected solids and solutions, which will allow measurements of the rates and products of interfacial reactions of atmospheric gases as a function of the composition and phase of the substrate material. A temperature-controlled aerosol chamber will also be installed in which these same reactions can be studied on aerosol particles themselves. The advantage of this combined approach is that the composition and phase of the model solids and solutions can be controlled with greater precision than can the properties of aerosol particles, providing a sound basis for the interpretation of the direct aerosol reaction studies.

Molecular-Level Studies of Biological Systems. Recent advances in fluorescence microscopy, including those made at PNNL, have made it possible not only to detect single molecules at room temperature, but also to conduct spectroscopic measurement and monitor dynamical processes on single molecules. Recently we have also demonstrated fluorescence imaging of single molecules by two-photon excitation with a femtosecond Ti:sapphire laser, which has the advantages that the excitation volume is small, the penetration is deep, and photodamage can be reduced for biological samples. This offers the opportunity of viewing chemical reactions in a living cell in real time. Recently, the crystal structures of many membrane proteins, such as light-harvesting proteins and reaction-center proteins, have been solved. In contrast, our knowledge of how these proteins are assembled in the membrane is extremely limited. The formation of the photosynthetic membrane during cell growth has never been directly monitored on a single-cell basis, and the mechanism for formation of other membrane proteins is also unknown. The advantage of photosynthetic proteins is that they have naturally fluorescent chromophores with distinct spectroscopic identities that can be followed by optical measurements. Previous spectroscopic measurements of photosynthetic bacterial growth have been done on large ensembles of cells. These averaged results often preclude detailed information due to cell heterogeneity. Single-cell measurements are likely to produce new information otherwise hidden, and will open up many exciting possibilities for probing cellular processes.

Capabilities Development. This area of research is an enabling activity required to keep the experimental programs working effectively at the state of the science.

1998

During 1998 the group has settled into the new EMSL laboratories, and the research programs have continued with minimal impact from the move, as evidenced by the progress summaries that follow, and the continuing production of quality research and publications.

Two personnel changes have occurred this year in the relatively stable group of CS&D staff. Doug Ray accepted the position of EMSL Deputy Director, and will reduce his research activities in CS&D. Effective Jan. 1, 1999, Sunney Xie was named Professor of Chemistry at Harvard University; he will continue here through the spring to insure a smooth transition for his group.

Web Addresses

Pacific Northwest National Laboratory:
http://www.pnl.gov
William R. Wiley Environmental Molecular Sciences Laboratory:
http://www.emsl.pnl.gov

2. Reaction Mechanisms at Interfaces

Structure and Reactivity of Ice Surfaces and Interfaces

K. P. Stevenson, Z. Dohnalek,**
R. L. Ciolli,† G. A. Kimmel,
R. S. Smith, and B. D. Kay

Supported by DOE Office of Basic Energy Sciences.

*Postdoctoral Research Associate.
†AWU Undergraduate Student.

Amorphous materials are important in a variety of scientific disciplines such as chemistry, physics, materials science, and biology. Amorphous solid water (ASW) is of special importance for many reasons, including the open question over its applicability as a model for liquid water, and fundamental interest in the properties of glassy materials.[1] In addition to the properties of ASW itself, understanding the microscopic intermolecular interactions between ASW and an adsorbate is important in such diverse areas as solvation in aqueous solutions, cryobiology, and desorption phenomena in cometary and interstellar ices.[2]

1. Controlling the Morphology of Amorphous Solid Water

The growth and annealing temperatures are well known to strongly influence the physical properties of ASW. Nevertheless, conflicting results have been reported for such fundamental properties as the surface area, density, and porosity of ASW, and remain unresolved. We have investigated the morphology of thin ASW films deposited by two different methods: from highly collimated, effusive H_2O beams, and from ambient vapor.

The ASW films were characterized by their saturation coverage of N_2 at 26 K, measured by integrating the N_2 TPD lineshapes obtained with a quadrupole mass spectrometer. The information obtained is analogous to that from N_2 Brunauer–Emmett–Teller (BET) isotherm measurements, but allows ASW films to be studied at temperatures much lower than 77 K. The N_2 gas was deposited normal to the surface using a supersonic beam that was smaller than, and centered on, the umbra of the ASW film. The N_2 uptake was independent of incident angle. At 26 K, the N_2 will adsorb on the surface of the ASW and in pores, but it will not form multilayers on a flat surface. We have experimentally verified that N_2 diffusion on the surface and through the pores of the ASW deposit is very rapid, ensuring uniform coverage of the film. The curvature of the pores locally reduces the N_2 vapor pressure, allowing multilayer adsorption (capillary condensation) in pores below some maximum radius. Therefore, the amount of N_2 adsorption is a measure of the accessible surface area and pore volume of the film. Water deposited at temperatures above 140 K resulted in nonporous crystalline ice. The area of the monolayer N_2 TPD signal from crystalline ice was used as a reference state for normalizing the N_2 adsorption in ASW.

Figure 2.1 shows the amount of N_2 adsorbed by 50-BL ASW films grown at 22 K on Pt(111) versus

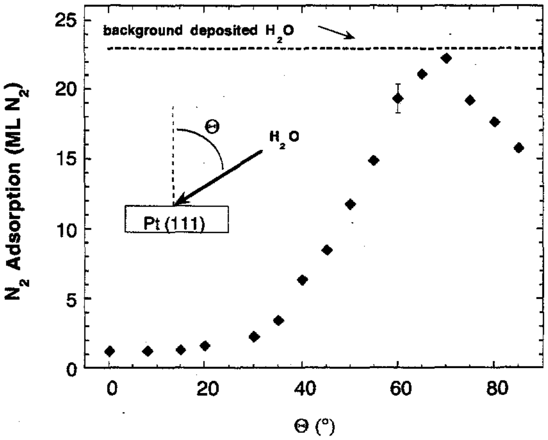

Figure 2.1. Amount of N_2 adsorbed by ASW films versus Θ, the angle between the incident H_2O beam and the Pt(111) surface normal. The films, which were nominally 50 BL thick, were deposited at 22 K. The "film thickness" corresponds to the number of bilayers that each film would have if it were grown as a nonporous crystal. The actual height of the film depends on the number of bilayers and the density, which varies with the deposition angle. The solid diamonds represent ASW films grown using a collimated, effusive H_2O molecular beam. The dashed line shows the amount of N_2 adsorbed by a 50-BL ASW film grown at 22 K from a random background flux formed by controlling the H_2O partial pressure in the vacuum chamber.

the deposition angle, Θ. The N_2 adsorption by ASW films grown with $\theta \leq 20°$was similar to a crystalline ice film. However for $\theta > 30°$, the amount of N_2 adsorbed by the ASW increased dramatically, reaching a maximum near $\Theta = 70°$. At the maximum, the ASW films adsorb more than 20 times as much N_2 as a crystalline ice film. The quantity of N_2 adsorbed by the ASW is much greater than would be expected from a simple roughening of the surface, and indicates the formation of a porous film. We have also investigated ASW films grown by filling the experimental chamber with water vapor (background dosing). In that case, the flux of water molecules striking the surface has a cosine angular distribution. As indicated by the dashed line shown in Fig. 2.1, the large N_2 adsorption for ASW grown by background dosing is indicative of a highly porous film and is most comparable to that obtained for ASW grown at oblique angles. Results similar to those shown in Fig. 2.1 were obtained for O_2 and Ar adsorbed on ASW films, indicating that the ability to adsorb large quantities of gas depends primarily on the morphology of the ASW. It is well known that the porosity of ASW and its ability to trap volatile gases depends on the growth and annealing temperatures. However, the data in Fig. 2.1 show that the porosity and morphology of ASW are also strongly dependent on the angular distribution of the incident water molecules.

We estimate the ratio of N_2 molecules adsorbed to water molecules deposited in the ASW films at $\Theta = 70°$ or by background dosing to be 1:2. This ratio is consistent with volume filling of pores by capillary condensation, and yields a density of ~0.6 g/cm^3 for the ASW film, in good agreement with earlier results. In addition, the N_2 TPD lineshapes show evidence of capillary condensation (data not shown). ASW films grown at higher temperatures or at normal incidence have densities as high as 0.93 g/cm^3. The decrease in N_2 adsorption for $\Theta > 70°$ may result from the formation of larger pores that can no longer be filled by capillary condensation at 26 K. Alternatively, the ASW structures grown at very oblique angles may be structurally weak, leading to some collapse of the films.

Figure 2.2 shows the N_2 adsorption of ASW grown at 22 K versus film thickness for various deposition angles. For off-normal deposition angles, the N_2 adsorption increases approximately linearly with film thickness.

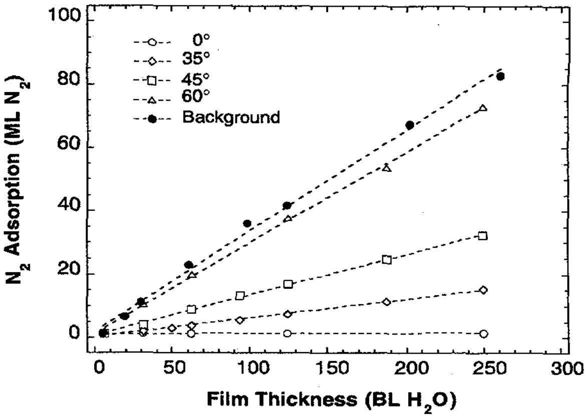

Figure 2.2. Amount of N_2 adsorbed by ASW films versus film thickness. The films were deposited at 22 K. Open symbols represent ASW films deposited by collimated beams with $\Theta = 0°, 35°, 45°$, and 60°. The filled circles represent the ASW films grown using background H_2O dosing. Fitted lines show a linear increase in N_2 uptake with increasing film thickness.

The adsorption of N_2 by the ASW films grown by background dosing is greater than that of the corresponding ASW films grown with collimated beams. The linear increase in N_2 adsorption, in conjunction with the magnitude of the adsorption, suggests that the pore structure in the ASW films is highly connected, allowing the N_2 to diffuse throughout the ASW film. In contrast, the amount of N_2 adsorption on ASW films grown at normal incidence is nearly independent of film thickness and similar to the amount of N_2 adsorption on the clean Pt(111) substrate, indicating denser films without a connected network of pores. In this case, N_2 adsorption occurs primarily on the external surface of the film.

We also measured the N_2 adsorption by 50-BL ASW films as a function of the sample temperature during H_2O deposition (Fig. 2.3). In all cases, N_2 adsorption by the ASW films decreases with increasing surface temperature. For ASW films grown at or near normal incidence, the decrease in N_2 adsorption versus temperature is small—these films are nonporous, independent of growth temperature. However, for ASW films grown at oblique angles or by background dosing, the porosity and the N_2 adsorption are strongly dependent on temperature. Above approximately 90 K, all ASW films, independent of the angular distribution of the incident water molecules, have essentially the same N_2 adsorption as the crystal-

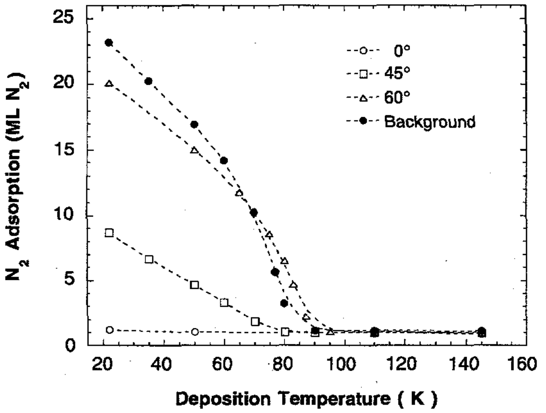

Figure 2.3. Amount of N_2 adsorbed versus growth temperature for 50-BL ASW films. Open symbols reflect ASW films deposited by collimated beams with $\Theta = 0°$, 45°, and 60°. The filled circles represent the ASW films grown using background H_2O dosing. The dotted lines through the data are to guide the eye. For the thin films and low deposition rates used in these experiments, the ASW film temperature and the Pt(111) temperature are essentially identical ($\Delta T << 0.1$ K).

line reference state at 140 K. We have also found that the porosity of ASW films grown at 22 K depends on the annealing temperature and time, in agreement with earlier reports that annealing reduces the porosity of ASW.

The data in Fig. 2.3 show that the morphology of vapor-deposited ASW is a complicated function of both the temperature and the angular distribution of the incident water molecules. In addition to these variables, the morphology of ASW may also depend on the whether the water beam is supersonic or effusive. Using supersonic expansions, which leads to water cluster formation in the beam, apparently produces porous ASW even at normal angles of incidence.

Typically, BET isotherm measurements made with N_2 at ~77 K have been used to characterize the apparent surface area of ASW. However, since the porosity is a very sensitive function of the thermal history of the ASW, BET measurements should not be used to study the very fragile, low-temperature deposits. Fig. 2.3 shows that the porosity of ASW at low temperatures can be substantially higher than at 77 K. Furthermore, since the slope of the curves in Fig. 2.3 is non-zero at the lowest temperature of this study, ASW films grown at temperatures below 22 K are likely to have even greater porosity. For ASW films grown by background dosing, the amount of N_2 adsorbed corresponds to an apparent surface area of ~2700 m^2/g at 22 K and ~640 m^2/g at 77 K. Mayer and Pletzer[3] obtained a value of ~420 m^2/g at 77 K using standard BET techniques. The large apparent surface areas we observe at low temperatures and oblique angles of incidence result from both large internal surface areas and N_2 multilayer formation in the pores of the ASW film.

Our observations can be qualitatively understood using a simple physical picture based on ballistic deposition.[4] For ballistic-deposition simulations of surface growth, randomly positioned particles are brought to a surface with straight-line trajectories, and the particles stop as soon as they encounter an occupied site ("hit and stick"). These models lead to the formation of porous films whose morphology is strongly dependent on the angle of deposition of the particles. For off-normal deposition angles, regions that are initially thicker by random chance have higher growth rates and shadow the regions behind, leading to the formation of a porous film. The shadowing effect increases as the angle of incidence increases. In these models, the density decreases with the angle of incidence, in qualitative agreement with our experimental observations at low temperatures. For background dosing, the shadowing effect also leads to porous films with a different pore structure. The densification observed with increasing growth and/or annealing temperatures is a result of increased surface and bulk diffusion of the water molecules. Quantitative understanding of this diffusive behavior requires detailed molecular level information such as that provided by molecular dynamics simulations.

Controlling the morphology of ASW by the method of deposition has important implications for experimental studies concerning the physical and chemical properties of ASW. In astrophysical environments, the morphology of ASW will depend on whether it forms from a directional or a diffuse source of water vapor. Directional deposition may occur, for example, in the rings of Saturn, where it has been proposed that water molecules sputtered from the outer rings accumulate on the inner rings. Directional deposition of ASW can also occur when a particle or body is passing through a water cloud with a large relative velocity. In other cases, such as the formation of comets, porous ASW may result when omni-directional deposition of the water molecules occurs.

2. *Substrate-Induced Crystallization of Amorphous Solid Water at Low Temperatures*

The crystallization of ASW, which is an important process in the thermal aging and outgassing of icy bodies in outer space, has been studied previously.[5,6] These studies indicate that the crystallization of ASW on heterogeneous substrates occurs via a bulk nucleation and growth mechanism.[5] Therefore, these substrates do not act as nucleation sites for crystallization during deposition or during the annealing of the ice film. However, the role of crystalline ice (CI) as a substrate in promoting the ASW crystallization is unclear. We show that water deposited at low temperatures (<110 K) and slow deposition rates (<0.1 bilayer/s) on CI is amorphous, and the CI substrate acts as a nucleation site for the subsequent crystallization of the amorphous phase upon heating. We find that at 128 K the crystallization time for 10 bilayers (BL) of ASW deposited on CI is ~1000 times shorter than the crystallization time for ASW deposited on Pt(111). These changes of the ASW surface crystallinity occur at temperatures below those where any appreciable water desorption occurs, and were monitored using a new surface-sensitive N_2 desorption "spectroscopy," which is described below.

The H_2O TPD spectra from 25 BL of H_2O deposited on Pt(111) at different substrate temperatures are shown in Fig. 2.4. Fig. 2.4a represents the TPD from the film deposited at 22 K. Low-temperature growth results in the formation of ASW, as shown in previous studies. The characteristic feature of the amorphous phase in the desorption spectrum is the presence of a shoulder at ~158 K due to the higher desorption rate of ASW as compared to CI phase (Fig. 2.4b). The difference between the ASW and CI desorption rates is more easily seen in the inset of Fig. 2.4. The higher desorption rate of ASW is a consequence of its metastable character, and hence its higher free energy. As the crystallization of the ASW film occurs (157–160 K), the H_2O desorption rate decreases to the desorption rate of CI, and follows the zero-order desorption dependence for higher temperatures.

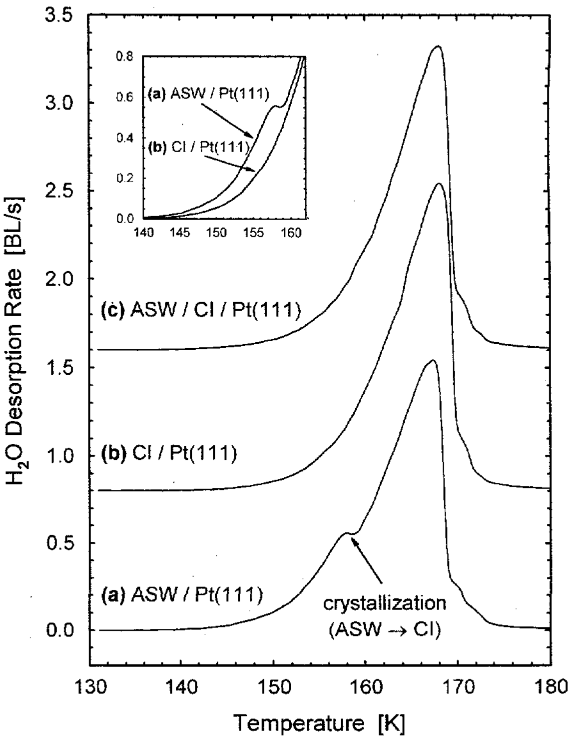

Figure 2.4. The H_2O TPD spectra from the H_2O films deposited on a Pt(111) substrate at different temperatures. (a) 25 BL deposited at 22 K (ASW), (b) 25 BL deposited at 140 K (CI), (c) 15 BL deposited at 140 K (CI) followed by 10 BL deposited at 22 K (ASW). The spectra are offset for clarity. The inset shows a superposition of spectra (a) and (b) to indicate the higher desorption rate of ASW compared to CI.

Since the H_2O TPD clearly distinguishes between ASW and CI, we have used it to investigate the affect of a CI substrate on the subsequent growth of low-temperature-vapor-deposited ice. Figure 2.4c shows the H_2O desorption spectrum from a thin film prepared by the initial deposition of 15 BL of H_2O at 140 K to form a CI base, followed by the deposition of 10 additional bilayers of H_2O at 22 K. Despite the fact that the H_2O deposition at 22 K is expected to result in the formation of an ASW film, the low desorption rate in the H_2O TPD shows only the presence of CI phase, analogous to the spectrum of CI film in Fig. 2.4b. However, as mentioned earlier, two explanations are possible: (1) the CI substrate acts as a template for the subsequent growth of crystalline ice during low temperature deposition, or (2) the low temperature vapor deposited ice overlayer is amorphous, but the CI substrate acts as a nucleation site, thereby accelerating the crystallization of the ASW overlayer. The limitation of H_2O TPD for investigating the crystallization in this case is that prior to the temperatures where desorption becomes appreciable (>140 K), significant crystallization may have occurred. To avoid the high temperature annealing of the ASW layer we utilize a surface-sensitive method that is based on the low temperature desorption of N_2 monolayers physisorbed on H_2O surfaces.

The N_2 TPD spectra from the surfaces of the H_2O films described in Fig. 2.4 are shown in Fig. 2.5. After the deposition of the ice films, the sample temperature was set to 26.5 K and the ice films were exposed to the N_2 beam until a saturation (monolayer) coverage was achieved. The N_2 desorption spectra from ASW (Fig. 2.5a) and CI (Fig. 2.5b) are readily distinguished. Two significant differences are observed: (1) the maximum of the desorption peak shifts from 31.5 K for ASW to 35.5 K for CI, and (2) the integrated N_2 TPD area from the CI surface decreases by ~30% compared to that of ASW. The shift in the peak desorption temperature suggests that the physisorbed N_2 has a slightly higher binding energy on the CI surface as compared to the ASW surface. The higher surface area of the ASW film may be attributed to the formation of slightly rougher surfaces due to significantly slower H_2O surface diffusion at low temperatures.

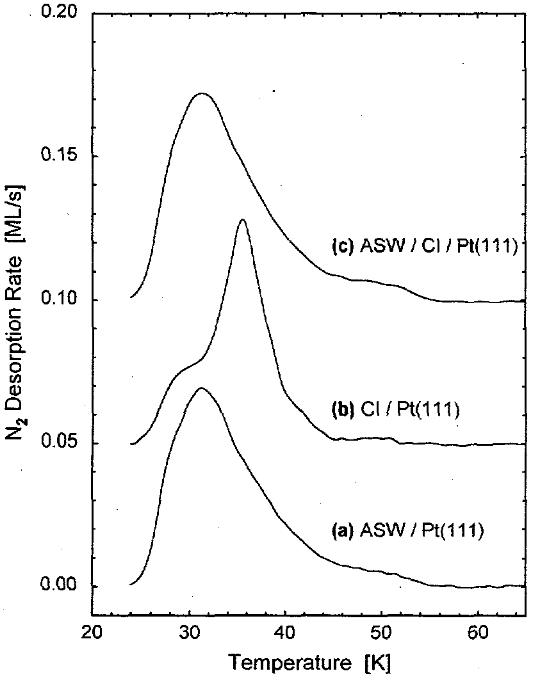

Figure 2.5. The N_2 TPD spectra from 1 ML of N_2 physisorbed on 25 BL of H_2O adsorbed at different temperatures as described in Fig. 2.4. (a) 25 BL deposited at 22 K (ASW), (b) 25 BL deposited at 140 K (CI), (c) 15 BL deposited at 140 K (CI) followed by 10 BL deposited at 22 K (ASW). The spectra are offset for clarity.

As shown in Fig. 2.5c, the N_2 desorption from a 10-BL H_2O film grown at 22 K on a 15-BL CI substrate yields a desorption spectrum that is identical to the spectrum from the ASW film grown at 22 K on Pt(111) (Fig. 2.5a). This is in contrast with the result presented in Fig. 2.4c, which shows the H_2O desorption rate corresponding to that of the CI phase. Based on the similarity of Fig. 2.5c and Fig. 2.5a, we conclude that the H_2O film deposited on the CI substrate at 22 K is amorphous. We have also investigated the growth of H_2O overlayers at higher temperatures. The N_2 desorption spectra indicate that for temperatures less than ~110 K the films deposited on CI are amorphous as well. The subsequent crystallization of the ASW is accelerated by the presence of the CI substrate, and occurs at a temperature below the onset of any appreciable H_2O desorption (T < 140 K), as confirmed by Fig. 2.4c.

As illustrated in Fig. 2.6 the N_2 TPD lineshape can be used to determine the crystallinity of the ASW surface as a function of annealing time. For this data, a 10-BL ASW film was deposited on 15 BL of CI and subsequently annealed at 128 K for a period of time, after which it was cooled to 26.5 K, dosed with a monolayer of N_2, and then heated to obtain the N_2 TPD spectrum. The same film was then further annealed at 128 K and the process was repeated. In this way, a series of N_2 TPD spectra was obtained for partially crystallized surfaces. The complete set of spectra in Fig. 2.6a demonstrate a decrease in the intensity of ASW peak (~31.5 K) and an increase in the intensity of CI peak (~35.5 K) with increasing annealing time, showing the gradual crystallization of the surface. All the spectra intersect at a single isobestic point (~33.5 K) that is generally associated with the existence of two interconvertible species which have overlapping spectra. Therefore the N_2 TPD spectra of partially crystallized surfaces can be expressed as a linear combination of the ASW and CI spectra weighted by their corresponding fractions:

$$s(T,\chi) = (1-\chi)\, s_{ASW}(T) + \chi\, s_{CI}(T),$$

where s_{ASW} and s_{CI} represent the temperature-dependent spectra of the ASW (Fig. 2.6b) and CI (Fig. 2.6c) surfaces, respectively, and χ is the frac-

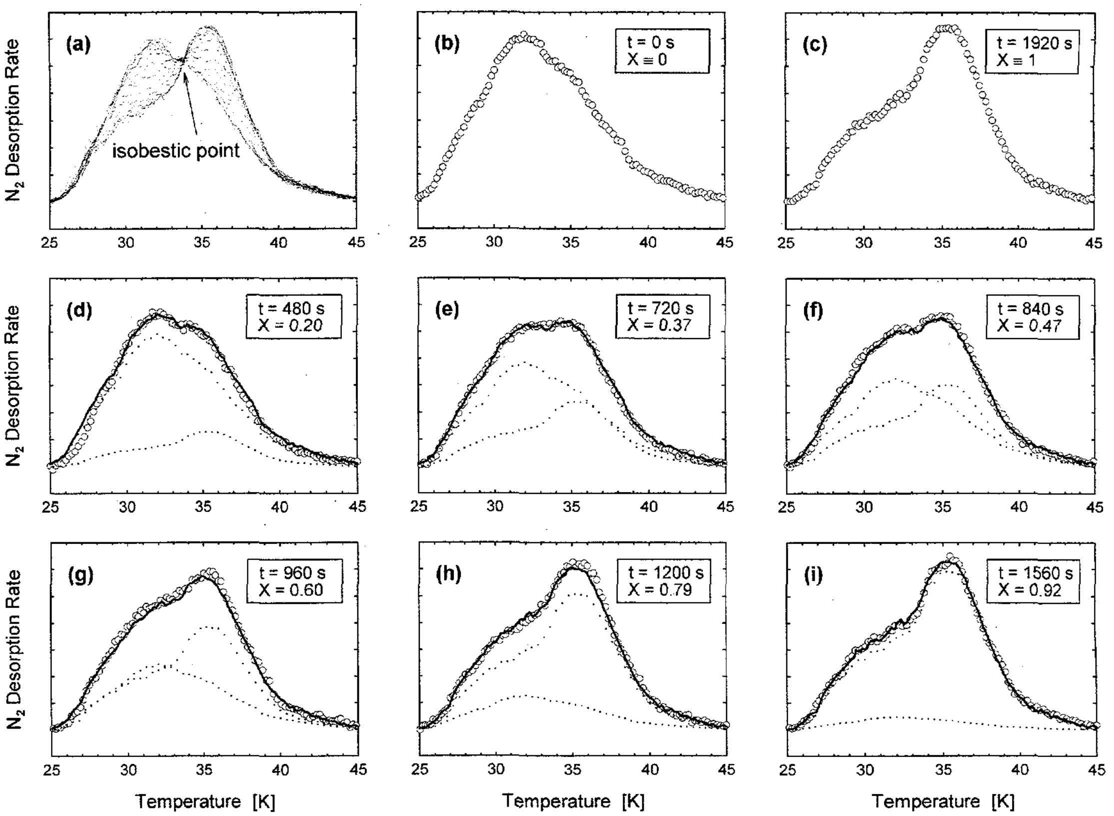

Figure 2.6. The N_2 TPD from 1 ML of N_2 adsorbed at 26.5 ± 0.5 K on the H_2O film prepared as described in Fig. 2.4c (10 BL of ASW/15 BL of CI/Pt(111)) as a function of annealing time at 128 K. Fig. 2.6a shows the set of N_2 TPD spectra vs. annealing time, exhibiting an isobestic point at ~ 33.5 K. In the Figs. 2.6b–i, the open circles represent the experimental points, solid lines represent the fit of spectra by a linear combination of the initial (Fig. 2.6b) and final (Fig. 2.6c) spectra with their partial fractions shown as dotted lines.

tional area of the surface corresponding to the CI spectrum in Fig. 2.6c. Figures 2.6d–i show the fits (solid lines) to the experimental data (open circles) as well as the partial fractions (dotted lines) of the crystalline and amorphous spectra for a representative subset of measurements. Excellent agreement is found between the fits and the data, demonstrating that N_2 TPD provides a sensitive method for the quantitatively study of the crystallization of ASW surfaces.

The comparison of the N_2 TPD spectra of the film crystallized at 128 K (Fig. 2.6c) and the CI film grown at 140 K (Fig. 2.5b) shows a significant decrease in the intensity of the low temperature shoulder (~30 K) for the ice grown at 140 K. The differences in the spectra suggest that the CI grown at 140 K is more ordered than the CI obtained by annealing at 128 K. This observation is consistent with previous studies, which suggest that CI produced by annealing ASW in this temperature range has a significant amorphous component.

The converted surface fraction, $\chi(t)$, of ASW films (10 BL) on CI (open circles) and Pt(111) (filled circles) substrates as a function of annealing time at 128 K is shown in Fig. 2.7. The crystallization of ASW film on a CI substrate shows a dramatic acceleration compared to the crystallization of ASW on Pt(111) substrate. Only small changes in the converted fraction (<0.10) of the ASW film on Pt(111) are observed within the time that leads to complete crystallization of the ASW film on the CI substrate. We estimate that the crystallization of 10 BL at 128 K would take ~1000 times longer compared to the crystallization of 10 BL of ASW on the CI substrate.

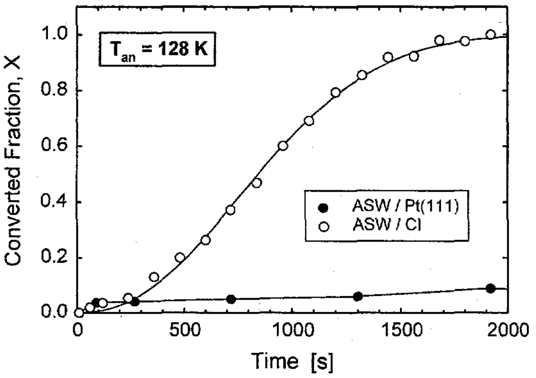

Figure 2.7. The isothermal crystallization of the surface of 10-BL thick ASW film on CI (open circles) and Pt(111) (filled circles) substrates at 128 K. Solid lines are provided to guide the eye.

In general, during the crystallization two processes occur: (1) formation of the nucleation embryos, and (2) their subsequent growth. Each step is associated with a kinetic barrier towards the formation of the thermodynamically favored crystalline phase. The increase of the crystallization rate observed on the CI substrate is attributed to the fact that the CI substrate acts as a 2-dimensional nucleation center. Hence, the crystallization rate is determined by the rate of propagation of the ASW/CI interface (i.e. the growth of the crystalline phase).

The converted fraction as a function of time, $\chi(t)$, (Fig. 2.7) gives us valuable information about the crystallization process. If the ASW/CI interface propagated layer by layer through the film, then $\chi(t)$ would be a step function. Instead, $\chi(t)$ is significantly broadened, suggesting that the ASW/CI interface is rough. Some of the width of $\chi(t)$ may be due to initial roughness of the CI substrate and/or the ASW overlayer. However, the width of $\chi(t)$ probably also has contributions from stochastic roughening of the interface as the crystallization proceeds. We are currently conducting further experiments on the thickness and temperature dependence as well as simulations to investigate these issues and to extract the activation energy for the growth of the crystalline phase.

In summary, we have used N_2 TPD from a monolayer of N_2 physisorbed on H_2O surfaces to investigate the crystallization of amorphous solid water (ASW) at low temperatures. The changes in the N_2 desorption spectra are directly proportional to the changes in the crystallized fraction of the ASW surface. The H_2O films deposited on crystalline ice (CI) substrate at temperatures below ~110 K are amorphous. Upon annealing, the CI substrate acts as a 2-dimensional nucleus for ASW crystallization, and hence the crystallization is not limited by the kinetic barrier associated with the formation of bulk nucleation embryos as on heterogeneous substrates. Instead the crystallization rate is limited only by the barrier associated with the propagation of the ASW/CI interface. This results in a dramatic increase of the crystallization rate (~1000 times at 128 K) of ultrathin (10 BL) ASW film deposited on CI compared to the rate of bulk crystallization observed for the film deposited directly on a Pt(111) substrate.

References

1. P. G. Debenedetti, *Metastable Liquids: Concepts and Principles* (Princeton University Press, 1996).
2. R. S. Smith, C. Huang, E. K. L. Wong, and B. D. Kay, *Phys. Rev. Lett.* **79,** 909 (1997).
3. E. Mayer and R. Pletzer, *Nature* **319,** 298 (1986).
4. A. L. Barabasi and H. E. Stanley, *Fractal Concepts in Surface Growth* (Cambridge University Press, Cambridge, 1995).
5. R. S. Smith, C. Huang, E. K. L. Wong, and B. D. Kay, *Surf. Sci. Lett.* **367,** L13–18 (1996).
6. R. S. Smith, C. Huang, and B. D. Kay, *J. Phys. Chem.* **101,** 6123 (1997).

Ozone Decomposition in Soot Aerosols

R. S. Disselkamp, M. A. Carpenter,*
and J. P. Cowin

Supported by Laboratory Directed Research and Development (LDRD) Funding.

*Postdoctoral Research Associate.

Carbonaceous material in the earth's atmosphere arises from both natural emissions such as global biomass burning, and anthropogenic sources such as fossil fuel combustion. The average annual global source of particulate carbon has been recently estimated[1] to be as high as 24 Tg/yr, and represents a significant fraction of the atmosphere's particulate loading. Soot, also referred to elemental carbon, has been observed to comprise 15–20% of the total carbon present in rural areas and 20–60% at urban locations.[2] An understanding of soot chemistry is important, since it may effect tropospheric ozone concentration and influence the partitioning of nitrogen oxides. In our investigations we have focused on the ability of soot to deplete ozone.

Static aerosol samples are created within an atmospheric simulation chamber having a diameter of 20 cm and a length of 1 m.[3] The chamber has been Teflon coated to enable oxidant species to be studied. A White multiple-reflection absorption cell within the chamber has been interfaced to an FTIR spectrometer, providing an absorption path length of ~10 m and a trace gas sensitivity of ~10 ppm. Experiments were performed using a four-step procedure. First, the chamber was evacuated and a background spectrum collected. Next, ozone was introduced into the chamber. Spectra were then collected at regular time intervals, and finally a soot aerosol was generated by rapidly expanding a powder through two stainless-steel wire mesh screens (100 and 320 mesh) and into the chamber. The screens aided de-agglomeration of the soot particulate material, creating a finely-dispersed aerosol sample. After each experiment it was necessary to clean the chamber, accomplished by removing the White cell from the chamber, introducing a cleaning solution into a rod inserted in the chamber, and using deionized water at high pressure to remove particulate debris from the chamber walls. A pump located at the base of the chamber was used to remove spent cleaning solution. Mechanical pumping was employed to dry the chamber, and the White-cell was then realigned within the chamber.

Figure 2.8 shows infrared spectra collected (a) before and (b) after the addition of soot to the chamber. Absorption features arising from the ν_3 2350-cm^{-1} band of CO_2, the ν_2 1850 cm^{-1} bending mode of water, and the ν_3 1050 cm^{-1} asymmetric stretching mode of ozone are seen. The increasing extinction with increasing wavenumber in (b) arises from the absorption and scattering of light by the soot aerosol. An analysis of many spectra collected before and after the addition of soot to the chamber yields time-dependent O_3 and CO_2 partial pressures, and is shown in Fig. 2.9. The small decrease in O_3 partial pressure prior to soot addition demonstrates that the chamber is chemically inert with respect to O_3 decomposition. After the addition of soot, however, O_3 partial pressure is dramatically reduced, whereas CO_2 pressure shows a corresponding increase. The quantity of CO_2 generated relative to the O_3 consumed is 2:1, so a reaction consistent with this observation is

$$2\,O_3 + O_2 + 4\,C(\text{soot}) \rightarrow 4\,CO_2.$$

The role played by molecular oxygen in this reaction is unknown, but it has been suggested that it may be a reaction intermediate obtained by stabilizing radical sites present at the surface of soot.[4] By varying soot concentration within the chamber, a reaction order with respect to soot of 1.5 was obtained.

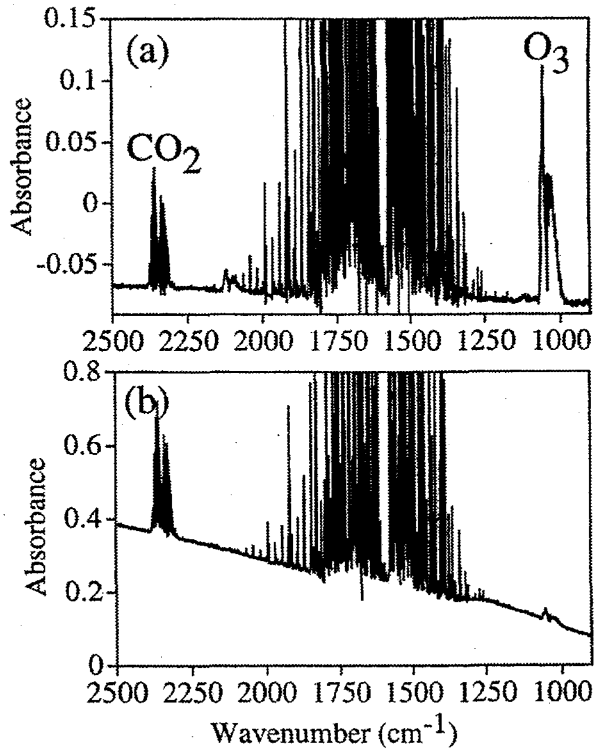

Figure 2.8. Infrared spectra (a) before and (b) after the addition of 24 mg of Degussa FW black carbon soot to the chamber. Note disappearance of O_3 and increase of CO_2 absorption.

The likelihood of atmospheric ozone depletion to occur on soot can be assessed if it is assumed that Degussa FW2 soot material is a good surrogate for atmospheric soot. The soot concentration used in our experiments was ~1 × 10^{-6} gm/cm^3, compared to a typical atmospheric background concentration of 1 × 10^{-12} gm/cm^3. Hence the rate of ozone decomposition in the atmosphere will be 10^9 times slower than our measured rate, or ~4 × 10^7 days. Since the tropospheric ozone lifetime is only ~30 days, no significant ozone destruction due to ozone–soot chemistry is expected.

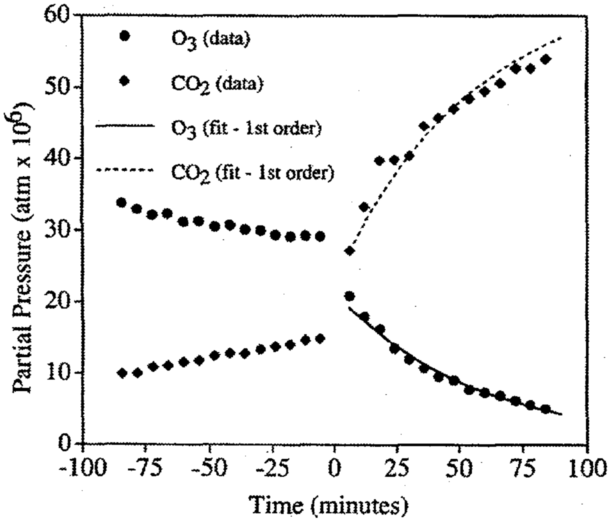

Figure 2.9. O_3 and CO_2 partial pressures, before and after soot addition. Time = 0 corresponds to the moment when 24 mg of Degussa FW2 soot was introduced into the chamber. The solid line corresponds to treating the decay of O_3 as a pseudo–first-order process with $\tau = 56.8$ min. The dashed line is the modeled CO_2 production using the same time constant and the reaction

$$2O_3 + O_2 + 4C(\text{soot}) \rightarrow 4CO_2.$$

References

1. J. E. Penner, H. Eddleman, and T. Novakov, *Atmos. Environ.* **27A**, 1277–1295 (1993).
2. H. Seinfeld and S. N. Pandis, *Atmospheric Chemistry and Physics* (John Wiley & Sons, New York, 1998).
3. M. L. Narus, N. C. Schoenfelder, Y. Na, L. A. Chavasse, and R. S. Disselkamp, *Rev. Sci. Instrum.* **67**, 4364–4368 (1996).
4. D. M. Smith, and A. R. Chughtai, *J. Geophys. Res.* **101**, 19607–19620 (1996).

The Structure of Iron Oxides Surfaces

*S. A. Joyce and S. A. Chambers**
Supported by DOE Environmental Management Science Program (EMSP).
*EMSL Interfacial and Processing Science.

Heterogeneous reactions on metal oxide surfaces are central to a better understanding of numerous environmental problems, ranging from the transport of pollutants through soils to the catalytic destruction of toxic chemicals. The scanning tunneling microscope (STM) is capable of imaging solid surfaces and molecular adsorbates with atomic-scale resolution. As a real space probe, the STM can directly determine the role of surface structure, especially at defects such as steps, vacancies, etc., in the adsorption and heterogeneous chemistry of molecules on surfaces. Many surfaces of relevance to environmental chemistry are, however, unsuitable for detailed studies due to the insulating nature of many materials, the lack of large, single-phase crystals, and/or difficulties associated with surface preparation. Our approach has been to use bulk single crystals, either natural or man-made, when available, and to use thin film epitaxy for those systems where bulk materials are not suitable.

We have continued our examination of epitaxially grown magnetite (Fe_3O_4) films. The presence of reduced iron in Fe_3O_4 allows this material to convert toxic pollutants such as hexavalent chromium and halogenated hydrocarbons into less harmful species. $Fe_3O_4(001)$ grown on MgO(001) substrates were studied. MgO, an insulator, was chosen as the substrate due to a near perfect lattice matching (better than 0.3%) with Fe_3O_4. Magnetite adopts a spinel crystal structure. One third of the iron is in the 2+ oxidation state, with the tetrahedral sites occupied exclusively by Fe^{3+} and the octahedral site occupied by both Fe^{3+} and Fe^{2+}. Along the (001) direction, the structure can be viewed as alternating sheets of tetrahedral sites and octahedral sites. The separation between these sheets is ~1 Å, so that the separation between like sheets (i.e., tetrahedral to tetrahedral) is 2 Å. An important question is whether the surface is terminated by one type of sheet or by a mixture of both. Based on numerous STM experiments, only step heights of 2 Å or integral multiples thereof have been observed. This is consistent with a model where the (001) surface is terminated exclusively by either a tetrahedral or an octahedral sheet, but not by both.

The nature and detailed atomic scale structure of the surface can be determined from high resolution STM studies. A c(2×2) reconstruction of Fe_3O_4 (001) is observed with both STM and diffraction measurements. This reconstruction can be rationalized using simple energetic considerations. The ideal surfaces for either termination are high-energy structures, due to an imbalance in the number of occupied and unoccupied dangling bonds on the surface. The surface atoms can rearrange to minimize or eliminate this imbalance. At least two inequivalent structures give rise to a balance (i.e., autocompensation) of the dangling bonds, either by removing every other iron from the tetrahedral sheet or by removing oxygens and oxidizing some of the Fe^{2+} sites in the octahedral sheets.

A high-resolution image of the reconstructed surface is shown in Fig. 2.10. The most notable feature of this image are the bright protrusions which cover the surface in a c(2×2) pattern. From many previous experimental and theoretical studies of tunneling on metal oxide surfaces, it has been shown that the metal cation sites appear as protrusions, whereas the oxygen anion sites appear as depressions. Given this and the observation that there is only one protrusion per unit cell, we interpret the STM image as arising from the reconstructed tetragonal termination.

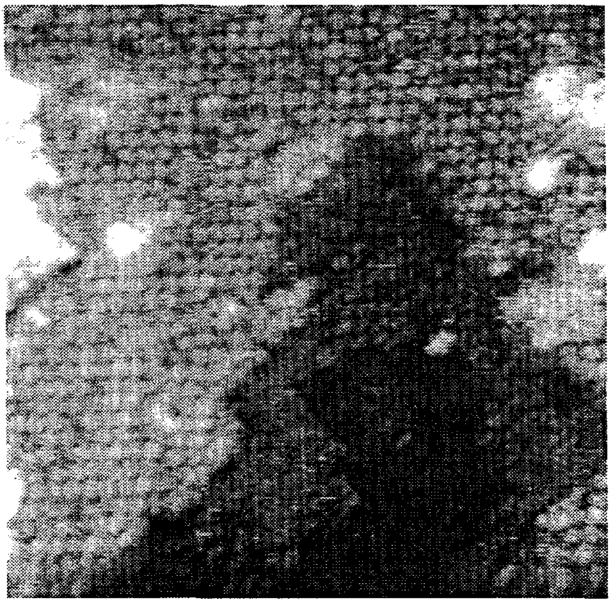

Figure 2.10. STM image of a Fe_3O_4(001) surface with a c(2×2) reconstruction. Scan range 30 nm × 30 nm; tunneling conditions, −1.5V/nA.

As mentioned, a number of environmentally relevant processes result from the energetic accessibility of the Fe(II)/Fe(III) redox couple in the natural environment. An additional consequence is the facile interconversion between different forms of iron oxide. Under even mildly oxidizing conditions, α-Fe_2O_3, hematite, is the thermodynamically favored form. In hematite, all the iron is in a 3+ oxidation state, and the crystal structure is corundum, where the iron occupies octahedral sites. Under reducing conditions, Fe_3O_4 is favored. A third phase is γ-Fe_2O_3, maghemite, which adopts a spinel structure nearly identical to Fe_3O_4, with iron vacancies in the octahedral sites. Previous work by us and others has shown that the hematite (001) surface can be converted to the magnetite (111) surface by sputtering and annealing. Sputtering of metal oxides is generally reducing due to the preferential removal of oxygen. We have annealed the magnetite (001) surface in oxygen and found that after prolonged oxidation, the c(2×2) surface converts to a (3×1) symmetry.

An STM image of Fe_3O_4 (001)(3×1) is shown in Fig. 2.11. Dark rows can be seen running along the diagonals; these rows are separated by three unit cells, hence the 3×1 designation. Note that the rows run in orthogonal directions on terraces separated by a single height step. As with the

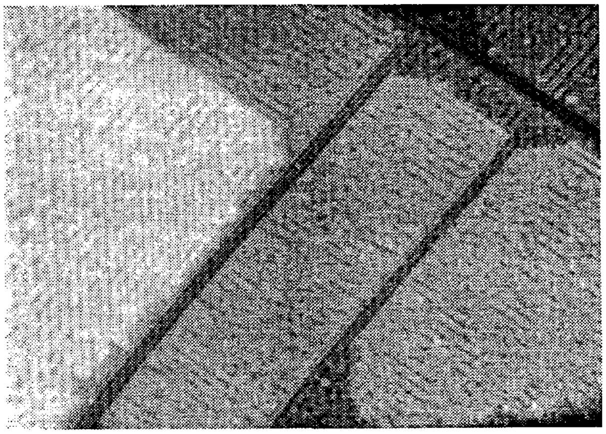

Figure 2.11. STM image of a Fe_3O_4(001) surface with a (3×1) reconstruction. Tunneling conditions, −1.5V/nA.

c(2×2) surface, all step heights are 2 Å. As the cations appear as bright protrusions, we interpret the dark rows as cation vacancy sites. This reconstruction is consistent with a highly ordered maghemite (001) surface, as the difference between Fe_3O_4 and Fe_2O_3 is one iron vacancy in every three unit cells. For this ordered maghemite, only the octahedral sheet is autocompensated.

Reference

1. S.A. Chambers and S.A. Joyce, "Surface Termination, Composition and Reconstruction of Fe_3O_4 (001) and γ-Fe_2O_3 (001)," *Surf. Sci.*, in press.

Photoionization of Liquid Water Using a Newly-Constructed Liquid Beam Source

R. G. Tonkyn, N. Petrik,*

S. E. Barlow, and T. M. Orlando

Supported by DOE Office of Basic Energy Sciences.

*Visiting Scientist.

A liquid-beam/droplet source (LDS), designed to produce micron-sized beams of homogeneous liquids and heterogeneous solutions in a high vacuum, has been constructed. The jet is formed by forcing liquid through a 10–100 µm diameter pinhole into a large evacuated chamber. The beam is pointed directly at a large cryopump a few centimeters away that condenses most of the liquid. The small size of the beam combined with the low background pressure (~10^{-5} Torr for water) is designed to permit free (or nearly free) evaporation of the liquid. This allows in principle the direct study of the liquid interface without the usual interferences due to collisions with the vapor. Furthermore, the surface is continually replenished. Rapid evaporation of the liquid produces a significant temperature gradient via evaporative cooling, which can be exploited to vary the temperature under study by translating along the beam. At right angles to the beam a skimmer samples the vapor through several stages of differential pumping into a quadrupole mass spectrometer. A differentially-pumped time-of-flight photoelectron/photoion spectrometer protrudes into the beam chamber for direct photodesorption or photoemission studies of the jet. The instrument design is shown in Fig. 2.12; Fig. 2.13 is an image of a liquid water beam 2–3 mm downstream from a 10-µm nozzle.

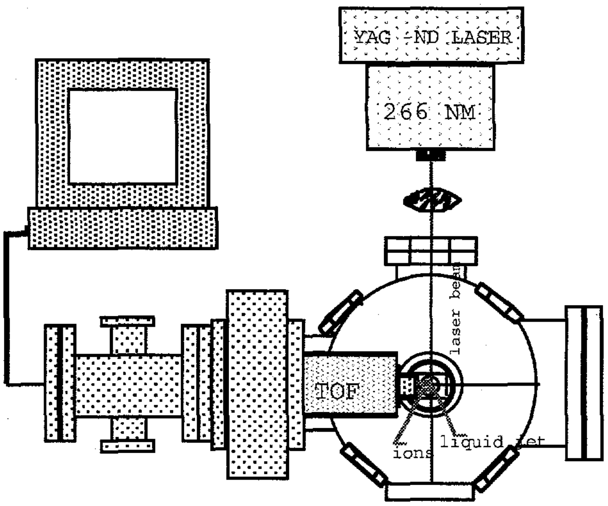

Figure 2.12. Liquid beam source chamber.

In proof-of-principle experiments, the liquid jet was irradiated with the focused 266-nm output (0.07–3.8 mJ/pulse) of a Nd:YAG laser (5-ns, 20-Hz pulses), and the positive ions produced during irradiation were collected, separated, and detected by the differentially pumped time-of-flight (TOF) mass-spectrometer. The TOF spectra (Fig. 2.14) contains several peaks which we tentatively assign as H^+, H_2^+, O^+, OH^+, and H_2O^+. Our assignment suggests that we see signal both from directly ion-

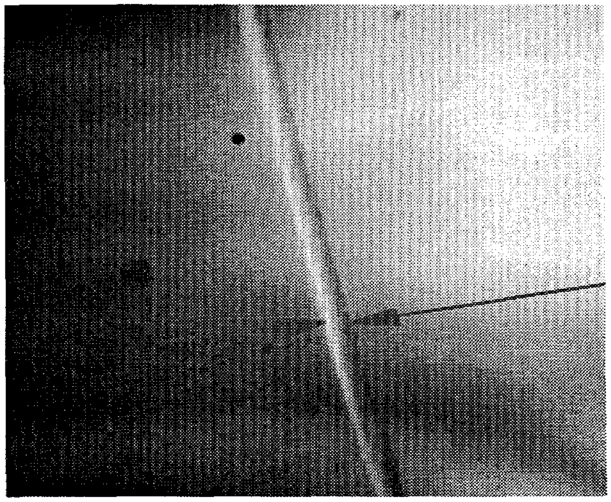

Figure 2.13. Liquid beam at 2–3 mm from the nozzle. The measured diameter of the beam is 7 µm. The nozzle has a 10-µm aperture.

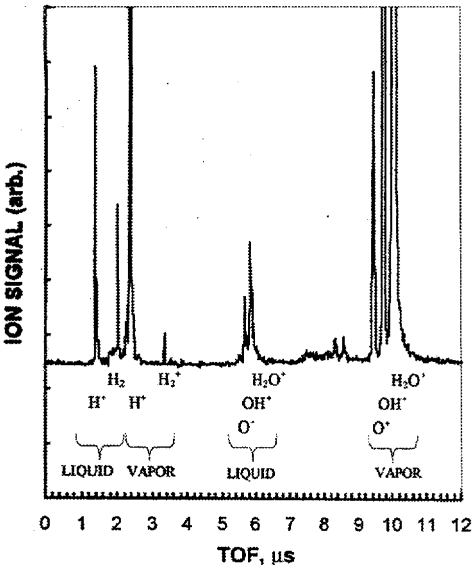

Figure 2.14. Time of flight MPI spectrum of a liquid water jet. The fourth harmonic of a Nd:YAG laser at 255 nm was the ionization source.

ized liquid as well as photoionization of water ejected into the gas phase by ablation. Experiments utilizing higher-energy photons at much lower energy density should be more easily interpreted. Future work will utilize 193-nm and 157-nm light from an excimer laser, as well as a newly constructed laser-based vacuum ultraviolet source near 100 nm. These experiments will allow us to probe the valence band structure as well as the dissociation and photoionization dynamics of liquid water.

A Soft-Landing Ion Beam for Re-Creating Ionic Interfaces

J. P. Cowin and M. J. Iedema

Supported by DOE Office of Basic Energy Sciences.

Ionic processes take many forms, and ion beam methods have long been used to conduct and understand these processes. Yet a class of very common ionic systems, solutions containing ions, has seldom found direct use for ion beams. Ion beam sources should in principle be excellent for re-creating condensed systems, which then could be used for study by a wide variety of bulk and surface analytical methods. But this requires ion beams that are well mass-selected and very clean (low neutral flux), intense (1–100 nA), include important solution-phase ions (H_3O^+, NH_4^+, OH^-, NO_3^-, alkali ions, etc.), and have very low energy (0.5–5 eV) to prevent impact-induced chemistry. These are extreme restrictions. To meet these needs we built a unique ion source in collaboration with Professor Barney Ellison at the University of Colorado, Boulder.

Figure 2.15 shows the ion source, which is extensively differentially pumped. Figure 2.16 shows the current at the target as the mass selector is scanned, for increasing pressures of pure D_2O vapor in the nozzle. These resemble typical "cracking patterns" expected for electron impact ionization at low pressure. At higher D_2O nozzle pressures, ion–neutral collisions in the jet convert D_2O^+ to D_3O^+; similarly, we can make ammonium ions (NH_4^+). We have made 10–70 nA beams this way. Secondary electrons from the electron impact also can interact with the electronegative molecules in the neutral jet to create negative ions, such as OH^-, Cl^-, and NO_3^-.

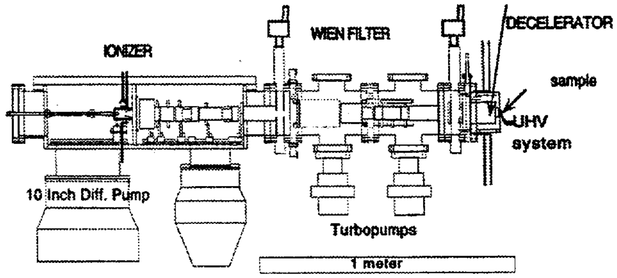

Figure 2.15. Schematic of ion source.

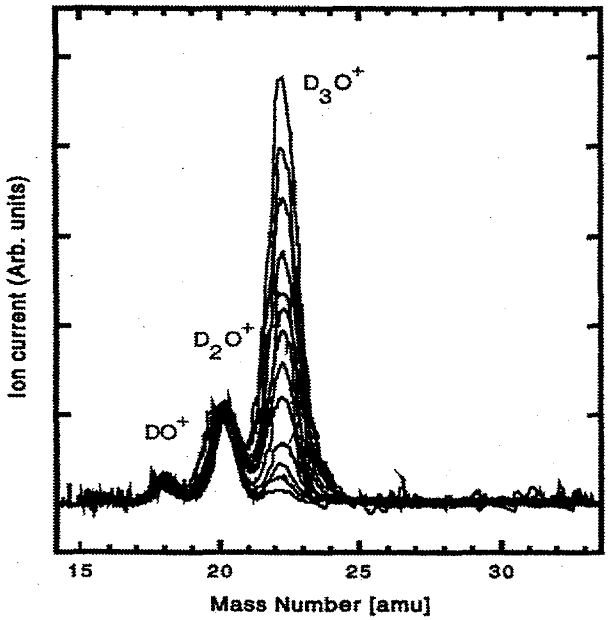

Figure 2.16. Current at target as a function of mass number, for increasing nozzle pressures of D_2O vapor.

The ion beam operates at 300–400 eV, and must be decelerated to 1 eV before hitting the target. A simple approach was chosen: a parallel field geometry from a 300 line-per-inch double mesh to the target, placed nearly touching a plate with a hole, which decelerates the beam without space-charge problems. The measured current stays constant up to the last volt, then drops off over a 0.8-eV fwhm—the "ion beam stopping curve." By biasing the target at the beam voltage minus 1 eV, ions deposit on the target at 1 eV. As any surface film charges, the target bias is changed to correct for effects of work-function change.

A convenient condensed phase is another need, where we can employ vacuum-based surface analytical methods and the vacuum-based ion beam. If the temperature is reduced sufficiently, solvent vapor pressures drop to manageable levels. This approach is not limited to crystalline ice solvents: many solvents, including water, can be grown epitaxially in glassy states. Above a characteristic glass temperature, these amorphous solvents are true liquids. Below the glass temperature (about 135 K for water), many processes, like charge transfer, are expected to proceed much as they would in a high-temperature liquid, but with the advantage that the ion/substrate can be put into well-determined initial states, with control over both distances (normal to the surface) and solvent composition, including abrupt phase boundaries.

Applications of the soft-landing ion beam typically follow the approach seen in Fig. 2.17, showing the simple case of a nearly ideal glass. We deposit ions on top of a 37-monolayer film at 30 K and monitor their position using a non-contact work-function probe. We observe their motion near 90 K as we ramp the temperature upward, at a temperature close to that expected from the known temperature-dependent viscosity. The results are in good agreement with the ion mobility predicted by the Stokes-Einstein law and the known viscosity of 3-methylpentane.

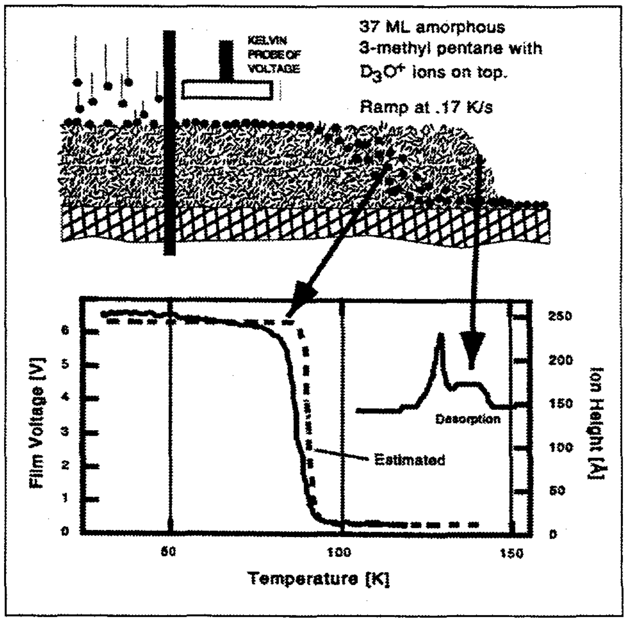

Figure 2.17. Film voltage as a function of temperature for a 37-ML film of amorphous 3-methylpentane with D_3O^+ ions deposited on top.

Soft-Landed Ion Study of Water

J. P. Cowin, M. J. Iedema,
A. A. Tsekouras, et al.*

Supported by DOE Office of Basic Energy Sciences.

*Visiting Scientist, University of Athens.

Water is one of our most fundamentally important materials. We created our ion source with the study of ionic processes in water as a major goal. One obvious target was proton transport in water ices. In the process of our studies, we also set out to confirm some fundamental properties of water ices (crystalline or amorphous) that standard monographs on water suggest are well understood. We found our studies provided some significant surprises, forcing a re-assessment of basic water properties.

1. Immobility of Protons in Water Ice from 30 to 190 K.[1]

With the collaboration of K. Wu* and G. B. Ellison.†
*Postdoctoral Research Fellow.
†University of Colorado.

The anomalously fast motion of hydronium (H_3O^+, D_3O^+) in water is often attributed to the Grotthus mechanism, in which the hydronium proton tunnels from one water molecule to the next. This tunneling is particularly relevant to proton transport under restricted geometries, e.g., biological "proton wires" and stratospheric ice chemistry. Hydronium transport in ice is thought to be closely related to its transport in liquid water. Controversies persist: some claim ice's ordered, equivalent sites permit tunneling even at 0 K; others see non-zero activation energies for hydronium motion in ice. It had not been previously possible to dope ice with pure hydronium ions, or track their motion directly. Here we succeed using a soft-landing hydronium ion source, showing that hydroniums do not move at temperatures up to 190 K in crystalline ice.

Water's hydrogen-bonded network must disrupt to solvate or transport ions. Figure 2.18 shows H-bonding in a thin film. Normally each water hydrogen-bonds with four neighbors. Three hydroniums were initially placed on top of the film. At right, a proton has hopped via the Grotthus mechanism four monolayers down.

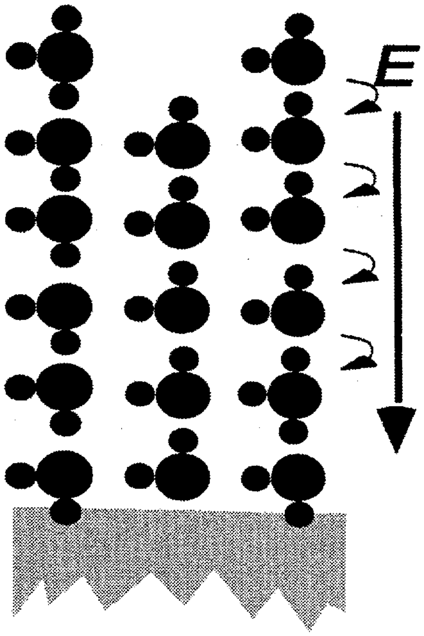

Figure 2.18. Sketch of hydrogen bonding in a thin film.

We prepared targets by depositing D_2O or H_2O films 0.2–1.5 μm thick on a Pt(111) single crystal, yielding single-crystal ice above 140 K. Figure 2.19 shows ΔV for D_3O^+ ions deposited on D_2O ice at 33 K, then ramped up in temperature. The initial film voltage, 11.7 V for the 20 nC deposited, is consistent with $\varepsilon = 2.3$ and the ions initially staying on top of the film. The voltage stays nearly

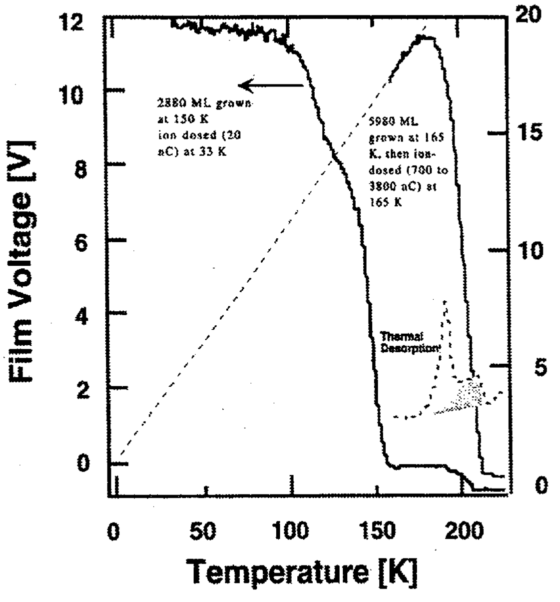

Figure 2.19. Film voltage as a function of temperature for D_3O^+ ions deposited on D_2O ice.

constant up to 100 K, then drops in steps at 110, 150, and 200 K. Near 150 K, ε should become "active," increasing to over 100, accounting for this large voltage drop. Substantial water desorption begins around 180 K. The 200-K drop is caused by desorption of the last of the water, and a work function change of +0.6 V. The lack of large voltage changes below 150 K shows that hydronium does not move from 33 to 120 K, and probably to 150 K, even in a 1.1×10^7 V/m field.

To probe hydronium motion above 150 K, we deposited substantially more ions at temperatures between 140 and 165 K, where the dielectric constant is large. Data for ice grown at 165 K is shown in Fig. 2.19. If the ions don't move, the voltage should vary as $1/\varepsilon(T)$. For $T \geq 160$, ε varies as $1/T$, predicting a voltage proportional to T. Figure 2.19 shows that the work function does increase linearly with T, until water desorption near 200 K. Thus hydronium does not move in ice from 33 to 190 K. We sandwiched ions inside of crystalline ice films, and saw no evidence of any surface trap. No mobility is the case for both D_3O^+ in D_2O and H_3O^+ in H_2O.

The absence of the Grotthus mechanism is easy to accept: tunneling long distances should only work if the potential is periodic. But normal ice is proton-disordered, destroying the periodicity. Further, the hydronium ions should self-trap in a polarization well.

2. Ferroelectricity in Proton-Ordered Water Ice.[2]

With the collaboration of K. Wu,* M. Dresser,†
D. Doering,§ W. P. Hess, and B. Rowland.*
*Postdoctoral Research Fellow.
†Washington State University.
§Associated Western Universities.

Water ice in its familiar form (ice I, either hexagonal or cubic) is well ordered with respect to the oxygen positions and in that all hydrogens are hydrogen-bonded to the oxygens of neighboring molecules. But this still allows an infinity of water dipole orientation patterns. Thus ice is proton-disordered, even at 0 K, due to the sluggish ability of the molecules to re-orient. To date no one has truly (in our opinion) made fully proton-ordered ice I. In this study we make slightly proton-ordered ice and critique two other studies that claim to have made proton-ordered ice I.

Fully proton-aligned water ice I, with all the water dipoles exactly aligned (ice I-cubic) or nearly so (ice I-hexagonal) has long been sought experimentally. Several groups (Somorjai and Shen at University of California, Berkeley, via sum-frequency measurements; and Whitworth at University of Birmingham via electrical studies and neutron diffraction) have reported or implied fully aligned ice I forms. We independently found a tendency for vapor-deposited ice films (either amorphous or crystalline) to become proton aligned. This was evident by an apparent charging of the ice films even without deposited ions, with negative outward. We find the alignment to be very slight: as shown in Fig. 2.20, at 0 K we have about 2% of the protons aligned, and this drops as 0.016 × $\exp(-T/27)$. This effect had been observed in the 1970s by Kutzner, and by Onsager and coworkers. The asymmetry of the growing solid–vacuum interface allows a net dipole per monolayer to occur. The large drop in alignment near 128 K is due to the turn-on of amorphous water's dielectric screening; the rise peaking at 140 K is due to the ice growing crystalline above 135 K. The effect then decreases above 140 K as the dielectric constant of crystalline ice begins to have an effect. We quantitatively assessed the data from the other groups, and conclude that Somorjai and Shen's ice is only very slightly aligned, and possibly by the same mechanism as ours. Whitworth's ice we conclude could not be ferroelectrically aligned,

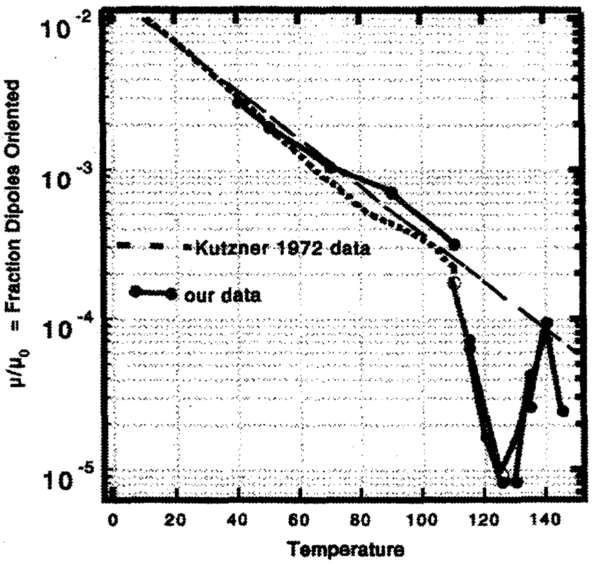

Figure 2.20. Fraction of dipoles oriented in water ice as a function of temperature.

though possibly antiferroelectric.

3. *Highly Proton-Ordered Water Ice.*
With the collaboration of K. Wu,
Postdoctoral Research Fellow.

We measured two extraordinary properties of ice films, which may be explained by the formation of highly proton-aligned ice. We grew ice films at 160 K, where they should be fully crystalline and aligned with the Pt(111) substrate. Upon these we deposited Cs^+ or D_3O^+ ions. From the voltage rise vs. charge, it is clear that the dielectric constant was fully active at 160 K, and as expected had a value between 100 and 200. As shown in Fig. 2.21, the film voltage created by the ions increases with temperature linearly with T above 160 K (until the water desorbs). This is expected, as the dielectric constant should vary as $1/T$. Two unusual things are observed as we drop the temperature (before any heating above 160 K): (1) the voltage decreases as T drops to 30 K, and we see it reversibly go back up, with no observable time constant (less than a few seconds at most) over the entire temperature range. No pure ice sample has previously shown such an active dielectric constant below 150 K, and even hydroxide-doped ice becomes inactive below 70 K. (2) The voltage can be precisely fit as T^2. This implies that the dielectric constant goes as $1/T^2$.

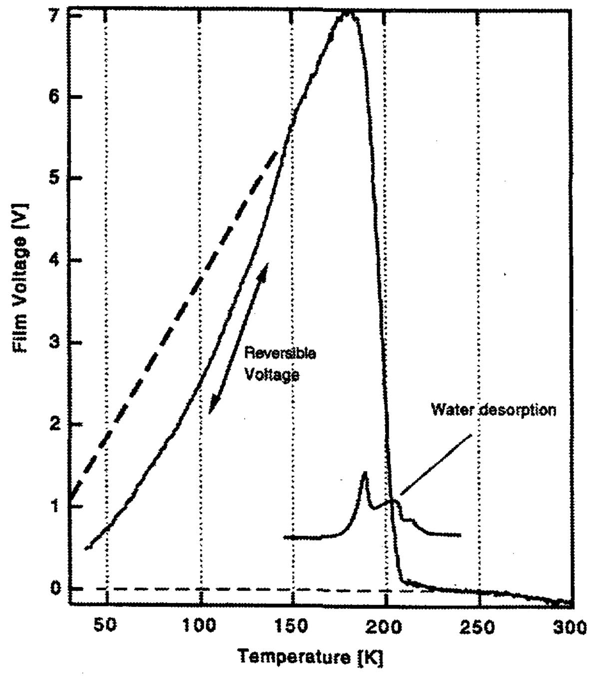

Figure 2.21. Film voltage as a function of temperature for Pt(111) dosed with D_2O and Cs^+ at 160 K.

What leads us to believe that the ice is proton-aligned is the numerics: at the bias voltage created by the ions, for the dielectric constant of ice at 160 K, each monolayer of water must be about 1/4 aligned, just to create the field to shield the field induced by the bare ions. This fact, combined with the remarkable electrical properties above, prompt our conclusion, which awaits additional confirmation. The activity to 30 K also suggests that hydrogen-bond defects (L or D) must be mobile in this ice to as low as 30K.

4. *Field-Dependent Motion of D-Defects in Water Ice.*[1]

Figure 2.22 shows D and L defects, which are misdirected hydrogen bonds that put either two or zero protons between two adjacent oxygens instead of the usual one. These D/L defects facilitate the re-orientation of water molecules, creating water's high solvation power and dielectric constant. D/L defects moving under the influence of an external field flip water orientations. They have an effective charge of ±0.38 $|q_e|$, regarding the external field changes generated by their motion-induced water dipole re-orientations. Also shown is a D-defect created by a deposited hydronium.

We have studied crystalline ice films grown at 140 K, dosed with D_3O^+ ions at 30 K, then T-ramped. The initial film voltages were from 10 to 30 volts, and initial coverages were from 600 to 5060 mono-

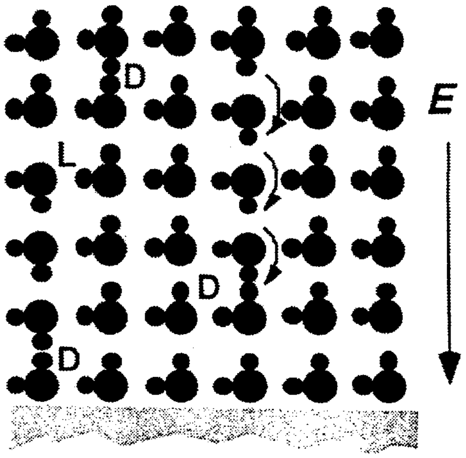

Figure 2.22. D and L defects in water ice.

layers thick. No ion diffusion was found. The voltage fall-offs had different shapes, but formed a continuous family vs. electric field strength when plotted in a normalized fashion. The fall-off near 150 K is the expected onset of ice's dielectric constant due to formation of L/D defect pairs. The drop near 120 K we identify as due to 1–1.5 D-defects per hydronium deposited becoming mobile and moving through the ice. Given their effective "charge" of 0.38 $|q_e|$, the 1/3 to 1/2 voltage drop is immediately understood.

The temperature of the "120-K" drop is very field-dependent. The half-point temperatures of that drop extrapolated to zero field is 124 K, and the field for 0 K mobility is 1.6×10^8 V/m. The field dependence implies that an ion in solution can induce proton flipping far away from itself, without thermal activation of the water.

5. Amorphous Water:
Two Unexpected Properties

We have observed irreversible dielectric responses in amorphous ices.[3] Figure 2.23 shows 30-K deposited amorphous D_2O ice films with Cs^+ and D_3O^+ ions on top. As the temperature is ramped, the film voltages irreversibly disappear near 50 K, much lower than the expected 135 K! This is a purely dielectric effect, as hexane/water sandwich studies show. Figure 2.23 shows that this fall-off can be progressively pushed up to near 120 K by pre-annealing the ice to similar temperatures. This behavior is understood in terms of fluffy, stressed amorphous ice irreversibly compacting and annealing, which allows water molecule orientations to flip in response to any co-existing fields; a useful effect for future work on ionic/electron experiments.

We have also discovered that there is no ion motion in amorphous ice above the glass temperature. The mobility of an ion under a field is approximately inversely proportional to the viscosity of the medium, so we can use ion motion to measure whether amorphous water above its glass temperature is a true liquid. Figure 2.24 shows that in deuterated amorphous ice both D_3O^+ and Cs^+ are immobile from 30 to 40 K; above that, the transient turn-on of the dielectric constant obscures any ion motion. But Fig. 2.25 shows ice films where higher initial voltages were placed

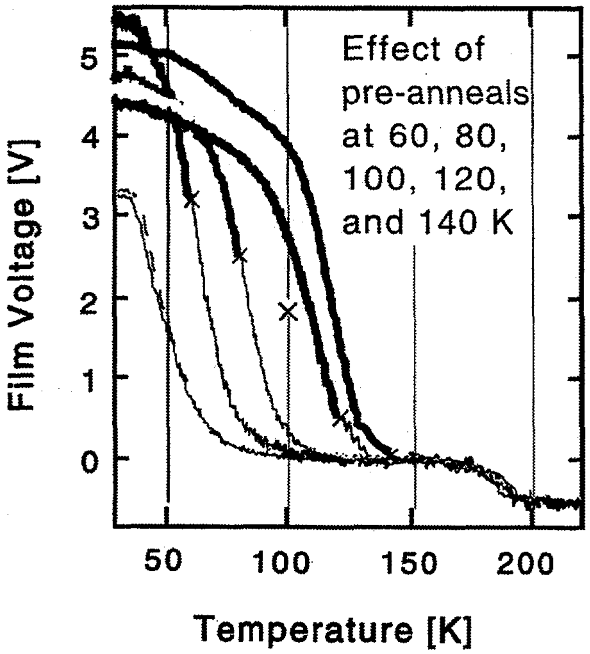

Figure 2.23. Dielectric response of amorphous ice: effect of pre-annealing.

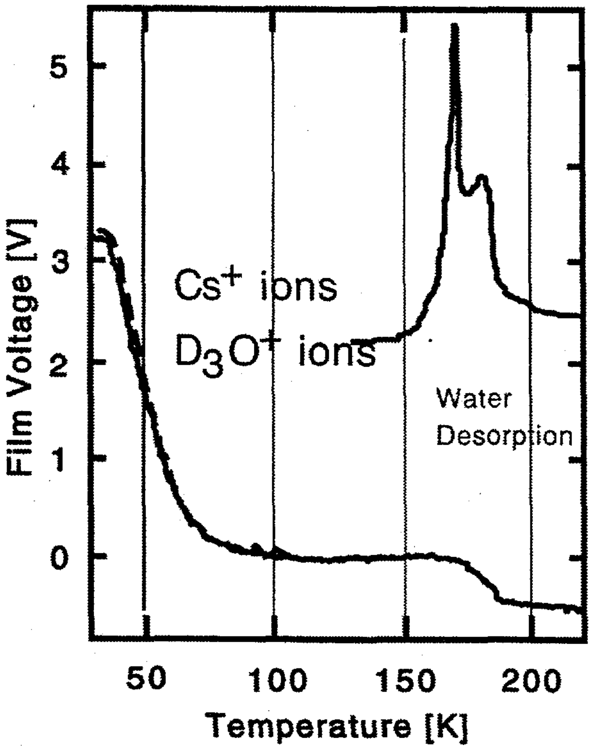

Figure 2.24. Dielectric response in deuterated amorphous ice.

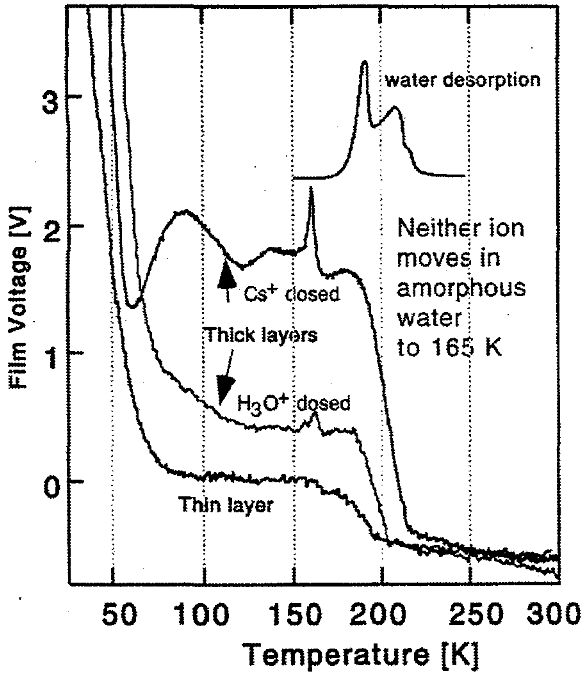

Figure 2.25. Showing immobility of ions in amorphous ice above T_{glass}.

(30–70 V, on, ~2000-ML films). This makes easily measurable the voltage that persists after the dielectric constant turns on, provided the ions stay on top of the ice film. The lowest curve shows a 60-ML film biased initially to a few volts, the "zero" for these comparisons. For glass temperatures 135–165 K, we would have expected the ions to move, if it were a true liquid. Curious fluctuations associated with dielectric phenomena are seen. But the ions stay on top, as the voltages do not drop to the zero (thin film) curve. Near 165 K, where the amorphous ice crystallizes, a spike in the film voltage appears. Ions under their self-generated field gradient should be hundreds of times more mobile than neutrals in a liquid. Either the amorphous ice is not a true liquid above 135 K (as some feel), or the ions nucleate the crystallization around the ion at a lower temperature.

References

1. J. P. Cowin, A. A. Tsekouras, M. J. Iedema, K. Wu, and G. B. Ellison, *Nature*, in press (1999).
2. This work was featured in a recent Nature "News and Views" (S.T. Bramwell, "Ferroelectric Ice," *Nature* **397**, 212–213 (1999)); it appears in full in M. J. Iedema et al., *J. Phys. Chem.* **102**, 9203– 9214 (1998).
3. A. A. Tsekouras, J. P. Cowin, and M. J. Iedema, *Phys. Rev. Lett.* **80**, 5798-5801 (1998).

Phase Transfer of Hydrated Ions

K. Wu, J. P. Cowin,*
M. J. Iedema, and A. A. Tsekouras[†]

Supported by DOE Office of Basic Energy Sciences.

*Postdoctoral Research Associate.
[†]Visiting Scientist, University of Athens.

Separation processes for ionic species, like Cs^+, from complex mixtures (such as Hanford tank waste), or in biological transfer of ions across membranes, involve moving an ion from a well-solvated aqueous region into an organic medium with poorer solvation. This has been the focus of several theoretical studies at PNNL and elsewhere. We have begun studies of this using the soft-landed ion source. Since our previous work for ions in water ices has shown near-zero motion in either crystalline or amorphous water up to 200 K, we do not look for transport of ions across a thick water film into an organic medium. Instead, we introduce ions on top of an organic layer, and then look at the ability of small amounts of added water to inhibit the motion of the ion. The water is expected to alter the motion in two ways. At sub-monolayer amounts of water, illustrated in Fig. 2.26, we anticipate that the water molecules will form a water–ion complex. This will increase the size of the ion, and will thus slow it down by increasing its viscous drag. We should then expect to measure, via the amount it has slowed, the hydration state of the ion. The hydration number of the ion ought to vary with the amount of water deposited and the thermal history. A second effect occurs for thicker water films: here the ion becomes hydrated fully in the water film.

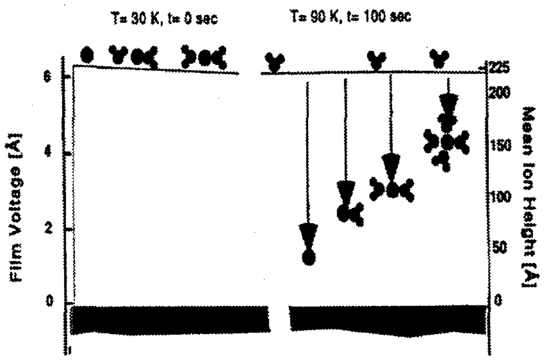

Figure 2.26. Ion motion into organic film, vs. hydration state.

We expect the energy of the ion to be lowest if it remains in the aqueous layer, and we should see no ion motion.

Figure 2.27 shows data for 60-ML films of methyl cyclohexane (MCH), which has a glass temperature of 85 K. Upon it is placed water in increasing amounts, then hydronium ions. Contrary to what we might expect based on the lack of hydronium mobility in thick water films, it made no difference up to at least 10 ML of water whether the ions were added on top of or under the water film. As the samples were ramped in temperature, we see strong effects due to the water. First, the low-temperature ion motion seen at these high fields disappears by the time 1 ML of water has been added. Also, the rapid fall-off at near 100 K is shifted upward in temperature. Finally, the curves develop a tail extending to 120 K. The plot of temperature of the maximum slope vs. water shows a plateau between about 0.5 and 1 ML of added water, of 3 K. Then for more water added, a very large shift occurs. The large shift for more than 1 ML of water is much too great to be accounted for by a simple increase in ion size. The plateau may be due to such a shift.

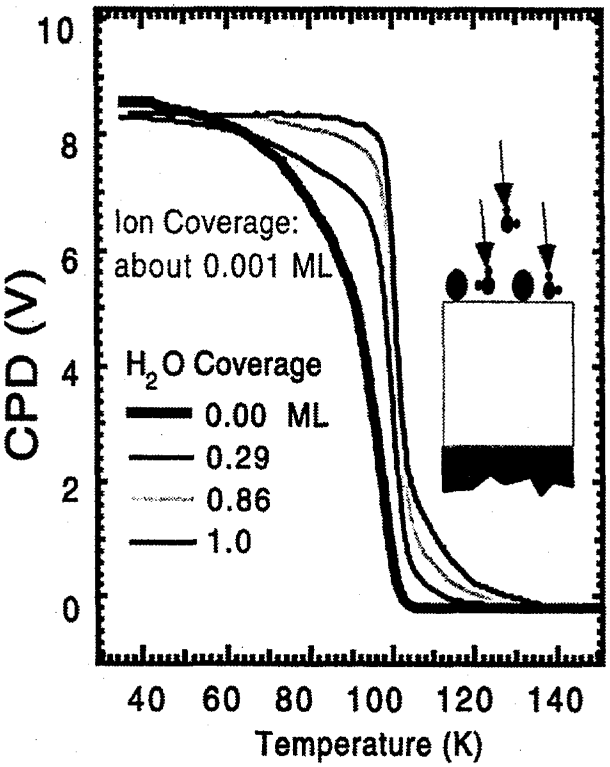

Figure 2.27. Results for 60-ML films of MCH.

3. High-Energy Processes at Environmental Interfaces

Characterization of Nanocomposite Materials Prepared via Laser Ablation of Pt/TiO_2 Bi-Combinant Targets

*K. M. Beck, T. Sasaki,**
*and N. Koshizaki**

Supported by DOE Office of Basic Energy Sciences, National Science Foundation, and Agency of Industrial Science and Technology (Japan).

*National Institute of Materials and Chemical Research, Agency of Industrial Science and Technology, Tsukuba, Japan.

TiO_2 in its anatase form is far less well understood than the rutile modification. However, recent applications of colloidal anatase in novel photochemical solar cells, the high mobility that anatase affords *n*-type charge carriers, and the metal–nonmetal transition in the impurity band of reduced anatase thin films have increased interest and investigations.[1,2] Several researchers attribute primary photoactivities in TiO_2 and TiO_2 composites to the anatase crystal phase.

One such composite, Pt/TiO_2, is used as a photocatalyst and photoelectrode for the decomposition of water.[3,4] Recently, researchers have explored the synthesis of Pt/TiO_2 nanocomposite thin films using rf magnetron co-sputtering of Pt and TiO_2.[5] The unique optical and chemical properties of these nanocomposites arise from quantum size effects of the embedded nanoparticles in the matrix, or from surface effects between the nanoparticles and the matrix. At low concentrations of Pt, it was found that the Pt is deposited as PtO_2 or in a Pt–Ti–O complex. After annealing, metallic Pt in the form of nanoparticles was observed via transmission electron microscopy (TEM). Only TiO_2 in the rutile form was observed with Pt nanoparticles created by co-sputtering.

We have synthesized the Pt/TiO_2 nanocomposite, but from single bi-combinant target materials using pulsed laser deposition (PLD). In dramatic contrast to the co-sputtering study, X-ray photoelectron spectroscopy (XPS) surface analysis and TEM diffraction analysis of PLD samples indicate that at all concentrations, metallic Pt is deposited. Further, from x-ray diffraction (XRD) analysis it was observed that both the anatase and rutile forms of TiO_2 are synthesized after annealing. At the same time, XPS depth profiling of a nanocomposite sample displays a homogenous thin film with constant atomic concentrations and chemical states.

Pt/TiO_2 bi-combinant targets with 5%, 10%, and 20% Pt by weight were created from platinum powder and 99.9% anatase, sintered at 900°C. The third harmonic (355 nm) of a Nd:YAG laser is utilized as an ablation source, generating intensities of 1.7, 3.4, and 5.7 J/cm^2. The experimental PLD chamber consists of a planetary support system which holds and rotates the bi-combinant targets during the ablation process. The 300–400 nm thin films are deposited at ambient temperature on quartz substrates. Both "as deposited" and "annealed" sample thin films were analyzed independently.

It was found that optimal nanoparticle formation and film growth occur in an oxygen environment of ~0.01 Torr. To understand the effects of laser intensity and target composition on the chemical states and distribution of Pt on the thin films, comprehensive XPS surface surveys of all samples were conducted. In all cases, only the metallic form of Pt was detected. Figure 3.1(a) summarizes these results. In "as-deposited" films the Pt/Ti surface ratio is more strongly dependent on the initial %Pt in the target than on laser intensity. In the annealed samples, the Pt/Ti surface ratio decreases, but is more or less constant for all targets and intensities.

This decrease in the Pt/Ti surface ratio in "annealed" samples represents an absolute drop in the surface concentration of metallic Pt, reflecting an interfacial interaction involving TiO_2 during matrix crystallization, which drives Pt below the boundary detectable by surface XPS. XPS depth profiling (from surface to substrate) of this annealed Pt/TiO_2 nanocomposite thin film is shown in Fig. 3.1(b). Consistent with the surface survey, the XPS depth profile of metallic Pt in terms of estimated atomic concentration can be summarized as rising from near zero at the surface to ~5% throughout the nanocomposite thin film.

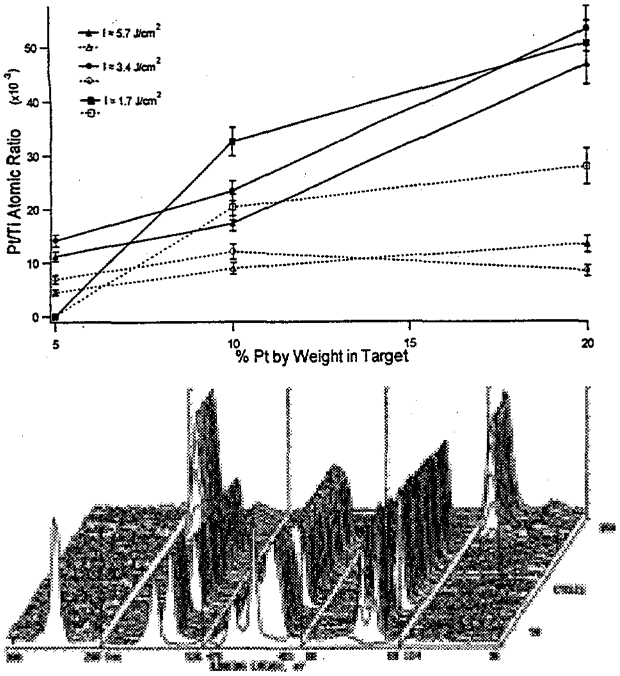

Figure 3.1. (a, above) Summary of XPS surface surveys. Errors bars indicate a 12% and 10% confidence limit for "annealed" (dotted lines and open markers) and "as-deposited" (solid lines and markers) sample values, respectively. (b, below) Depth profiling was begun at the surface of thin films where adventitious carbon, C(1s), is observed, and ended at the substrate surface with the appearance of Si peaks. Here, the thin film was produced from the 20% Pt bi-combinant target at an intensity of 5.7 J/cm^2. From left to right: C(1s), O(1s, SiO_2), O(1s, TiO_2), Ti(2p^3), Pt(4f^7), Si (2p^3). Throughout, constant-area peak signals and atomic concentrations of the components were recorded. The deformation in the Ti(2p3) peaks results from known X-ray induced state changes.

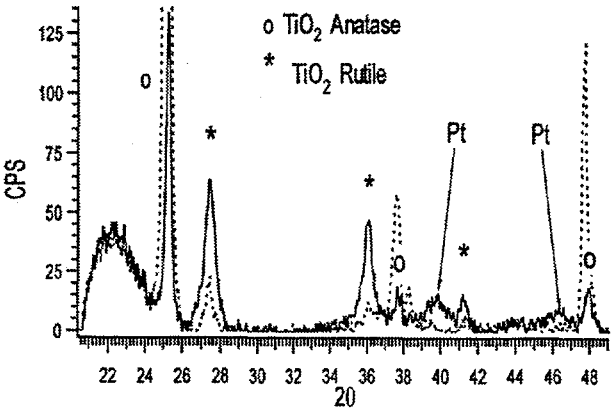

Figure 3.2. The wide angle XRD spectrum of an annealed pure TiO_2 thin film (dotted line) displays the extremely strong and narrow crystal anatase peaks, which are readily apparent as the dominant species. The spectrum of a Pt/TiO_2 nanocomposite thin film (solid line) produced from the 20% Pt bi-combinant target at an intensity of 5.7 J/cm^2 again shows the predominant crystal species is anatase.

Figure 3.2 shows the XRD spectrum of the "annealed" Pt/TiO_2 nanocomposite thin film, indicating that the predominant crystal species is anatase TiO_2. A significant amount of rutile TiO_2 is also visible, with broader peaks than the anatase, indicating smaller particle dimensions. The large breadth of the crystal Pt peak near $2\theta = 40$ is characteristic of nanocrystals. An "annealed" thin film created under similar conditions from a target of 99.9% anatase is >95% anatase. As the laser intensity decreased, the ratio of anatase to rutile TiO_2 decreased in all samples containing Pt, with TiO_2 becoming completely rutile in thin films created at 1.7 J/cm^2. It was also observed that rutile particle formation only occurs in the presence of Pt metal.

TEM images were obtained for both "annealed" and "as-deposited" nanocomposite thin films created under these latter conditions, Fig. 3.3. The image has been processed to enhance the diffraction effect caused by a single electron as it transits the nanoparticle. The cross-hatched pattern represents two different crystal planes within an apparently cubic structure (Pt has a cubic crystal structure). The dominant pattern displays a plane separation of $d(\text{Å}) = 2.27$, in good agreement with standard Pt(111) pattern analysis. The weaker pattern was observed on the edge of instrument resolution; it displays $d(\text{Å}) \sim 2.00–1.92$, compared to the standard Pt (200) pattern of $d(\text{Å}) = 1.96$.

UV-visible spectra of the "as-deposited" thin films show nearly complete absorption, a result of TiO_2 defects which are removed through annealing. Shown in Fig. 3.4(a) are the spectra of "annealed" nanocomposite films, where a is the absorption coefficient and ΔE is the bandgap. The optical bandgap can be estimated by extrapolating the linear portion of the curve to $a^2 = 0$. For the anatase film, we obtain a value of $\Delta E = 3.15$ eV, which compares favorably with recent literature values

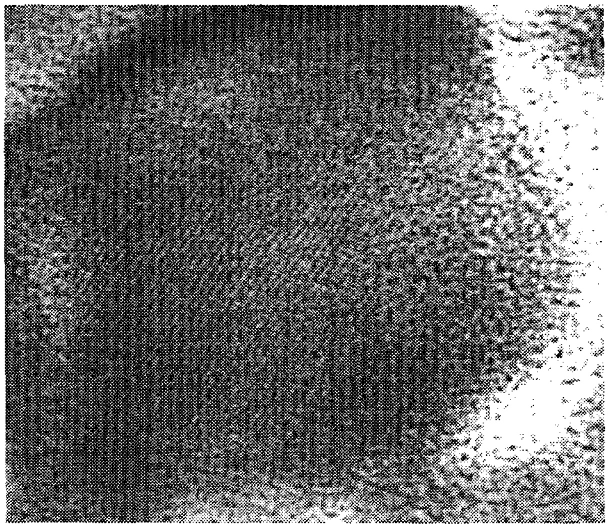

Figure 3.3. A TEM enlargement of a single Pt nanoparticle.

for single crystal anatase. The bandgap estimates for Pt/TiO_2 films created from the 5% and 10% Pt targets (2.9 eV and 2.8 eV, respectively) show little relative variation in relation to Pt concentration and an absolute change from the TiO_2 thin film bandgap that might be expected from impurity doping alone. In contrast, the bandgap for the nanocomposite film synthesized from the 20% Pt target shows a dramatic drop of >26%, to less than 2.3 eV. It should be noted that while this nanocomposite film exhibits an optical bandgap at >540 nm in the green portion of the visible spectrum, no clear optical absorption peak was observed here. A small absorption cross-section for surface plasmon resonances of Pt nanoparticles is indicated.

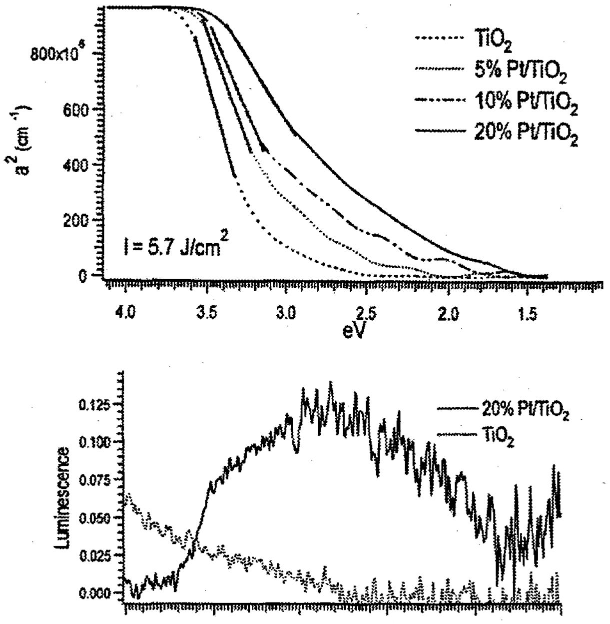

Figure 3.4. (a, above) The UV-visible spectra of "annealed" nanocomposite thin films (laser intensity = 5.7 J/cm^2) plotted as the square of the absorption coefficient vs. energy. (b, below) Photoluminescence emission of Pt/TiO_2 thin film nanocomposites at T = 24 K. The anatase film (dotted line) is displayed over the same range.

Displayed in Fig. 3.4(b) is the photoluminescence of this Pt/TiO_2 film, recorded at T = 24 K, with the 300-K background subtracted. For comparison, the anatase film spectrum is also shown (dotted line). Broad-band emission is produced only by the Pt/TiO_2 nanocomposite film as observed 680–800 nm, and is not seen in the pure anatase film or the other Pt/TiO_2 films. Similar emission was previously observed from high concentration (Pt/Ti = 0.18) co-sputtered Pt/TiO_2 nanocomposite films with Pt nanoparticles 5–10 nm in diameter.[6] in that study, a large feature that peaked at 700 nm (fwhm ~70 nm) was recorded with a trailing edge ending at ~800 nm, apparently highly dependent on nanoparticle size.

Under the conditions of these experiments, deposited Pt concentrations are more strongly dependent on the initial %Pt in the target than on the laser intensity. However, only the PLD of the 20% Pt target at a laser intensity of 5.7 J/cm^2 produced a nanocomposite thin film detectable via XRD, indicating the presence of an energetic process necessary for nanoparticle formation. Recent research into the evolution of ablation plumes with various gases and pressures suggests that the 0.01-Torr O_2 found optimal here for nanocomposite film synthesis is too low to provide a collision frequency sufficient for nanoparticle formation in the PLD plume.[7]

However, nanoparticles may grow via rapid surface diffusion. TEM shows that Pt nanoparticles are present before annealing. A mechanism in which Pt clusters are created in the plume, then deposited, and through surface diffusion rapidly form nanoparticles seems probable. In terms of Pt nanoparticle formation, the primary role of higher laser intensity during ablation appears to be in providing sufficient translational energy to ejected

Pt so that Pt clusters of a requisite size, and thus capable of acting as nanoparticle precursors, can reach the substrate surface. This seems consistent with a recent model for ablation plume propagation, splitting, and nanoparticle formation dynamics. The initial morphology of deposited Pt (atoms, clusters, particles) and TiO_2 (continuous film, particles) affecting their matrix interaction during thin film formation is currently under investigation.

In conclusion, nanocomposite films can be created with the anatase form of TiO_2 being the dominant crystal structure. The Pt nanoparticles are ~30 nm in diameter and homogeneously distributed. These thin films exhibit an optical bandgap below 540 nm and photoluminescence emission 680–800 nm. It appears that an interfacial or surface state(s) between the homogeneously dispersed Pt nanoparticles and the TiO_2 matrix produce new energy levels within the bandgap of TiO_2.

References

1. S.-D. Mo and W. Y. Ching, *Phys. Rev. B* **51**, 13023 (1995).
2. H.-A. Durand, J.-H. Brimaud, O. Hellman, H. Shibata, S. Sakuragi, Y. Makita, D. Gesbert, and P. Meyrueis, *Appl. Surf. Sci.* **86**, 122 (1995).
3. S. Tabata, H. Nishida, Y. Masaki, and K. Tabata, *Catal. Lett.* **34**, 245 (1995).
4. L. Avalle, E. Santos, E. Leiva, and V. Macagno, *Thin Solid Films* **219**, 7 (1992).
5. T. Sasaki, R. Rozbicki, Y. Matsumoto, N. Koshizaki, S.-Ya. Terauchi, and H. Umehara, *Material Res. Soc. Symp. Proc.* **457**, 425 (1997).
6. T. Sasaki, N. Koshizaki, S.-Ya. Terauchi, H. Umehara, Y. Matsumoto, and M. Koinuma, *Nanostructured Materials* **8**, 1077 (1998).
7. D. B. Geohegan, A. A. Puretzky, G. Duscher, and S. J. Pennycook, *Appl. Phys. Lett.* **72**, 2987 (1998).

Femtosecond Laser-Induced Desorption of Positive Ions from Ionic Solids

R. M. Williams, K. M. Beck,*
A. G. Joly, J. T. Dickinson,†
and W. P. Hess

Supported by DOE Office of Basic Energy Sciences.

*Postdoctoral Research Fellow.
†Washington State University.

Environmental samples are often difficult to analyze for possible contamination, requiring sophisticated analytical techniques. Some of these techniques rely upon laser ablation as a primary means of vaporization and/or ionization. They include matrix-assisted laser desorption/ionization (MALDI) and laser assisted mass spectrometry (LAMS). Generally, nanosecond lasers have been used as the irradiation source for laser desorption and ablation; however, many of the key processes (i.e., electron/hole–pair recombination, trapping, electron/phonon interactions, etc.) involved in laser/solid interactions occur on a sub-nanosecond time scale. An important first step in optimizing methods based on laser desorption/ablation lies in the understanding of these fundamental processes. The goal of this research effort is to study how these important aspects are involved in energetic desorption of ions from surfaces during and after laser/solid interactions, where the solid material is usually an environmentally relevant wide-band-gap material, such as magnesium oxide, calcium carbonate or sodium nitrate.

We use time-of-flight mass spectrometry (TOF-MS) to study the ions desorbed from an MgO or $CaCO_3$ crystal following fs and ns UV laser irradiation. In a typical experiment, a freshly cleaved (in air) 1 × 1 × 0.2-cm sample of single crystal MgO(100) or $CaCO_3$ is mounted on the sample holder in an UHV apparatus. The freshly cleaved and baked samples are irradiated with UV laser pulses that illuminate the sample at an angle of incidence of 60° with respect to the surface normal. Positive ions are extracted and accelerated into the Wiley-McLaren TOF-MS, and detected with a microchannel plate assembly. Two different laser systems are employed in this experiment, providing either nanosecond or subpicosecond pulses. Subpicosecond UV pulses are produced in an amplified femtosecond titanium-sapphire (Ti:sapphire) based laser system operating at a fundamental wavelength of 795 nm. A cw pumped, mode-locked Ti:sapphire oscillator, producing <100-fs pulsewidths at a repetition rate of 82 MHz, is used to seed the Ti:sapphire amplifier (pumped at 20 Hz by the frequency-doubled output of a Q-switched Nd:YAG laser), which increases the energy of the femtosecond pulses to ~10 mJ/pulse in a regenerative and linear double-pass amplifier arrangement while maintaining pulsewidths of ~130 fs. The amplified output is doubled and tripled in KDP crystals producing up to 1.1 mJ/pulse at 265 nm.

Figure 3.5 depicts a series of time-of-flight mass spectra from MgO recorded using UV nanosecond pulses over a fluence range of 1–15 mJ/cm^2, where the illuminated surface area was estimated to be 0.28 cm^2. No other significant features, other than the ones depicted, are found in the TOF spectra. The two largest peaks, occurring at ~6.5 and 8.5 μs, are identified as Mg^+ and MgO^+, respectively. A small feature at 7.1 μs remains unidentified, but has a m/z ratio (28) consistent with $(MgO_2)^{2+}$. The data show two distinct trends with increasing fluence.

The first is a transition from a fluence region dominated by the desorption of MgO^+ to a region where Mg^+ has the largest contribution. At the lowest nanosecond fluence studied here (~1 mJ/cm^2), MgO^+ is the *only* detected desorption product. This trend is similar to that reported by Kreitschitz et al.[1] for desorption products from MgO following 193-nm irradiation (17-ns pulsewidth). At low fluences MgO^+ dominates and at roughly 3–4 mJ/cm^2 Mg^+ signal begins to grow in; as the fluence continues to increase the relative ratio of MgO^+ to Mg^+ decreases dramatically and approaches unity over this range of fluence. There is no clear trend in the increasing versus decreasing fluence data, indicating that little surface modification has occurred during the experiment. The Mg^+ yield has a P^2 dependence, while the MgO^+ has a P^4 dependence, implying different desorption mechanisms, or possibly different initial sites needed for these two species.

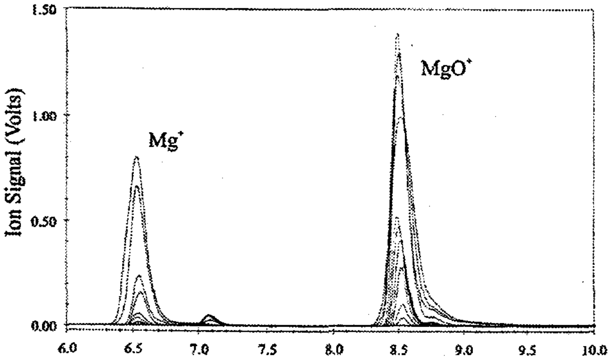

Figure 3.5. A series of time-of-flight mass spectra from MgO recorded using 3-ns, 266-nm laser pulses (sum of 2500 laser shots/trace) over a fluence range of 1–15 mJ/cm^2. Only a portion of each TOF spectra is represented, as no other significant features are found to be present in the TOF spectra.

The second notable trend found in Fig. 3.5 is the initial breadth of the TOF features and broadening and shifting of Mg^+ and MgO^+ peaks with increasing fluence. Additionally, it is found that with increasing fluence the arrival times (defined as the peak of the distribution) of the Mg^+ peaks decrease by as much as 80 ns while broadening from a fwhm of 60 ns to 175 ns. This is seen on Fig. 3.5 as the broadest (but not the most intense) peak associated with MgO^+. The initial shape and dynamic evolution of the TOF profiles as a function of fluence will require additional investigation to clarify the mechanism; however, the spreading of the distribution likely results from electrostatic interactions between the particles (positive ions) themselves and perhaps the surface. Ermer et al.[2] have studied the photoelectron emission from MgO which accompanies positive-ion emission following 248-nm (30-ns pulsewidth) irradiation, and it is suggested that complex Coulombic interactions exist between the desorbing positive ions and the photoelectrons.

Figure 3.6 displays the time-of-flight spectra recorded following subpicosecond exposure. The fluence range covered here extends from ~0.3–1.1 mJ/cm^2, where the illuminated surface area is ~0.21 cm^2. Several significant differences between the nanosecond spectra shown in Fig. 3.5 and the subpicosecond spectra shown in Fig. 3.6 are seen.

First, the addition of H^+ and Mg^{2+} to the mass spectra in the subpicosecond excitation case is significant. The appearance of Mg^{2+} by itself is not surprising, as it may be rationalized in terms of an enhanced state of ionization present at the surface during or subsequent to the intense subpicosecond irradiation. However, the unexpected appearance

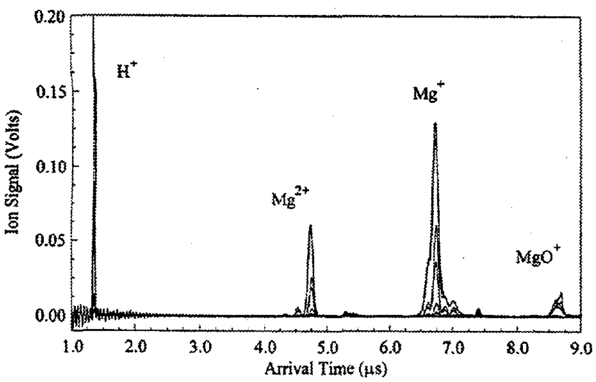

Figure 3.6. Series of summed (2500 shots) time-of-flight mass spectra generated by a irradiating a MgO surface with 265-nm, subpicosecond laser pulses over a fluence range of 300 μJ/cm^2 to 1.1 mJ/cm^2. Only the relevant portion of TOF spectra are shown for clarity. The ringing present at early times results from scattered UV laser light striking the surface of the microchannel plate detector.

of H$^+$ is interesting. The MgO surface could possibly contain a sufficient quantity of hydrogenated sites as to account for the observed H$^+$ signal. A hydroxylated surface may result from dissociative adsorption of water on the freshly cleaved surfaces prior to mounting and baking in the vacuum assembly. Recent synchrotron X-ray photoemission studies of the reaction of water with MgO(100) at 300 K by Liu et al.[3] conclude that water dissociatively adsorbs on MgO at defect sites initially, and subsequently on terrace sites present on cleaved surfaces, forming a hydroxylated surface on which additional waters may physisorb.

The minimal broadening of the peaks in Fig. 3.6 compared to the extensive broadening found in Fig. 3.5 is also noteworthy. This lack of broadening of the main assigned features allows for the detection of many "satellite" peaks found on either side of Mg^{2+} and Mg$^+$. These unassigned features remain the focus of our current experimental thrusts, and plans are underway to perform similar desorption measurements in an ion trap mass spectrometer to insure that these unexplained features are not the result of an experimental artifact. Finally, the surprising observation that the initial detection-threshold for desorption is roughly equivalent (within a factor of 2 or 3 rather than the orders of magnitude change that might be expected based upon a multiphoton absorption description) for both nanosecond and subpicosecond exposure, strongly suggesting a similar "initiation" step for both conditions which depends on fluence and not irradiance.

References

1. O. Kreitschitz, W. Husinsky, G. Betz, and N. H. Tolk, "Laser induced desorption of ions from insulators near the ablation threshold," *Nucl. Instr. Meth.* **B78**, 327–332 (1993).

2. D. R. Ermer, S. C. Langford, and J. T. Dickinson, "Interaction of wide band gap crystals with 248-nm excimer laser radiation. V. The role of photoelectronic processes in the formation of a fluorescent plume from MgO," *J. Appl. Phys.* **81**, 1495–1504 (1997).

3. P. Liu, T. Dendelewicz, G. E. Brown Jr., and G. A. Parks, "Reaction of water with MgO(100) surfaces. Part I: Synchrotron X-ray photoemission studies of low-defect surfaces," *Surf. Sci.* **412/413**, 287–314 (1998).

Photochemistry and Product Structures of Matrix-Isolated Acetyl Chloride

J. B. Rowland,* P. R. Winter,† G. B. Ellison,† and W. P. Hess

Supported by DOE Office of Basic Energy Sciences.

*Postdoctoral Research Fellow.
†Department of Chemistry and Biochemistry, University of Colorado.

We use Fourier transform infrared (FTIR) absorption spectroscopy to study the photodynamics of matrix isolated acetyl chloride irradiated at 248 nm and 266 nm, and to determine the product structures. Significant changes in IR band center frequencies and integrated intensities are observed for hydrogen-bonded molecules such as H_2O and HCl. Frequency bandshifts and absorbtivity enhancements can be used as a probe of intermolecular bonding in matrix-isolated photoproduct complexes. By using the HCl bandshift as a probe, we can assign structures to product complexes in various matrices. Previously, polarized infrared spectroscopy was used to study the orientation of HCl•ketene complexes in argon matrices. We argued that the complex structure is roughly T-shaped, with the hydrogen of HCl bonded to the methylenic carbon of ketene (Fig. 3.7). Structure 1

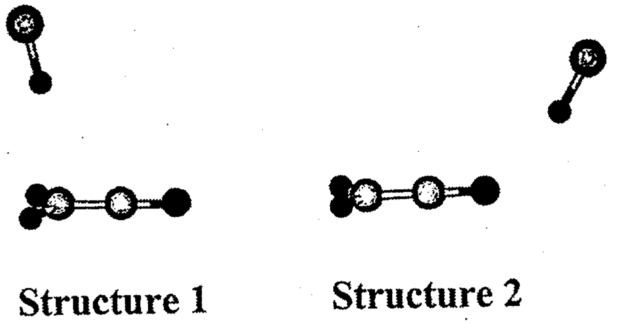

Figure 3.7. Structures **1** and **2** of the HCl•ketene complexes. IR spectra assigned to both structures **1** and **2** are observed in xenon matrices; only IR bands assigned to structure **1** are observed in argon matrices. Structures are as calculated in Ref. 1.

also corresponds to the most stable dimer geometry predicted by *ab initio* calculations.[1] however, another stable hydrogen-bonded dimer geometry exists. This second structural minimum involves the hydrogen of HCl bonding to the oxygen of ketene. Here, we assign the structures of HCl•ketene complexes for the 248-nm and 266-nm photoreaction of acetyl chloride in xenon and argon matrices.

We deposit matrix-isolated thin films of acid chlorides onto KBr and BaF_2 substrates cooled to about 20 K by a closed-cycle helium cryostat. The matrix-isolated samples have a concentration of 300:1 argon to acid chloride. All acid chloride samples were obtained from commercial vendors at stated purities of 99% or greater. Matrix-isolated deposits are irradiated at 248 nm and 266 nm, using the emission from an excimer laser or the fourth harmonic of a Nd:YAG laser. Infrared spectra are collected at a resolution of 2 cm^{-1} before and after irradiation at 248 and 266 nm.

For argon matrix-isolated acetyl chloride irradiated at 248 nm, the IR band of the HCl•ketene dimer is centered at 2686 cm^{-1} (Fig. 3.8). This absorption band has previously been assigned to the HCl stretch of structure **1**.[2] Other experimental evidence to confirm the assignment of the dimer geometry is the center frequency of the ketene C=O stretch band at 2142 cm^{-1} (Fig. 3.9) that is identical to that of argon matrix-isolated non-complexed ketene.[3] Thus, we would expect the C=O center frequency to be shifted if structure **2** were formed. The lack of frequency shift of the C=O stretch band is attributed to the lack of hydrogen bonding to the ketene oxygen (structure **1**).

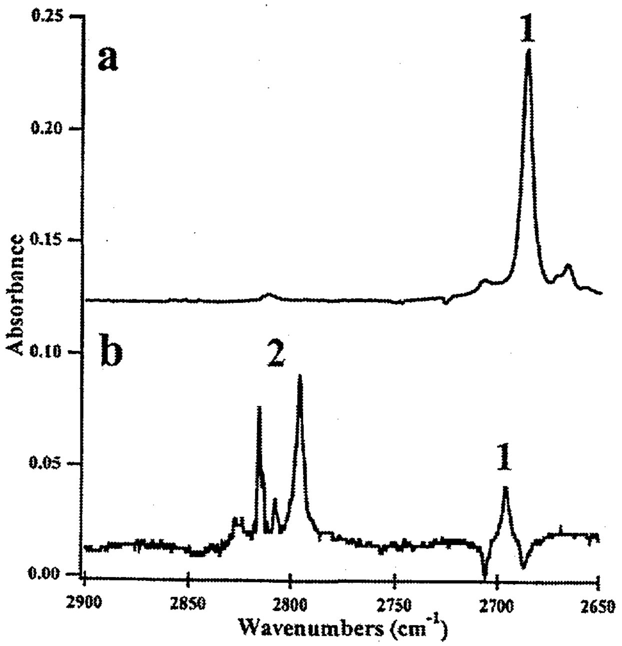

Figure 3.8. Infrared difference spectra of the HCl region in HCl•ketene complexes following 248-nm irradiation of acetyl chloride in argon (a) and in xenon (b) matrices. The HCl band centers assigned to structures **1** and **2** are marked.

We find distinct differences between HCl•ketene spectra in argon versus xenon matrices. Spectral differences between the argon and xenon samples are due in part to different intermolecular bonding in HCl•ketene complexes that we will show to correspond to structures **1** and **2**. In a xenon matrix, HCl IR bands are observed at 2696 cm^{-1} and 2798 cm^{-1}. Similarly, two ketene C=O stretch bands are observed at 2142 cm^{-1} and 2134 cm^{-1}. The HCl and C=O stretch bands at 2696 cm^{-1} and 2142 cm^{-1} are assigned to structure **1** as observed in argon matrices. The HCl and C=O stretch bands at 2798 cm^{-1} and 2134 cm^{-1} are attributed to structure **2** as observed in xenon matrices. Experimental and calculated frequency shifts for structures **1** and **2** are given in Table 3.1.

The effects of hydrogen bonding on vibrational modes have been experimentally and theoretically studied,[4,5] and show a general trend that correlates hydrogen-bond strength to shifts in infrared frequencies and band intensities. Generally, the greater hydrogen-bond strength, the greater the red shift of IR band centers, the greater the integrated IR intensity, the greater the molecular bond

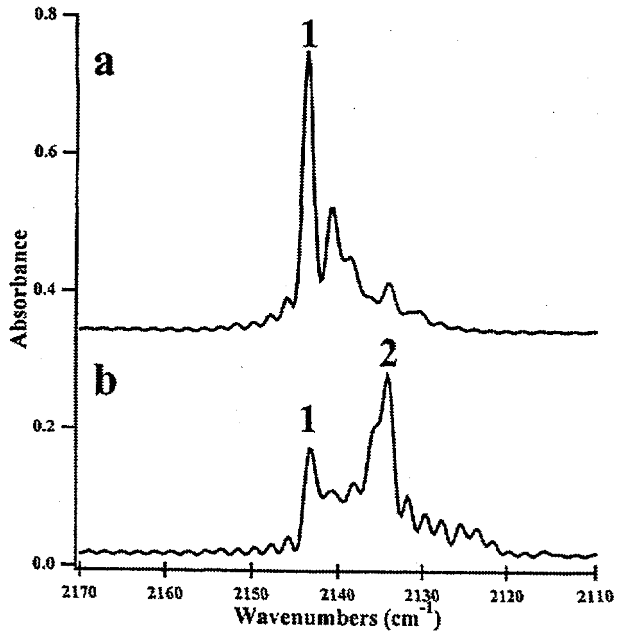

Figure 3.9. Infrared difference spectra of the ketene C=O stretch region in argon (a) and xenon matrices (b). The C=O stretches assigned to structures **1** and **2** are marked.

length, and the lesser the hydrogen-bond length. These trends have been observed in the *ab initio* electronic structure study of the complexes displayed in Fig. 3.7.[1]

As seen in Table 3.1, the 206 cm^{-1} red shift from calculated frequencies of free to complexed HCl agrees well with our measured red shift of 202 cm^{-1}. Furthermore, no hydrogen bonding occurs on the oxygen of structure **1**, which results in no change between the matrix-isolated and observed dimer frequencies at 2142 cm^{-1}.[3] The assignment of structure **2** to the HCl•ketene complex found in xenon matrices is based on comparing experimental red shifts of the HCl and ketene C=O stretches to calculated values. The HCl IR bands are red-shifted by 55 cm^{-1} from the xenon matrix-isolated HCl frequencies, in good agreement with the calculated value of 50 cm^{-1} from the free to complexed HCl frequencies (Table 3.1). The C=O stretch frequency is useful for assigning structure **2** because it can be used to probe the position of the hydrogen bond along the ketene molecule. In structure **2**, the oxygen of ketene is involved in a hydrogen bond, which results in red-shifting the C=O stretch band. An experimental red shift of 9 cm^{-1} is observed, which closely agrees with the calculated red shift of 8 cm^{-1}.

Table 3.1. Experimental and calculated band shifts of the C=O ketene stretch and HCl IR band centers for structures **1** and **2**. Experimental band shifts are determined by comparison of matrix-isolated monomer and complex center frequencies. Calculated shifts are obtained from Ref. 1, and are determined from free monomer and complex center frequencies.

Structure / band	$\Delta\nu$ expt. (cm^{-1})	$\Delta\nu$ theor. (cm^{-1})
1 / C=O stretch	0	2
2 / C=O stretch	9	8
1 / HCl	202	206
2 / HCl	55	50

Both structures **1** and **2** are formed in xenon matrices following 248-nm and-266 nm photoexcitation of acetyl chloride. Structure **1** represents the global minimum, with a binding energy of 1.37 kcal mol^{-1}, and structure **2** corresponds to local minimum with a binding energy of 0.71 kcal mol^{-1}.[1] It is interesting that most of the complexes in xenon matrices are the less stable structure **2**. It is possible that the differences in lattice spacing are responsible for the preponderance of structure **2**. Argon matrices have a unit cell spacing of ~5.4 Å with a nearest neighbor distance of ~3.8, Å compared to xenon, which has a unit cell spacing of ~6.2 Å with nearest neighbor distance of ~4.4 Å. The photoreaction of acetyl chloride in argon has less volume available for the photoproducts. Photoreactions in xenon matrices have more space for molecular rearrangement, such that other HCl•ketene structures and little polarization dependence are expected. This is experimentally observed for both 248- and 266-nm photoreactions in xenon matrices.

References

1. R. Sumathi and A. K. Chandra, *Chem. Phys. Lett.* **271**, 287 (1997).
2. B. Rowland and W. P. Hess, *J. Phys. Chem. A* **101**, 8049 (1997).
3. C. B. Moore and G. C. Pimentel, *J. Phys. Chem.* **38**, 2816 (1963).
4. G. C. Pimentel and A. L. McClellan, *The Hydrogen Bond* (Freeman, San Francisco, 1960).
5. L. Ojamae and K. Hermansson, *J. Phys. Chem.* **89**, 4271 (1994).

The UV Photodissociation of Matrix-Isolated Propionyl Chloride

P. R. Winter, J. B. Rowland,† W. P. Hess, J. G. Radziszewski,§ M. R. Nimlos,§ and G. B. Ellison**

Supported by DOE Office of Basic Energy Sciences.

*Department of Chemistry and Biochemistry, University of Colorado.
†Postdoctoral Research Associate
§National Renewable Energy Laboratory, Golden, Col.

The UV photodissociation of the most elementary acid chloride (RCH_2COCl), acetyl chloride CH_3COCl ($R = H$), has been previously studied in both the gas and solid phases. The photoproducts are found to depend on the initial phase of the reactant. In the gas phase, U V excitation of CH_3COCl at 236 nm results in cleavage of the C–Cl bond and the formation of Cl and CH_3CO as the primary products, while photoexcitation in the condensed phase at 266 nm leads to an elimination reaction forming ketene, CH_2CO, and HCl.

To further understand the mechanism for the condensed phase photodecomposition of acid chlorides, we have used FTIR spectroscopy to probe the photodecomposition products of ppropionyl chloride, CH_3CH_2COCl, in an Ar matrix at 10 K following irradiation at 248 nm, 254 nm and 266 nm. The only observed products are methyl ketene and hydrochloric acid.

CH_3CH_2COCl vapor was mixed with argon gas in amounts ranging from 0.256–0.626% and deposited on a CsI window which was held at 30 K during the deposition and then cooled to 10 K after the deposition was completed. After recording an initial IR spectrum, the matrix was irradiated with 254-nm photons from one or two mercury vapor lamps, or 248 nm from an excimer laser. Spectra were collected at regular intervals during the irradiation, until the propionyl chloride peaks were no longer observed. A spectrum of the products was obtained by subtracting the initial spectrum from the final spectrum; the product bands appear as positive features and the precursor bands as negative features in the difference spectrum. This spectrum was then analyzed to identify the irradiation products.

The IR absorption spectrum of CH_3CH_2COCl in an Ar matrix is shown in Fig. 3.10. Our assignments are based on literature assignments in the gas and solid phases[1] and were checked by comparison with spectra of CH_3CH_2COCl vapor at 1.7 Torr in a 10-cm cell. IR spectra of the matrix before and after irradiation at 266 nm are shown in Fig. 3.11. The CH_3CH_2COCl peaks are almost totally absent following two hours irradiation at 0.1 W, 20 Hz of 266-nm radiation. The duration of the irradiation in these experiments varied from several hours to overnight, depending on the initial matrix, but in all cases near complete decomposition could be achieved. Longer irradiation (including up to several days at 254 nm) resulted in no further change.

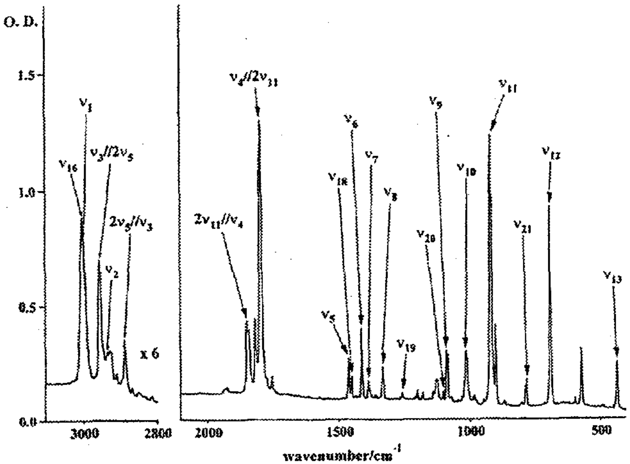

Figure 3.10. IR absorption spectrum of propionyl chloride, CH_3CH_2COCl, in argon matrix at 10 K.

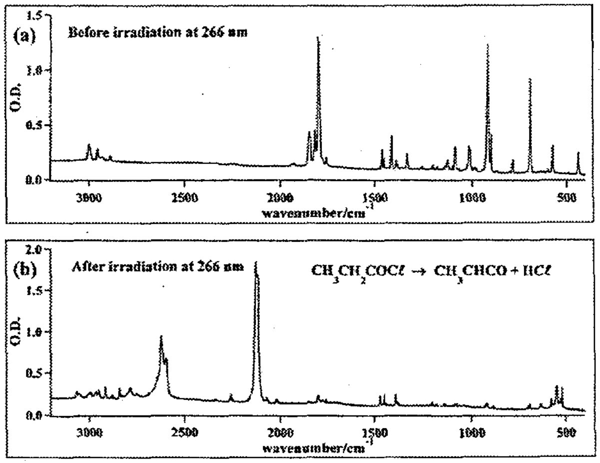

Figure 3.11. IR absorption spectrum of (a) propionyl chloride in argon matrix before irradiation; and (b) the product matrix following irradiation at 266 nm.

All of the trials showed the strongest product peak at 2130 cm^{-1}, close to the value of 2125 cm^{-1} reported[2] for the carbonyl stretch of $CH_3CHC{=}O$ in an Ar matrix. All of the trials also contained a broad doublet at 2597 cm^{-1} and 2619 cm^{-1}. We attribute this feature to HCl in a [$CH_3CH{=}C{=}O$, HCl] complex; an analogous [$CH_2{=}C{=}O$, HCl] complex was observed[3] at 2679 cm^{-1} in the acetyl chloride photoproducts, red-shifted from the isolated HCl monomer in an Ar matrix at 2860 cm^{-1}. Numerous other features were also consistently evident in the product spectrum. The difference spectrum following 254-nm irradiation of CH_3CH_2COCl is shown in Fig. 3.12. The fundamental bands for methyl ketene have been assigned based on the partial assignments of Harrison and Frei[2] for methyl ketene in an Ar matrix and our *ab initio* electronic structure calculations.[4]

A B3LYP/cc-pVDZ electronic structure calculation was carried out using the Gaussian 94 suite of *ab initio* electronic structure codes to determine the geometry and identify the harmonic frequencies of methyl ketene. A calculation of the same type was performed for ketene for the purposes of evaluating the accuracy of the methyl ketene calculation. Our unscaled harmonic frequencies are within a few percent of the experimental values for both the methyl ketene and the ketene. Based on these calculations, a symmetry was assigned for each mode ($CH_3CH{=}C{=}O$ has C_s symmetry). The polarization data and product spectra from the irradiation of CH_3CD_2COCl were used to confirm the assignments for these modes.[4]

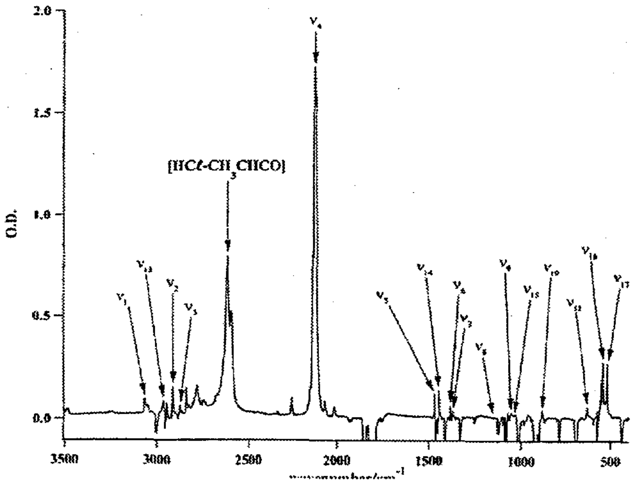

Figure 3.12. Difference spectrum showing the product features as positive peaks and the precursor features as negative peaks.

Photolysis of the selectively deuterated species CH_3CD_2COCl was studied to search for HCl produced by a β-abstraction or elimination process. Irradiation at 254 nm produced only DCl as a product, with no trace of either free HCl or the [$CH_3CH{=}C{=}O$, HCl] complex, thus confirming that only an α-elimination channel is active.

There are several conceptually different pathways by which an acid chloride (RCH_2COCl) could photodissociate in an Ar matrix: (1) a multi-step process proceeding through a radical pair, with the first step identical to the gas-phase fragmentation, followed by a radical–radical reaction; (2) a direct elimination following the initial photoexcitation; or (3) fragmentation into an ion pair, followed by ion–ion chemistry. For acetyl chloride, only the radical-pair mechanism may lead to products other than those observed in the condensed phase, and the ion pair mechanism is deemed unlikely based on energetic arguments.

Polarization studies were conducted to determine the relative orientation of the product methyl ketene and HCl molecules in the Ar matrix. Following irradiation with linearly polarized 266-nm light, IR absorption spectra of the matrix were recorded using IR light polarized at various angles to the polarization axis of the initial irradiation. Since the product molecules no longer have an isotropic distribution, the IR absorption for a given mode will vary as the polarization angle of the IR light changes. Thus the nomalized integrated peak area for an IR feature plotted as a function of the IR polarization angle can tell us about the orientation of the dipole moment for that absorption relative to the initial polarization axis. Figure 3.13 shows these curves for several of the stronger product absorptions, including the methyl ketene ν_4 C=C=O stretching mode at 2130 cm^{-1} and the HCl stretch around 2600 cm^{-1}. The data are fitted with the functional form, $I(\theta) = A\cos^2(\theta) + B$, where constants A and B relate to the average angle of the IR transition dipole to the z-axis in the oriented matrix. The dipole for ν_4 is seen to be aligned at right angles to the HCl dipole. The calculations indicate that the transition dipole for the ketene stretch is parallel to the C=C=O structure and in the plane of symmetry of the methyl ketene; thus the HCl molecule is oriented roughly perpendicular to this structure. It is also found that all methyl ketene IR modes assigned with in-

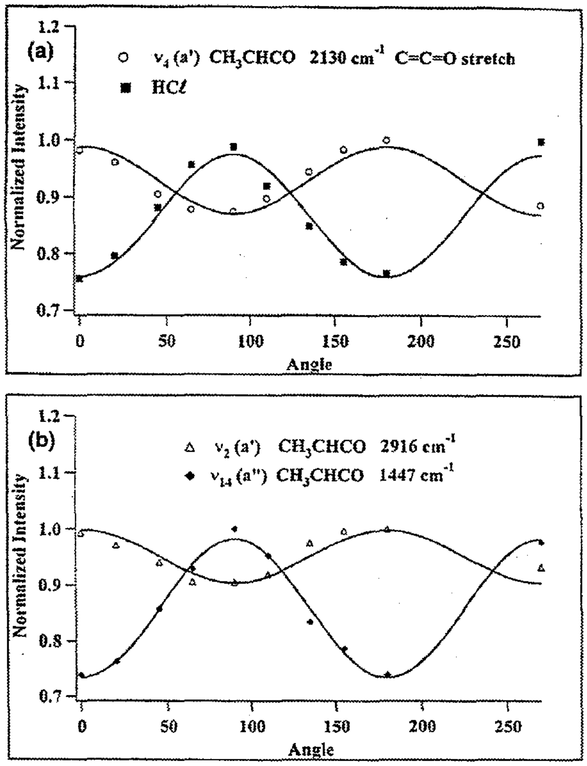

Figure 3.13. Angular dependence for CH_3CH_2-COCl and HCl modes following irradiation with linear polarized UV light. An angle of 0 degrees corresponds to the IR polarizer set along the axis of the UV laser polarization.

plane dipole transitions (A′ symmetry) have a similar angle dependence as the ν_4 mode, while the out-of-plane methyl ketene modes (A″ symmetry) behave like HCl. This suggests that the HCl molecule may be oriented perpendicular to the plane of the methyl ketene. A similar geometry has been calculated for the transition state to HCl elimination from acetyl chloride. A free chlorine abstracting a hydrogen would not be expected to produce highly oriented products; this suggests that the mechanism proceeds via an elimination pathway as opposed to hydrogen abstraction, and that no free chlorine atom is generated during the photolysis.

Since atomic chlorine is not observed in the condensed-phase acid chloride photodecomposition, the gas-phase curve crossing from a $^1(n \rightarrow \pi^*)$ state to a $^1(np \rightarrow \sigma^*)$ state must be altered by the presence of the surrounding matrix. With this channel inhibited, the system relaxes through internal conversion on a singlet surface to form a hot ground state molecule.[5] The condensed-phase chemistry for propionyl chloride may be pictured:

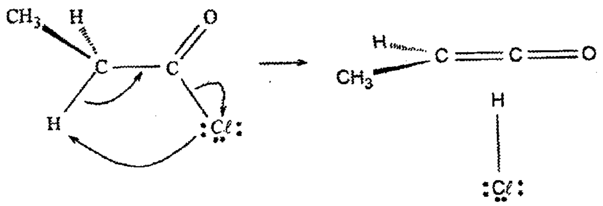

The [CH3CH=C=O, HCl] pair from the electrocyclic elimination in the matrix forms a complex that is roughly T-shaped.

References

1. S. G. Frankiss and W. Kynaston, *Spectrochim. Acta A* **31**, 661 (1975).
2. J. A. Harrison and H. Frei, *J. Phys. Chem.* **98**, 12142 (1994).
3. J. B. Rowland and W. P. Hess, *Chem. Phys. Lett.* **263**, 574 (1π996); N. Kogure, T. Ono, and F. Watari, *J. Mol. Struct.* **296**, 1 (1993).
4. P. R. Winter, J. B. Rowland, W. P. Hess, J. G. Radziszewski, M. R. Nimlos, and G. B. Ellison, *J. Phys, Chem. A* **102**, 3238 (1998).
5. J. B. Rowland and W. P. Hess, *J. Phys. Chem. A* **101**, 8049 (1997).

Experimental and Theoretical Investigations of Electron Diffraction in Stimulated Desorption

M. T. Sieger, G. K. Schenter, and T. M. Orlando*

Supported by DOE Office of Basic Energy Sciences.
*EMSL Theory, Modeling, & Simulation.

The interaction of electron beams with surfaces is a topic of interest for many disciplines, from astrophysics to semiconductor device processing. We are studying interactions of electrons with materials that involve excitation of the surface, leading to the ejection of atoms and molecules (electron-stimulated desorption, or ESD). In particular, we have been studying the role of scattering and diffraction of the incident electron. The interference of the direct electron wave with waves scattered from nearest-neighbor atoms produces an electron standing wave (ESW) field, with spatially localized maxima and minima in the incident electron density. Since the probability of the inelastic scattering event leading to desorption is proportional to the incident electron density in the immediate vicinity of the target surface atom, the ESD rate depends upon the local atomic structure and the k-vector of the incident wave. We have developed a theoretical description of this process, which we have used to calculate expected interference effects in ESD rates. In Fig. 3.14 we have plotted calculations of the expected variation in the ESD rate due to diffraction at the Si(111)-(1×1):Cl surface with electron beam incidence angle. Black denotes lowest desorption probability, white the highest. The symmetry of the surface is evident in the ESW pattern, and the patterns are different for different energies.

We have recently reported experiments verifying, for the first time, that total ESD yields from the Cl-terminated Si(111) surface show fine structure as a function of incident electron direction and energy, as predicted. In Fig. 3.15(a,b) symmetry-averaged χ-functions, characterizing the deviation in the desorption rate due to incident beam diffraction, are plotted for incident electron energies between 20 and 40 eV. Quantum-mechanical scattering and interference is expected to be a function of the electron wavelength (energy) (Fig. 3.14), and the observed fine structure is indeed dependent on energy. The measured χ-functions can then be subjected to structural analysis analogous to that used in low-energy electron diffraction or angle-resolved photoelectron diffraction. To demonstrate the structural origin of the observed fine structure, we compare our data to theoretical calculations for different bonding sites (solid lines, Fig. 3.15(a,b)). Comparison of experimental data to theoretical calculations reveals the atomic bonding geometry of the atomic site whose excitation is responsible for initiating the desorption process. A previous study of photon-stimulated desorption (PSD) of $Cl^+/Si(111)$ assigned this excitation to a Cl 3s ‡ Cl* antibonding transition. The results of a calculation assuming a Cl absorber are shown in Fig. 3.15(b), and give poor agreement with the data. A much better match between theory and experiment is obtained for an excitation localized on the Si atom bonded to Cl. On the basis of our observation, we assign the excitation responsible for Cl^+ desorption to a two-hole state localized on the Si atom. A hole is then transferred to the Cl, and the mutual Coulomb repulsion results in ejection of the Cl^+ ion.

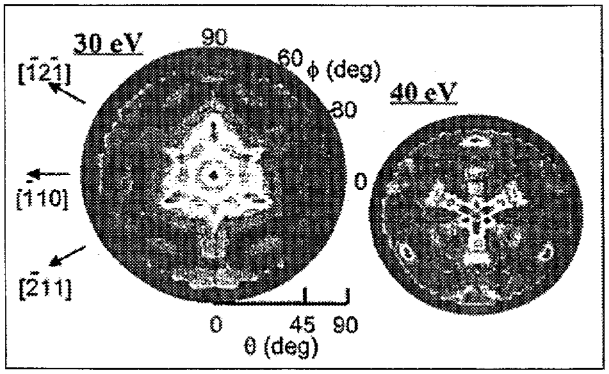

Figure 3.14. Calculated variation in ESD rate due to diffraction at the Si(111)-(1×1):Cl surface as a function of electron-beam incidence angle (θ,ϕ).

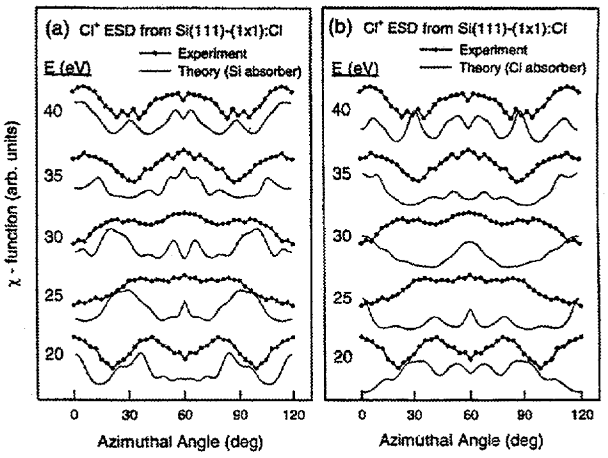

Figure 3.15. Deviations in the desorption rate due to incident beam diffraction (χ-functions) as a function of azimuthal angle for incident electron energies 20–40 eV.

The resulting picture of the role of diffraction in electron–surface scattering has implications not only for ESD, but for other surface spectroscopies as well, including Auger, EELS, and secondary electron emission. We have used our theoretical codes to carry out calculations of ESW effects for secondary electron emission from Au, and find good agreement with experimental data.

This ESW effect is potentially a very powerful tool for surface structure determination with sub-ångström resolution of bond vectors, and for illuminating the relationship between structure and excitations leading to desorption.

Electron-Stimulated Desorption and Reactive Scattering in Nanoscale Ice Films

M. T. Sieger, W. C. Simpson,**
K. A. Briggman,† and T. M. Orlando

Supported by DOE Office of Basic Energy Sciences.

*Postdoctoral Research Associate
†Visiting Graduate Student from the Department of Chemistry, Northwestern University.

1. *Crystallization of Amorphous D_2O Films Monitored by Electron-Stimulated Desorption*

D_2O ice deposited on Pt(111) at temperatures of 90–155 K forms several distinct crystalline and amorphous phases, depending on the deposition temperature and annealing history. The electron-stimulated desorption (ESD) of D^+ from these phases exhibits differences in the total yield and/or behavior as a function of ice temperature. We have completed a study in which the amorphous–crystalline phase transition is monitored by measuring the D^+ yield as a function of temperature.[1] D_2O vapor deposited at 90 K forms a porous amorphous film, while deposition at 155 K forms a cubic crystalline film. Annealing amorphous ice near 160 K results in a polycrystalline film, characterized by a lower stimulated desorption yield than amorphous or as-grown crystalline ice. However, amorphous ice deposited on an as-grown crystalline substrate crystallizes to a form with a D^+ yield similar to that of the buried film. Figure 3.16 shows the temperature dependence of the D^+ yield from an amorphous/crystalline multilayer system.

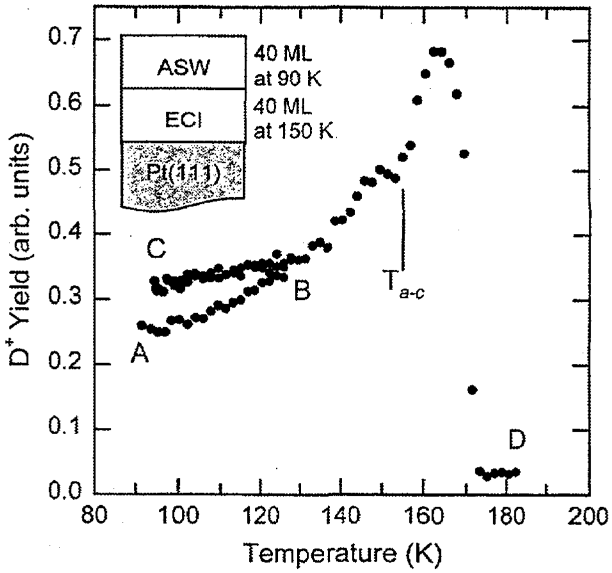

Figure 3.16. The temperature dependence of the D^+ ESD yield from an amorphous solid water and an epitaxial crystalline multilayer system. The temperature was cycled from 90 (A) to 130 (B) to 90 (C) to 190 (D) K. The irreversible increase in yield as the temperature is cycled from a–b–d strongly suggests that the overlayer is deposited as the porous polymorph. The rise in the yield following T_{a-c} suggests that the amorphous overlayer has crystallized to the epitaxial form.

The irreversible increase in yield as the temperature is cycled from 90–130–90 K, strongly suggests that the overlayer is deposited as the porous amorphous solid water (ASW) polymorph. The crystalline substrate does not appear to affect the overlayer growth, at least at the temperatures studied. Near 160 K, however, where we expect to see the yield drop, as the ASW film becomes polycrystalline, we observe only a small dip in the yield. Beyond 160 K, the yield *rises* to a value characteristic of as-grown crystalline ice, rather than a polycrystalline film. We conclude that the amorphous overlayer has crystallized to the same form as the buried film. This behavior can be understood if the energy required to form a crystalline nucleation center in amorphous ice is larger than the energy needed to add water molecules to an existing crystalline interface. These results are important for understanding the thermodynamics and crystallization kinetics of ice under various growth conditions, and serve to demonstrate the utility of ESD for measuring phase changes in ice films.

2. *Low-Energy (≤100 eV) Electron-Stimulated Desorption of Neutral $D(^2S)$ from D_2O Films on Pt(111)*

We have continued our investigations of low-energy (≤100 eV) electron-stimulated desorption and dissociation (ESD) of neutral products from amorphous and microporous D_2O films vapor-deposited on Pt(111). Resonant-enhanced multiphoton ionization (REMPI) is used to monitor the $D(^2S)$ yield as a function of incident electron energy and substrate temperature for 80-bilayer D_2O films. The ESD yield of the D atom for 100-eV incident electron energy as a function of increasing temperature for porous films shows an irreversible expulsion of D atoms from the film between 90–120 K for heating rates of at least 0.3 K/s. A similar irreversible increase in yield over this temperature range has been previously observed for the ESD of D$^+$ species from ice films, and correlated with the structural collapse of micropores in the ice substrate.[2] Our most recent results (Fig. 3.17) indicate that *neutral D atoms formed by electron irradiation can be trapped in the microporous structure of ice.* This has important implications, since the trapping and release of radicals and molecular products from porous ice may be involved in the formation of planetary atmospheres. We are exploring this further and note that irreversibility in yields has not observed for either the O or D$_2$ ESD products.

3. *D_2 Formation from D_2O Films via D^- Reactive Scattering*

The low-energy (5–15 eV) electron stimulated desorption of D$^-$ and D$_2$(${}^1\Sigma_g^+$, $v = 0$, $J = 0$ and $v = 1$, $J = 2$) from condensed D$_2$O films is investigated as a function of substrate temperature. The D$^-$ ions are produced primarily via the ${}^2B_1$ dissociative electron attachment resonance. Both the D$^-$ and D$_2$ yields are enhanced when the substrate temperature increases from 90 to 140 K. The changes in the D$^-$ and D$_2$ yields with substrate temperature are qualitatively similar, and are shown in Fig. 3.18; we attribute the increase in both the D$^-$ and D$_2$ yields to thermally-induced rotations or breaks in the near-surface hydrogen bonding network. This reduction in coordination and coupling reduces the nearest-neighbor perturbations and enhances the surface or near-surface excited-state lifetimes. Production of vibrationally excited D$_2$ molecules correlates with reactive scattering of D$^-$ at the surface,[3] whereas production of D$_2$ in the $v = 0$ level likely involves molecular elimination from an excited state which is produced by

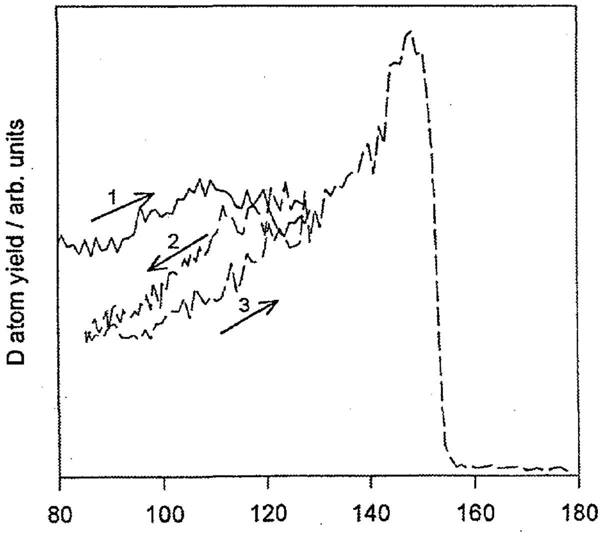

Figure 3.17. The ESD yield of D atoms as a function of substrate temperature. The heating rate was 0.5 K/s and the incident beam energy was 100 eV. Note the irreversible increase in yield between 90–120 K.

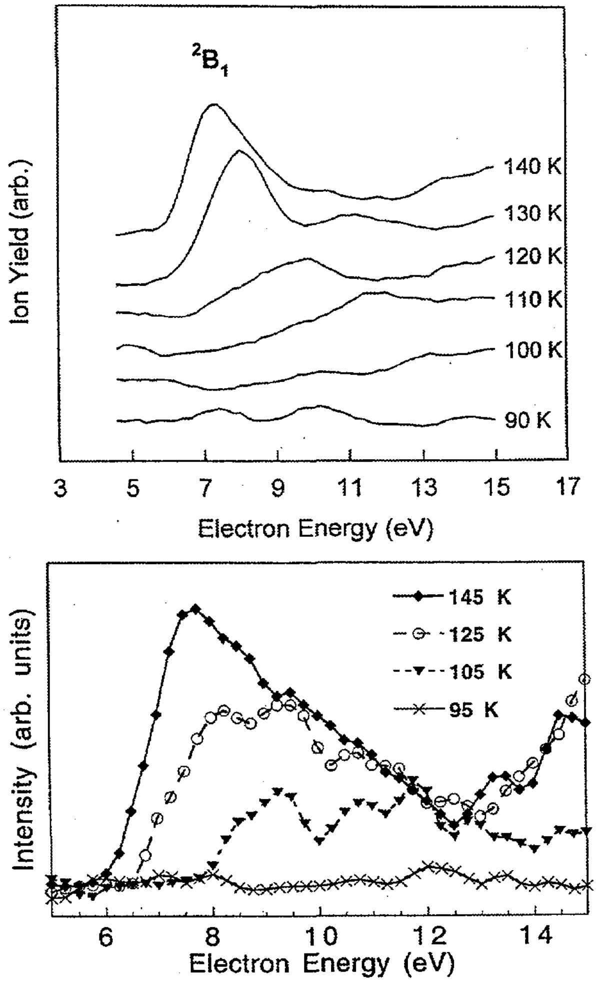

Figure 3.18. Temperature dependence of the D$^-$ yield (above) and D$_2$ ($v = 1$, $J = 2$) yield (below) vs. incident electron energy from a 60-bilayer film of amorphous ice. The film was initially grown at 90 K and the data were collected with the films held at the various temperatures indicated.

autodetachment.

References
1. M. T. Sieger and T. M. Orlando, "Low-Temperature Water Ice Phases Probed by Electron-Stimulated Desorption," *Surf. Sci.*, submitted.
2. M. T. Sieger and T. M. Orlando, "Effect of Surface Roughness on the Electron-Stimulated Desorption of D$^+$ from Microporous D$_2$O Ice," *Surf. Sci.* **390**, 92 (1997).
3. T. M. Orlando, G. A. Kimmel, and W. C. Simpson, "Quantum-Resolved Electron Stimulated Interface Reactions: D$_2$ Formation from D$_2$O Films," *Nucl. Instr. Meth. Phys. Res. B*, in press.

Vehicle Exhaust Treatment Using Electrical Discharge Methods

***R. G. Tonkyn, S. E. Barlow, T. M. Orlando, I. S. Yoon,* A. C. Kolwaite,* M. L. Balmer,* and J. Hoard*†**

Supported by a Cooperative Research and Development Agreement with the Low Emissions Technology Research and Development Partnership.

*EHSD Materials Group.
†Ford Motor Company.

Non-thermal dielectric barrier discharge systems are being examined for reduction of nitrogen oxides in diesel and lean burn vehicle exhaust. While theoretical and experimental work has shown that gas phase discharges can lower NO$_x$ and hydrocarbon concentrations in simulated vehicle exhaust, the energy efficiency and selectivity is low. Recent work has shown that energy efficiencies as well as yields and selectivities of the NO$_x$ reduction reaction can be enhanced by combining the discharge with select material surfaces.

Diesel and lean-burn exhausts contain a complex mixture of components that contribute to the overall chemistry that is promoted in the gas phase and on the surfaces of catalysts. The interactions between hydrocarbons, NO$_x$, water, oxygen, and hydroxyl radicals created in the plasma can potentially lead to a number of unwanted reaction by-products such as NO$_2$, N$_2$O, HONO, HNO$_3$, CH$_2$O, and organo-nitrates. Direct detection of N$_2$ from the reduction of NO$_x$ has not been demonstrated, due to high concentrations of N$_2$ in the exhaust streams and relatively minute starting concentrations of NO (50–500 ppm). Therefore, reported NO$_x$ reduction is derived from the amount of NO$_x$ that "disappears" and which is not transformed to other by-product species. Potentially large errors in the amount of NO$_x$ "reduced" can occur if the appropriate suite of analysis equipment is not used to measure all product gases, or if surface-adsorbed NO$_x$ is not measured. By replacing the nitrogen bath gas with helium, we have successfully demonstrated that "NO$_x$ removal" is indeed accompanied by N$_2$ production.

For these experiments a two-stage reactor configuration was used (Fig. 3.19). Simulated exhaust gas is passed through a non-thermal discharge prior to interacting with a proprietary catalyst. The product gases were analyzed with a chemiluminescent NO$_x$ meter, a mass spectrometer, a gas chromatograph and an FTIR spectrometer.

Nitrogen concentrations were measured with a gas chromatograph equipped with a 5-Å molecular sieve column. The signal was calibrated using a mixture of pure nitrogen and helium, and was found to be quite linear. Standard additions were used during the experiment itself to check on the sensitivity, with good agreement. The FTIR was

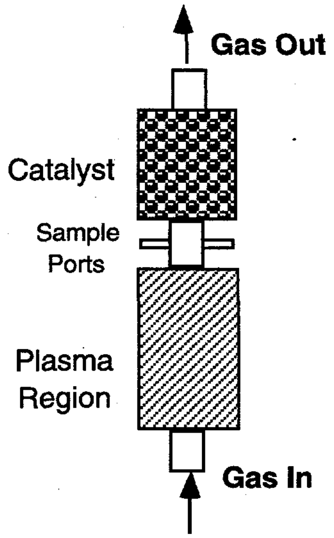

Figure 3.19. Two-stage reactor configuration where the catalyst is downstream from the plasma reactor.

utilized to measure N_2O production. The amount of missing NO_x was determined with the chemiluminescent NO_x meter.

Figure 3.20 shows the loss of NO_x versus the energy input into the plasma. These results, as well as the variation of the overall efficiency with respect to the oxygen and hydrocarbon concentrations, are consistent with our results utilizing a nitrogen bath gas. Sampling the exhaust between the discharge and the catalyst bed also suggests that similar discharge chemistry occurs with either He or N_2 as the bath gas.

As shown in Fig. 3.21, we found a direct correspondence between the loss of NO_x and the production of N_2 and N_2O. Comparison of the amount of N_2 produced as measured directly by the gas chromatograph with the amount of NO_x removed as measured by the chemiluminescent NO_x analyzer shows that only about 58% of the NO_x removed is reduced to nitrogen. FTIR analysis of product species suggests that a further 12% shows up as N_2O. No other nitrogen-containing species were observed that could account for the missing nitrogen. Experience suggests that at least some of the missing nitrogen is adsorbed to the surface. Clearly, further work is needed to determine if the discrepancy between NO_x reduction and the N_2 and N_2O production is due to undetected nitrogen-containing by-product species, surface storage, or inherent experimental differences that arise from replacing N_2 with He in the lean mix. This work also underscores the presence of competing reaction pathways for NO_x loss. Measurement of the N_2O to N_2 ratio under various reaction conditions could well lead to a better understanding of the underlying chemistry.

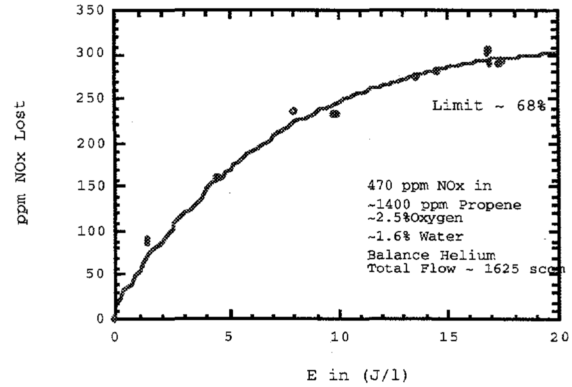

Figure 3.20. Loss of NO_x signal as a function of energy input.

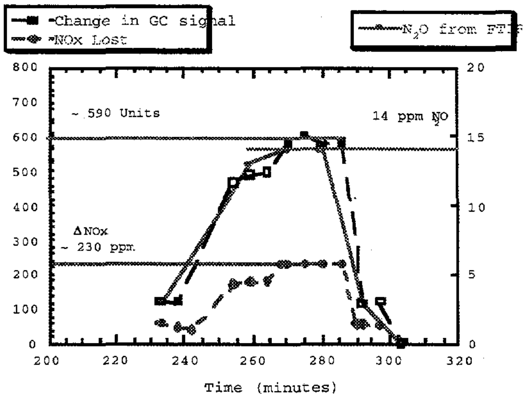

Figure 3.21. Loss of NO_x with concurrent production of N_2 and N_2O.

Production of Molecular Oxygen on Icy Satellites via Electronic Excitation

T. M. Orlando, M. T. Sieger, and W. C. Simpson**

Supported by DOE Office of Basic Energy Sciences.

*Postdoctoral Research Associate.

The signature of condensed O_2 has been reported in optical reflectance measurements of the Jovian moon Ganymede,[1] and an oxygen atmosphere has been observed surrounding Europa.[2] The surfaces of these moons contain large amounts of water ice, and it is thought that O_2 is formed by sputtering of ice by energetic particles from the Jovian magnetosphere.[3] Knowledge of how O_2 is made is crucial for accurate theoretical and experimental simulations of the surfaces and atmospheres of icy solar system bodies, but the detailed mechanism is poorly understood.

The reported heavy-ion and proton bombardment flux at Ganymede is between 10^8 and 10^{11} particles per cm^2 per s; the vacuum ultraviolet photon and electron fluxes are expected to be similar.[4] Previous studies have concluded that the sputtering of water ice plays an important role in the evolution of the surfaces of the icy moons and the plasma composition of the Jovian magnetosphere.[5]

As part of a continuing program studying the behavior of water ice under electron and photon bombardment, we have measured the electron energy threshold and temperature dependence of O_2 production during low-energy (5–100 eV) electron bombardment of thin (~40 bilayer) amorphous D_2O ice films in vacuum. The goal of this study was to understand the atomic mechanism for O_2 production in irradiated ice. Electron bombardment was chosen over high-energy ions as an excitation source, since the low excitation density, absence of knock-on processes, and negligible local heating allows examination of the purely electronic processes involved in O_2 formation.

The experiments were performed in an ultra-high vacuum system (base pressure $\sim10^{-10}$ Torr) equipped with a pulsed low-energy (5–100 eV) electron gun and a quadrupole mass spectrometer (QMS). The electron beam supplies a time-averaged electron flux of about 6×10^{13} $cm^{-2}s^{-1}$. The low incident current precludes any beam-induced heating and gas-phase interactions. The amorphous ice samples were prepared by vapor-depositing thin (~40 bilayer = 150 Å) films of D_2O on a clean Pt(111) substrate at 110 K, at a rate of 4–8 monolayers/min. D_2O was used to help distinguish D_2O and D_2 from background gases in other experiments. Other than an isotope shift in the temperature scale, it is believed that D_2O and H_2O behave identically. Molecular oxygen products were detected with the QMS in a "beam on / beam off" mode, which allowed for subtraction of the background signal. Other details of the apparatus, sample preparation, and data acquisition procedures have been published elsewhere.[6]

The electron energy threshold for O_2 formation was measured to be approximately 10 ± 2 eV (Fig 3.22), corresponding to valence electronic excitation or ionization of water molecules. Oxygen is not produced immediately upon electron exposure; the yield is initially zero, rises rapidly with increasing fluence, and asymptotically reaches a steady-state value, implying a two-step production mechanism. Comparison of the fluence dependence with kinetic models shows that O_2 is formed by direct excitation and dissociation of a stable precursor molecule, possibly HO_2 or H_2O_2, and not by diffusion and chemical recombination of radicals.[7]

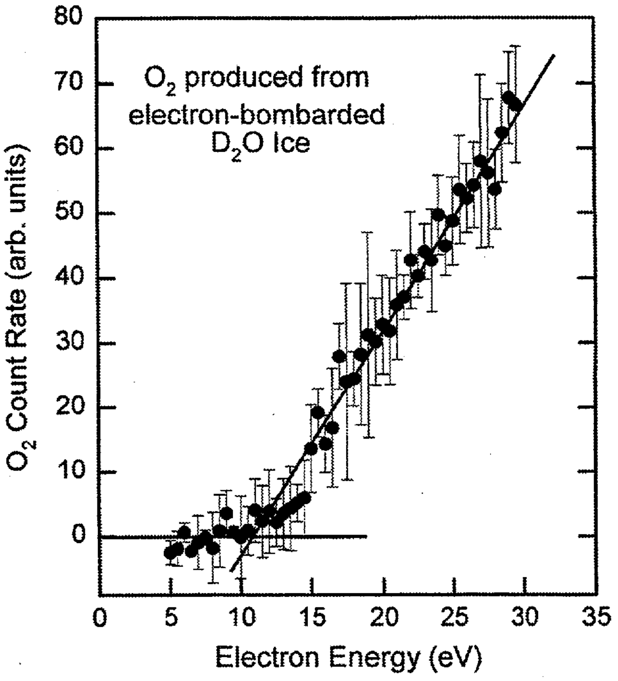

Figure 3.22. Yield of O_2 molecules produced from an amorphous D_2O ice film as a function of incident electron energy.

The O_2 yield is also strongly dependent on the temperature of the ice, showing structure indicative of bulk structural transitions. In Fig. 3.23 we plot the temperature dependence of the O_2 yields. The O_2 yield increases between 90–150 K, with a bump around 120 K. Measurements of D_2O ejected by electron bombardment suggest that the D_2O yield is constant or decreases in the same temperature region. The dip near 155 K is coincident with the amorphous-crystalline phase transition. The sublimation rate of ice is negligible below 140 K, but as the sample is heated above 160 K the film evaporates.

The data imply a complex dependence of O_2 production on temperature, and point to a novel explanation of thermal effects in ice sputtering, based on a temperature dependence of the dissociative excited state lifetimes of water. We propose that the temperature dependence of the O_2 yield is related to changes in the electronic excited states that lead to precursor formation. Since dissociation yields are very sensitive to the lifetime of the excited state, small perturbations in the lifetime can result in large changes in the dissociation cross section. There is evidence that the electronic excited state lifetimes are indeed temperature dependent; in studies of D^+ and D^- ejected from D_2O ice under electron bombardment,[6,8] we found that the ion desorption yields increase with sam-

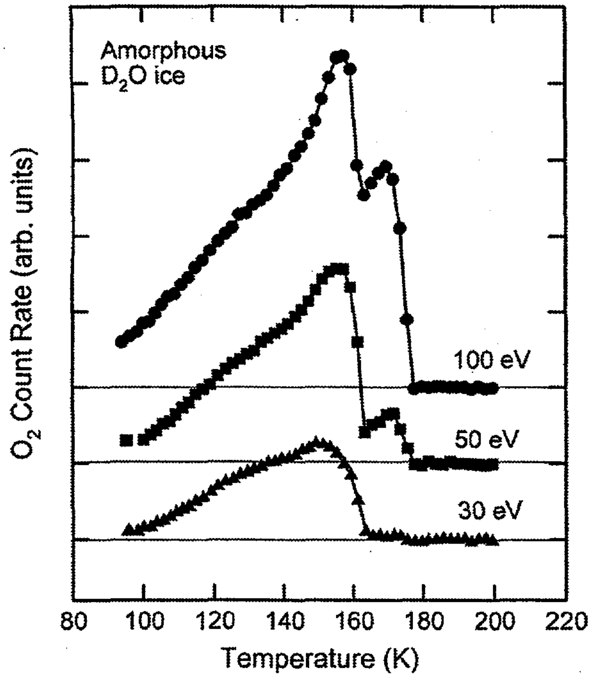

Figure 3.23. O_2 produced from amorphous D_2O ice under electron bombardment as a function of ice temperature for selected electron energies. The drop in yield at 160 K is coincident with the amorphous–crystalline phase transition. By 180 K the ice film has sublimed.

ple temperature in a manner suggestive of a weakening of the surface or near-surface hydrogen bonding network near 120 K. As water molecules become more weakly bound to their neighbors, they find it increasingly difficult to dispose of the excited state energy, and are more likely to dissociate. The monotonic rise of the O_2 yield below 150 K may therefore be related to changes in the near-surface structure of the ice itself. Our observations suggest that changes in the local electronic structure are more important than thermal diffusion for chemical processes in the electronic sputtering of ice.

The observed threshold energy (10 eV) is accessible to Lyman α photons (10.2 eV), suggesting that O_2 may be produced by direct solar illumination, and that low-energy electronic excitations are important in the formation of O_2 on Ganymede and Europa. The O_2 yield changes by nearly a factor of four over the day–night cycle temperature range of the Jovian moons (100–140 K). Since earlier work suggests that the temperature dependence is not related to thermal diffusion of reactive precursors in the ice,[6] we suggest that the strong temperature dependence is related to the lifetime of the dissociative electronic excited state of water that leads to O_2 precursor formation.

References

1. J. R. Spencer et al., *J. Geophys. Res.* **100**, 19049–19056 (1995).
2. D. T. Hall et al., *Nature* **373**, 677–679 (1995).
3. W. M. Calvin et al., *Geophys. Res. Lett.* **23**, 673–676 (1996).
4. W.-H. Ip et al., *Geophys. Res. Lett.* **24**, 2631–2634 (1997).
5. R. E. Johnson et al., *Science* **212**, 1027–1030 (1980).
6. M. T. Sieger et al., *Phys. Rev. B* **56**, 4925–4937 (1997).
7. M. T. Sieger et al., *Nature* **394**, 554—556 (1998).
8. W. C. Simpson et al., *J. Chem. Phys.* **107**, 8668–8678 (1997).

Low-Energy Electron Impact of Sodium Nitrate Crystals and Adsorbed Methanol Overlayers

N. G. Petrik, D. Camaioni,† and T. M. Orlando*

Supported by the DOE Environmental Management Science Program (EMSP)

*Visiting Scientist.
†EHSD Analytical Chemistry Group.

The radioactive and chemical wastes present in DOE underground storage tanks contain complex mixtures of sludges, salts, and supernatant liquids. These mixtures of a wide variety of oxide materials, aqueous solvents, and organic components, are constantly bombarded with energetic particles produced via the decay of radioactive ^{137}Cs and ^{90}Sr. Currently, there is a vital need to understand the radiolysis of organic and inorganic species present in mixed-waste tanks because these processes (1) produce mixtures of toxic, flammable, and potentially explosive gases (i.e., H_2, N_2O, and volatile organics); (2) degrade organics, possibly to gas-generating organic fragments; (3) reduce the hazards associated with nitrate-organic mixtures; and (4) alter the surface chemistry of insoluble colloids in tank sludge, influencing sedimentation and the gas/solid interactions that may lead to gas entrapment.

The aim of this work was to study electron-induced degradation of $NaNO_3$ crystals at low temperature and to probe radiation-induced processes at the $NaNO_3$/methanol interface.

1. Production of NO and O_2 from Low-Energy Electron Impact on Solution-Grown $NaNO_3$ Single Crystals at Low Temperature

$NaNO_3$ crystals were exposed to a continuous 100-eV electron beam and damage was analyzed for substrate temperatures between 100 and 450 K. Images of the sample were obtained by monitoring the incident current as a function of beam position. These images indicated that the beam was well focused over the temperature region studied, implying that charging did not limit the incident electron flux. NO and O_2, the two primary molecular products produced during electron-beam irradiation of $NaNO_3$, were detected via quadrupole mass-spectrometry.

The formation of NO and O_2 is consistent with previous work using pulsed electron and photon irradiation of $NaNO_3$ single crystals.[1-3] NO_2 was not detected with the continuous irradiation mode, in contradiction to the pulsed-mode experiments.

The temperature dependence of the NO and O_2 steady state ESD rates is shown in Fig. 3.24 and can be approximated by the sum of two exponents. These exponents correspond to activation energies of 0.24 and 0.016 eV for NO and 0.5 and 0.0035 eV for O_2 desorption. Note that a significant fraction of the O_2 molecules remain trapped in the crystal matrix, in accordance to a well known scheme of $NaNO_3$ bulk radiolysis/ photolysis:

$$NO_3^- \rightarrow NO_2^- + O,$$
$$O + NO_3^- \rightarrow NO_2^- + O_2,$$
$$O + O \rightarrow O_2.$$

Molecular oxygen is then released from the crystal during temperature-programmed annealing (Fig. 3.25). The TPD curve indicates at least two distinct mechanisms for O_2 production and desorption. The sharp low-temperature TPD peak corresponds to the temperature region in which $NaNO_3$ radiation defects recombine. The broad exponentially rising high-temperature peak is consistent with diffusion of subsurface O_2 followed by desorption. The temperature dependence of the O_2 yields indicate that significant amounts of O_2 can be produced at tank waste chemistry temperatures, and thus solid-state radiolysis contributes to tank waste aging.

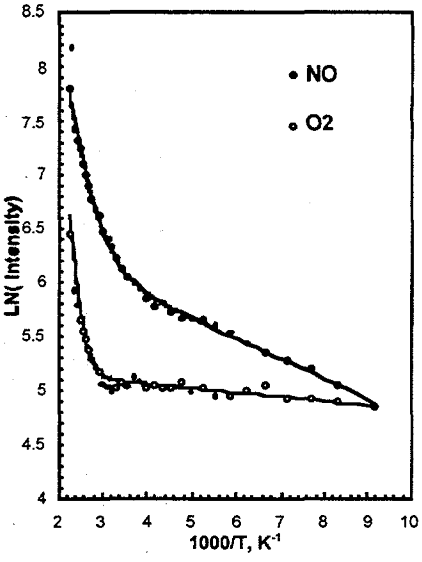

Figure 3.24. Arrhenius plot of NO and O_2 steady-state ESD rates from $NaNO_3$ surfaces under 100-eV continuous electron bombardment. The lines are a two-exponential approximation.

2. Low-Energy Electron Impact on a $NaNO_3$/Methanol Interface

Irradiation of complex tank wastes should generate new products as result of reactions of organic radicals and molecules at the organic/$NaNO_3$ interface. The importance of these interfacial reaction pathways was investigated by controlled electron-beam induced radiolysis of $NaNO_3$ surfaces containing multilayers of CH_3OH.

Multilayers (1–10 monolayers, ML) of CH_3OH

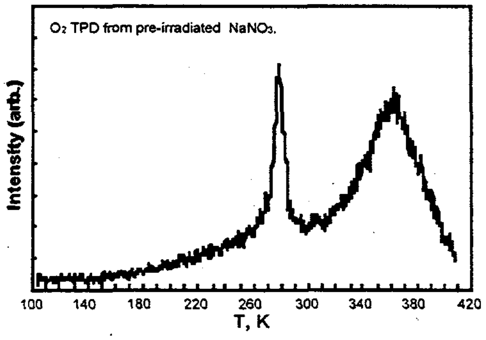

Figure 3.25. Thermal desorption of O_2 from $NaNO_3$ pre-irradiated with a 100-eV electron beam.

were adsorbed on the $NaNO_3$ surface at substrate temperatures between 114 and 120K. Irradiation of this interface with 100-eV electrons produced primarily NO and O_2 from the $NaNO_3$ surface, and H_2, CO, CH_4, CO_2, and CH_2O (formaldehyde) from the methanol overlayer. The NO and O_2 yields from $NaNO_3$ did not depend on the CH_3OH coverage up to 7 ML. This may indicate that the O_2 arises mainly from subsurface processes or non-uniform coverage. Post-irradiation TPD experiments revealed the formation of lower-volatility products such as water, dimethyl ether (CH_3OCH_3), ethanol (C_2H_5OH), ethylene glycol ($(CH_2OH)_2$), and methoxymethanol (CH_3O-CH_2OH). All of these products have been observed in a previous experiment on low-energy electron irradiation of methanol overlayers on a metal surface.[4] No significant amounts of R–NO compounds were produced under the 100-eV irradiation conditions. These results demonstrate that O and NO radicals produced at the $NaNO_3$ surface, do not react significantly with methanol under these thin-film experimental conditions. We expect the major reactions to occur in deeper layers of the organic liquid phase.[5]

References
1. K. Knutsen and T. M. Orlando, *Appl. Surf. Sci.* **127–129**, 1 (1998).
2. K. Knutsen and T. M. Orlando, *Phys. Rev. B.* **55**, 13246 (1997).
3. K. Knutsen and T. M. Orlando, *Surf. Sci.* **348**, 143 (1996).
4. T. D. Harris, D. H. Lee, M. Q. Blumberg, and C. R. Arumainayagam, *J. Phys. Chem.* **99**, 9530 (1995).
5. D. M. Camaioni, W. D. Samuels, J. C. Linehan, A. K. Sharma, M. O. Hogan, M. A. Lilga, S. A. Clauss, K. L. Wahl, and J. A. Campbell, *Organic Tanks Safety Program FY97 Waste Aging Studies*, PNL-11670, Rev. 1 (1998), Pacific Northwest National Laboratory, Richland, Washington.

Stimulated Luminescence of Yttria-Stabilized Cubic Zirconia Crystals

N. G. Petrik,* D. P. Taylor,† and T. M. Orlando

Supported by the DOE Environmental Management Science Program (EMSP).

*Visiting Scientist.
†Postdoctoral Research Associate.

The kinetics of laser-stimulated luminescence (LSL) of yttria-stabilized cubic zirconia (YSZ) single crystals was investigated.[1] Excitation of $ZrO_2 \cdot 9.5\% Y_2O_3$ (100) and (110) using ns pulses of 213-nm (5.82 eV), 266-nm (4.66 eV), and 355-nm (3.49 eV) photons produce LSL bands with Gaussian profiles and peak maxima at 460 nm (2.69 eV), 550 nm (2.25 eV) and 600 nm (2.07 eV), respectively. LSL involves a single-photon process for energy densities below ~1.0 MW/cm^2.

Decay times vary from 0.1 to 100 μs, depending on the excitation energy and temperature. Decay kinetics are hyperbolic, indicating that all LSL bands result from recombination.

The LSL quenches with increasing temperature, and the activation energies obtained using the Mott approximation are 0.10 ± 0.01, 0.20 ± 0.02, and 0.45 ± 0.04 eV for the 2.69-, 2.25-, and 2.07-eV LSL bands, respectively (see Fig. 3.26). The various activation energies, decay kinetics, and excitation/emission energies correspond to the presence of several emission centers which can be associated with anion vacancies. We tentatively

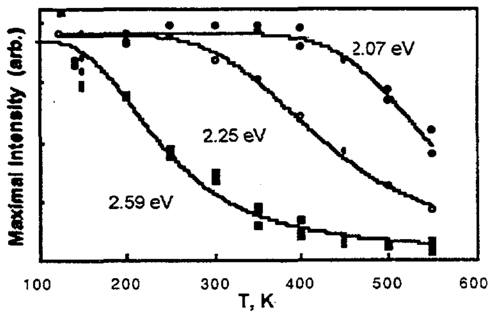

Figure 3.26. Temperature dependence of the luminescence peak intensities (points). The fit to the data (lines) is obtained using the Mott approximation, $I_{max} = I_{max}^0/[1 + A\exp(-Q/kT)]$.

assign these centers to intrinsic F-centers and extrinsic F-type centers (see Fig. 3.27). The latter are associated with one and two Y^{3+} ions in the nearest neighborhood positions. Since the normalized temperature dependencies of the decay coefficients are similar for all the LSL bands, we suggest that recombination primarily involves electrons, trapped at intrinsic and extrinsic defect sites, and mobilized holes.

References

1. N. G. Petrik, D. P. Taylor, and T. M. Orlando, *J. Appl. Phys.*, in press.
2. P. Li, I.-W. Chen, and J. E. Penner-Hahn, *Phys. Rev. B* **48**, 10074 (1993).
3. V. R. PaiVerneker, A. N. Petelin, F. J. Crowne, and D. C. Nagle, *Phys. Rev. B* **40**, 8555 (1989).
4. S. Choi and T. Takeuchi, *Phys. Rev. Lett.* **50**, 1474 (1983).

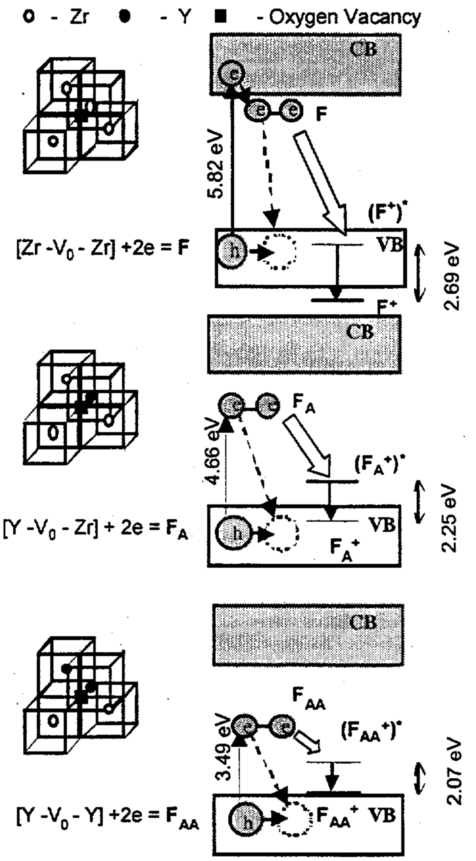

Figure 3.27. Simplified schemes of some important anion vacancies in the yttria-stabilized zirconia.[2] The F-centers associated with the vacancies and main electronic transitions leading to different types of luminescence are also indicated. *Note:* We have estimated the position of the F-type centers assuming the F+ level lies below the bottom of the O(2p) valence band.[3,4]

4. Cluster Models of the Condensed Phase

Cluster Model Studies of the Structure and Bonding of Environmentally-Important Materials

L. S. Wang, J. B. Nicholas,[*]
S. D. Colson, H. Wu,[†]
X. B. Wang,[†§] C. F. Ding,[§] and X. Li[†]

Supported by DOE Office of Basic Energy Sciences.

[*] EMSL Theory, Modeling, and Simulation.
[†] Washington State University.
[§] Postdoctoral Research Fellow.

Oxides of Si, Al, Mg, and Ti are major components of the earth and are important environmental materials. Their surface chemistries influence the storage and underground transport of waste materials. A major effort is being directed here to understand their surface and interface properties. We are engaged in a program to study the structure and bonding of these materials with cluster models, combining experimental and theoretical studies using anion photoelectron spectroscopy (PES) and quantum calculations. The smaller, controlled sizes of these cluster systems provide atomic-level models to enable us to better understand bulk surfaces and defect sites, and they are an excellent testing ground to benchmark theories intended for large and "real-world" systems.

A state-of-the-art magnetic-bottle time-of-flight PES spectrometer with a laser vaporization cluster source has been built for these studies. With high mass- and high electron-energy-resolution, this is a powerful apparatus for the study of clusters. In 1998, we have continued our investigations of aluminum oxide clusters. Photoelectron spectra of a series of $Al_3O_y^-$ clusters (y = 0–5) were measured at several photon energies: 532, 355, 266, and 193 nm (Fig. 4.1).[1] The electron affinities and low-lying electronic states of the Al_3O_y clusters were obtained. The photoelectron spectra clearly reveal a sequential oxidation behavior and the evolution of the electronic structure of the clusters from that of a metal cluster at Al_3 to that of a complete oxide cluster at Al_3O_5: two valence electrons of Al_3 are observed to be transferred to each additional O

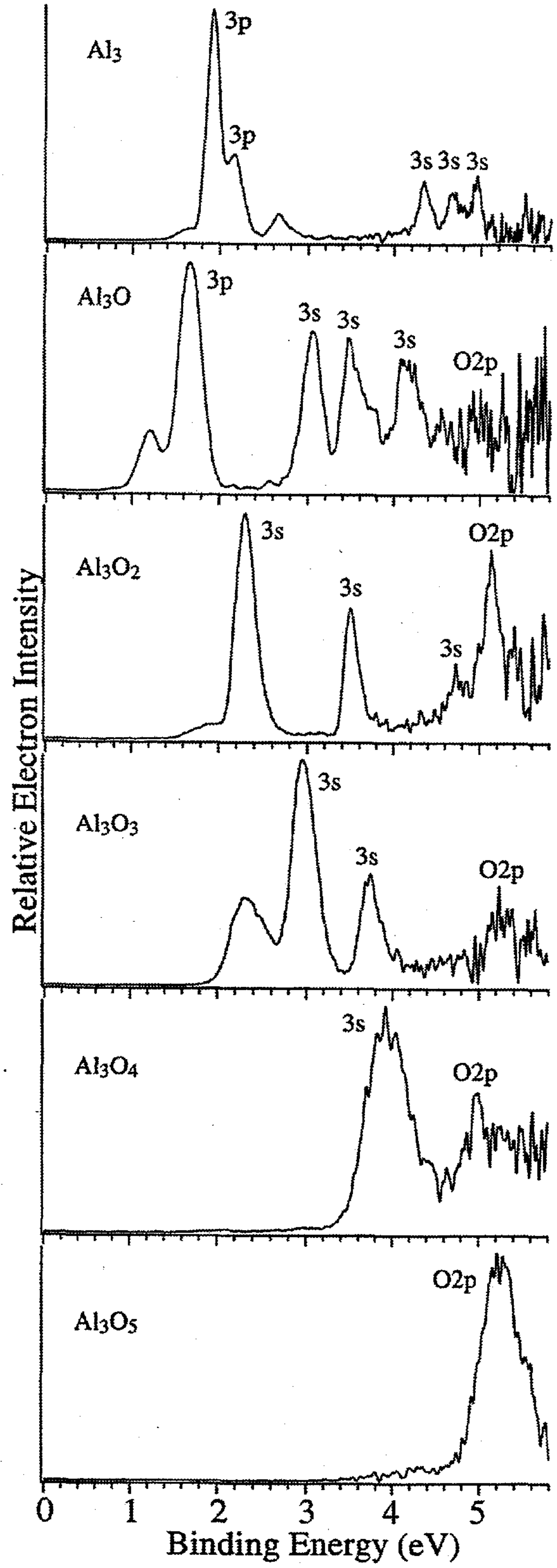

Figure 4.1. Photoelectron spectra of $Al_3O_y^-$ at 193 nm. The main characters of the features are labeled. The unlabeled features are due to anion excited states (Al_3^-) and isomers ($Al_3O_y^-$, y = 1–3).

atom until Al_3O_5, where all the nine valence electrons of Al_3 are transferred to the five O atoms. The anion $Al_3O_5^-$, which can be viewed as $(Al^{3+})_3(O^{2-})_5$, is found to be a closed-shell cluster, yielding an extremely high electron affinity for Al_3O_5 (4.92 eV). The electron affinities of the remaining clusters are: 1.90 (Al_3), 1.57 eV (Al_3O), 2.18 eV (Al_3O_2), 2.80 eV (Al_3O_3), and 3.58 eV (Al_3O_4). An electronic excited state of Al_3^- is also observed at 0.40 eV above the Al_3^- ground state. Isomers are observed for all the oxide clusters with lower electron affinities. Particularly, vibrational structures are observed for the two isomers of $Al_3O_3^-$, as well as a photoisomerization process between the two isomers. Information about the structure and bonding of the oxide clusters are obtained, based on the experimental data and the known structures for Al_3 and Al_3O.

Reference

1. H. Wu, X. Li, X. B. Wang, and L. S. Wang, *J. Chem. Phys.* **109**, 449 (1998).

Photodetachment Photoelectron Spectroscopy of Multiply Charged Anions

L. S. Wang, X. B. Wang,*† and C. F. Ding,†

Supported by DOE Office of Basic Energy Sciences.
*Washington State University.
†Postdoctoral Research Fellow.

Multiply charged anions are ubiquitous in nature, are often found in solutions and solids, and they play important roles in chemistry, biochemistry, and environmental and materials sciences. However, very few multiply charged anions are known or studied in the gas phase. This is partly due to the fact that many multiply charged anions are unstable in the gas phase, whereas they are stabilized in the condensed phase through solvation and electrostatic interaction with counterions. In the gas phase, these stabilizing factors are absent, and the large Coulomb repulsion between two or more excess negative charges makes multiply charged anions very fragile to electron loss or fragmentation. Thus the formation and characterization of such anions have been challenging both experimentally and theoretically.

During the past two years, we have developed a new one-of-its-kind apparatus, coupling photodetachment photoelectron spectroscopy and electrospray ionization to investigate the physical and chemical properties of free multiply charged anions in the gas phase. Electrospray ionization is one of the most useful techniques in biomedical mass spectrometry, and is ideal for producing naked or solvated multiply charged anions in the gas phase. The photodetachment studies allow us to obtain the intrinsic properties of the anions, and provide molecular-level information about their solvation and stabilization. Over the past year, we have completed the design and construction of this new apparatus (Fig. 4.2)[1] and obtained photodetachment spectra of doubly charged anions for the first time.

1. *Photodetachment Spectroscopy of A Doubly Charged Anion: Direct Observation of the Repulsive Coulomb Barrier*[2]

Our first experiment concerned with the citrate dianion (Fig. 4.3). The spectra of this dianion for the first time revealed directly the repulsive Coulomb barrier that binds electrons in multiply charged anions (Fig.4.4). This potential barrier, analogous to that in the alpha-decay of heavy nuclei, is important for understanding the properties of these anions. The repulsive Coulomb barrier height was estimated to be about 1.9~2.5 eV. The adiabatic electron binding energy was measured to be 1.0 eV. Two detachment channels were observed, with the second channel at ~0.6 eV higher in binding energy.

2. *Probing the Potential Barriers and Intramolecular Electrostatic Interactions in Free Doubly Charged Anions*[3]

We performed a series of experiments on dicarboxylate dianions (Fig. 4.5), $^-O_2C(CH_2)_nCO_2^-$ (n = 3–10), in which the distance between the two excess charges in the dianions can be systematically varied. In these experiments, we determined the precise relationship between the Coulomb repulsion and the Coulomb barrier in multiply charged anions. We found that the electron binding energies increase with the chain length, whereas the Coulomb barrier decreases with the

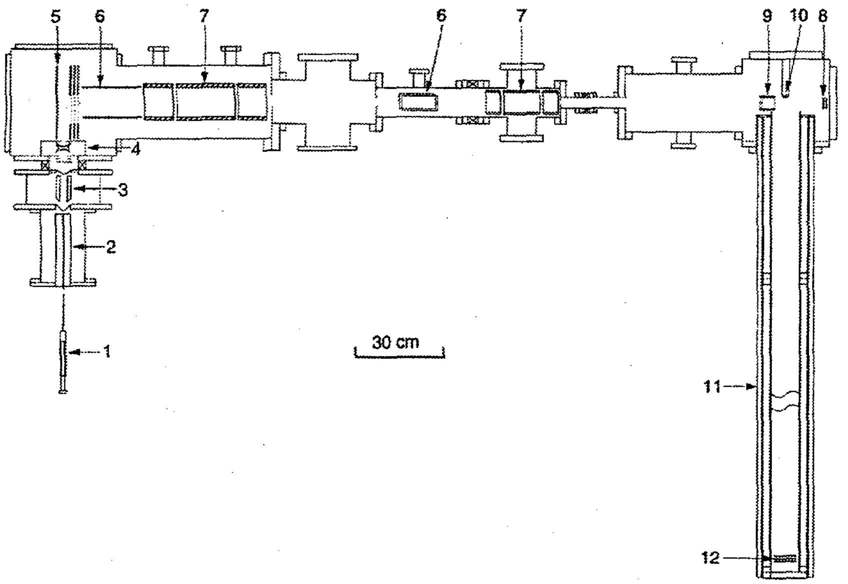

Figure 4.2. Schematic of the electrospray–magnetic-bottle photoelectron apparatus. 1. syringe; 2. desolvation capillary; 3. radiofrequency quadrupole ion guide; 4. 3-D ion trap; 5. ion repeller; 6. ion beam deflector; 7. einzel lens; 8. in-line mass detector; 9. mass gate and momentum deceleration assembly; 10. permanent magnet; 11. 4-m electron flight tube; 12. electron detector.

chain length, both following Coulomb's law (Fig. 4.6). Therefore the electron binding energy plus the Coulomb barrier, the effective potential well binding the electrons, is a constant, equivalent to the binding energy of an electron by a single carboxyl group.

3. Intramolecular Coulomb Repulsion and Solvent Stabilization[4]

Preliminary results on the solvation and stabilization of multiply charged anions have also been obtained. We studied a series of linear dicarboxylate dianions (DC^{2-}), $^{-}O_2C(CH_2)_nCO_2^{-}$ (n = 3–6), solvated by one and two waters. The electron binding energy of DC^{2-} decreases with decreasing aliphatic chain length, due to the increasing Coulomb repulsion between the two charges; the dianion with n = 2 has a binding energy close to zero and is not stable in the gas phase. We found that this dianion can be stabilized by one water, and in general the first water stabilizes the electron binding energy of DC^{2-} by ~0.3 eV. The second water, however, was observed to show a much stronger stabilization effect (~0.6 eV), suggesting that the two waters solvate the two carboxylate groups separately.

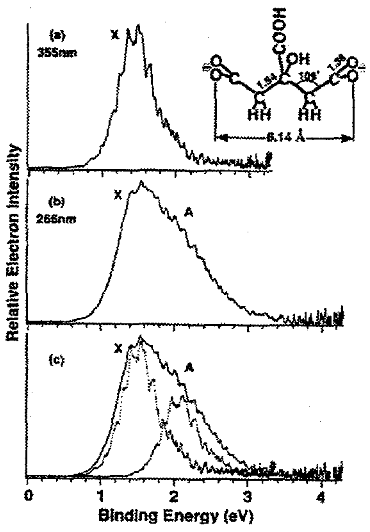

Figure 4.3. Photoelectron spectra of citrate acid dianion, CA^{2-}, at (a) 355 nm (3.49 eV) and (b) 266 nm (4.66 eV). Note the increased spectral width in the 266-nm spectrum, implying an additional detachment channel as shown in (c) (the dotted curves are two copies of the 355-nm spectrum with one shifted to higher binding energies).

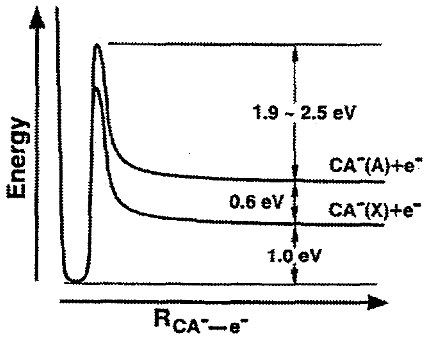

Figure 4.4. Schematic potential energy curves showing the adiabatic binding energies and the repulsive Coulomb barrier for detachment of CA^{2-}, leading to the X and A states of CA^{-}. Note that the barrier heights relative to the X and A states are assumed to be the same.

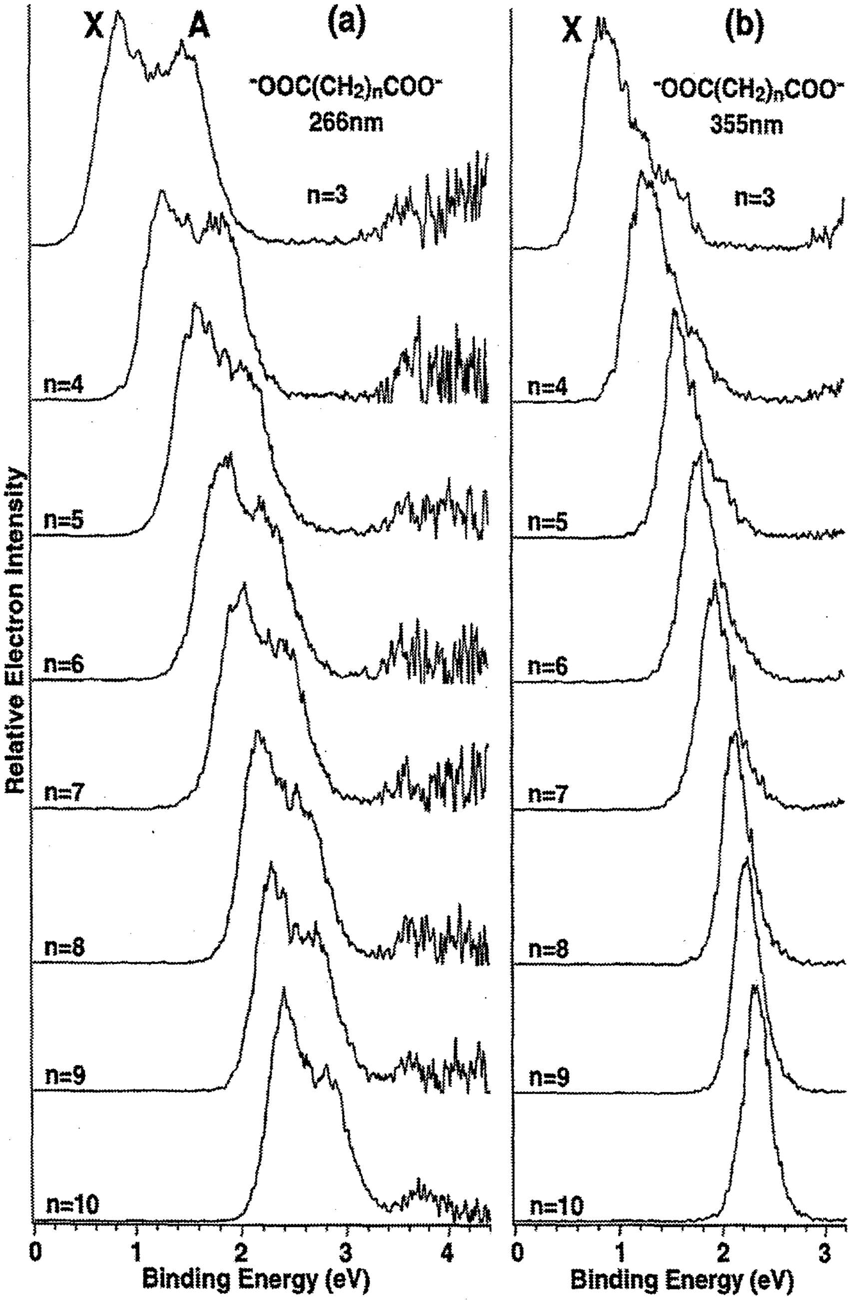

Figure 4.5. Photoelectron spectra of $^{-}O_2C(CH_2)_nCO_2^{-}$ (DC^{2-}) dianions ($n = 3$–10) at: (a) 266 nm (4.66 eV); (b) 355 nm (3.49 eV). Note the increase of binding energy with n and the disappearance of the higher energy feature at 355 nm due to the Coulomb barrier.

References

1. L. S. Wang, C. F. Ding, X. B. Wang, and S. E. Barlow, *Rev. Sci. Instrum.* **70**, xxx (1999).
2. X. B. Wang, C. F. Ding, and L. S. Wang, *Phys. Rev. Lett.* **81**, 3351 (1998).
3. L. S. Wang, C. F. Ding, X. B. Wang, and J. B. Nicholas, *Phys. Rev. Lett.* **81**, 2667 (1998).
4. C. F. Ding, X. B. Wang, and L. S. Wang, *J. Phys. Chem. A* **102**, 8633 (1998).

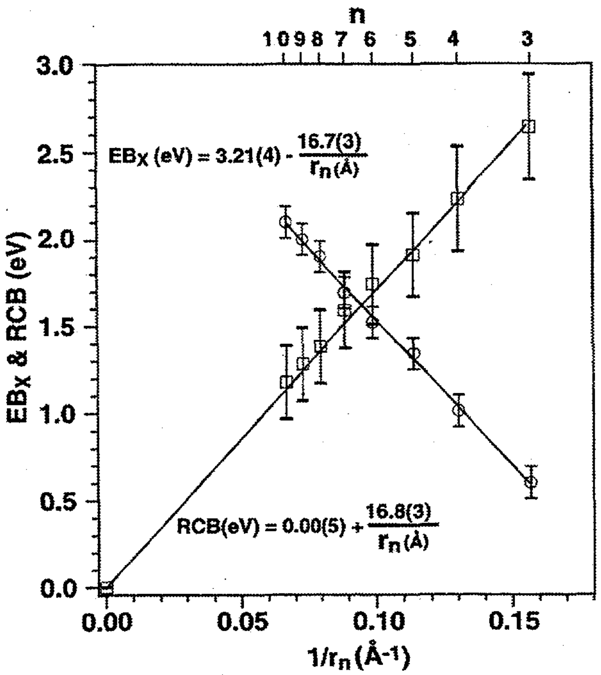

Figure 4.6. The measured adiabatic electron binding energies (EB$_x$) and the estimated repulsive Coulomb barrier heights (RCB) for DC^{2-} as a function of $1/r_n$, where r is the average equilibrium distance (Å) between the two charge centers in DC^{2-}, assumed to be localized on the O atoms of the carboxylate groups. Circles, EB$_x$; squares, RCB; lines are least-square fits. Note that the magnitudes of the slopes of the two lines are the same, *i.e.*, EB$_x$ + RCB = constant.

Photoelectron Spectroscopy and Electronic Structure of Metal Clusters and Chemisorbed Metal–Cluster Complexes

L. S. Wang, H. Wu, X. B. Wang,*†*
C. F. Ding,† X. Li, and W. Chen*†*
Supported by National Science Foundation.
*Washington State University.
†Postdoctoral Research Fellow.

One of the key issues in the study of metal clusters is understanding the electronic structures of these intermediate systems and their evolution toward bulk band structure as the cluster size increases. Our photoelectron spectroscopy experiments of size-selected cluster anions are ideal for providing this electronic information. The interactions between oxygen and metals are important in many areas of chemistry and materials sciences. Our laser vaporization cluster source and the high sensitivity of the magnetic-bottle PES apparatus provide a unique opportunity for us to investigate a broad range of metal oxide species that are otherwise impossible to study.

1. *Observation of s-p Hybridization and Electron Shell Structures in Aluminum Clusters*[1]

Using photoelectron spectroscopy of size-selected Al$_x^-$ (x = 1–162) clusters, we studied the electronic structure evolution of Al$_x$ and observed that the Al 3s- and 3p-derived bands evolve and broaden with cluster size, and begin to overlap at Al$_9$. Direct spectroscopic signatures were obtained for electron shell structures with spherical shell closings at Al$_{11}^-$, Al$_{13}^-$, Al$_{19}^-$, Al$_{23}^-$, Al$_{35}^-$, Al$_{37}^-$, Al$_{46}$, Al$_{52}$, Al$_{55}^-$, Al$_{56}$, Al$_{66}$, and Al$_{73}^-$ (Fig. 4.7). The electron shell effect diminishes above Al$_{75}$, and new spectral features appearing in Al$_x^-$ (x > 100) suggest a possible geometrical packing effect in large clusters.

2. *A Photoelectron Spectroscopic Study of Monovanadium Oxide Anions (VO$_x^-$, x = 1–4)*[2]

We studied monovanadium oxides, VO$_x^-$ (x = 1–4), at four photon energies: 532, 355, 266, and 193 nm. Vibrationally-resolved photoelectron spectra were obtained for VO$^-$ at 532 and 355 nm. Two new low-lying excited states were observed for VO at 5,630 and 14,920 cm^{-1} above the ground state. These states were assigned to two doublet states, $^2\Sigma^-$ and $^2\Phi$, respectively. The 532 and 355 nm spectra of VO$_2^-$ revealed a single vibrational progression for the ground state with a frequency of 970 cm^{-1} (ν_1). Three electronic excited states were observed for VO$_2$ in the 193-nm spectrum. For VO$_3^-$, three surprisingly sharp detachment transitions were observed at 193 nm. The two excited states of VO$_3$ were measured to be 0.59 and 0.79 eV above the ground state. The spectra of VO$_2^-$ and VO$_3^-$ were interpreted using the molecular orbital schemes obtained in a previous *ab initio* theoretical study,[3] which predicted that both

VO_2 and VO_3 neutrals were of C_{2v} symmetry with a doublet ground state. The spectrum of VO_4^- was obtained at 193 nm, showing features similar to that of VO_3^-, but much more broadened. The adiabatic electron affinities of VO, VO_2, VO_3, and VO_4 were measured to be 1.229(8), 2.03(1), 4.36(5), and 4.0(1) eV, respectively, with a significant increase from VO_2 to VO_3. The electronic and geometrical structures of the series of monovanadium oxide species were discussed based on the current observation and previous spectroscopic and theoretical results.

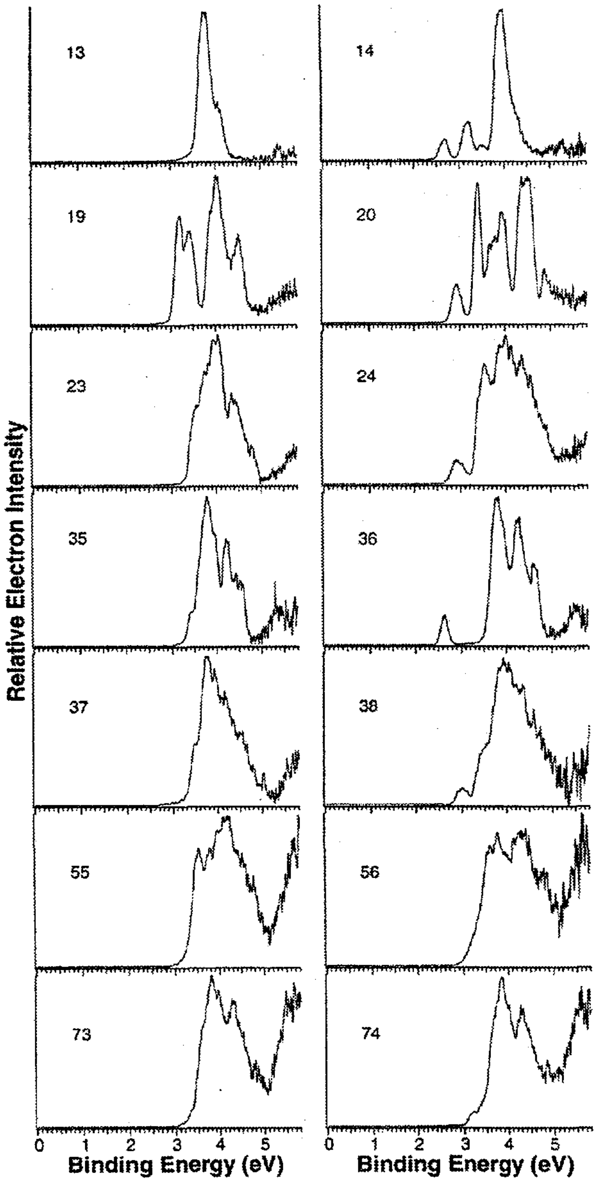

Figure 4.7. Photoelectron spectra (193 nm) of the expected closed shell Al_x^- anions (left column) compared to those of the Al_{x+1}^- clusters (right column). Note the high binding energies of the closed shell Al_x^- clusters and the appearance of low binding energy features and energy gaps in the Al_{x+1}^- clusters.

3. Photoelectron Spectroscopy and Electronic Structure of ScO_n^- (n = 1–4) and YO_n^- (n = 1–5): Strong Electron Correlation Effects in ScO^- and YO^-.[4]

A photoelectron spectroscopic study of ScO_n^- (n = 1–4) and YO_n^- (n = 1–5) was carried out at three photon energies: 532, 355 and 266 nm. Vibrationally resolved photoelectron spectra were obtained for ScO^- and YO^-. The electron affinities of both ScO and YO were measured to be identical (1.35 eV) within the experimental accuracy (±0.02 eV). Three low-lying excited states were observed for the monoxides, $A'^2\Delta$, $A^2\Pi$, and $B^2\Sigma^+$. The latter two excited states resulted from two-electron detachment, suggesting unusually strong electron correlation (configuration interaction) effects in the ground state of the anions. The excitation energies of the low-lying states were also found to be similar for the two monoxides, except that YO has a smaller vibrational frequency and larger spin-orbit splitting. The $A'^2\Delta$ states of both ScO and YO show very strong photon energy-dependent detachment cross sections. Four similar photoelectron features were observed for the dioxides, with those of YO_2^- having lower binding energies. A second isomer due to an O_2 complex was also observed for Sc and Y. Broad and featureless spectra were observed for the higher oxides. At least two isomers were present for the higher oxides, one with low and one with high binding energies.

References

1. X. Li, H. Wu, X. B. Wang, and L. S. Wang, *Phys. Rev. Lett.* **81,** 1909 (1998).
2. H. Wu and L. S. Wang, *J. Chem. Phys.* **108,** 5310 (1998).
3. L. B. Knight Jr., R. Babb, M. Ray, T. J. Banisaukas III, L. Russon, R. S. Dailey, and E. R. Davidson, *J. Chem. Phys.* **105,** 10237 (1996).
4. H. Wu and L. S. Wang, *J. Phys. Chem. A* **102,** 8633 (1998).

Study of Transition Metal–Carbon Mixed Clusters

L. S. Wang, X. B. Wang,[,†]*
H. Wu,[*] W. Chen,[,†] X. Li,[*]*
and H. S. Cheng[§]

[*]Washington State University.
[†]Postdoctoral Research Fellow.
[§]Air Products and Chemicals Inc.

Supported by National Science Foundation.

The objective of this research is to study the structure and formation of metal carbide clusters (M_xC_y) in the gas phase, and nanomaterials formed by these clusters in the condensed phase. The gas-phase study involves anion photoelectron spectroscopy, which yields electronic structure as well as vibrational information on the small M_xC_y clusters. We aim to provide a fundamental understanding of the structure and bonding of the M_xC_y clusters in a wide size range, and to understand the subtle differences in bonding and structures between carbon and the transition metals across the first transition series. The gas-phase studies will yield insight into the formation mechanisms of three classes of novel materials: endohedral metallo-fullerenes, single-shell carbon nanotubes, and metallo-carbohedrenes, because the formation of all depend on the interaction between carbon and the transition metals, and exhibits certain propensity among the transition metals. The microscopic understanding of the formation of these novel materials requires a thorough characterization of the small M_xC_y clusters and how their structure and bonding evolve as the cluster size increases. Such an understanding will lead to more efficient methods to synthesize these novel materials as well as to tailor-design new cluster materials involving carbon and transition metals.

1. New Magic Numbers in $Ti_xC_y^-$ Anion Clusters and Implications for the Growth Mechanisms of Titanium Carbide Clusters[1]

We reported observation of new prominent peaks in the $Ti_xC_y^-$ anion mass spectra from laser vaporization experiments involving a pure Ti target with a CH_4-seeded He carrier gas (Fig. 4.8). Both photoelectron spectroscopy and density functional calculations were performed to obtain structural and bonding information for the new prominent anion clusters, including $Ti_3C_8^-$, $Ti_4C_8^-$, $Ti_6C_{13}^-$, $Ti_7C_{13}^-$, $Ti_9C_{15}^-$, and $Ti_{13}C_{22}^-$. For each cluster, we optimized several structures, evaluated their electron affinities (EAs), and simulated their single particle density of states (DOS); cf. Fig. 4.9. The calculated EAs and DOS of the different structures were then compared with the experimental photoelectron data. Good agreement between the experiments and calculations was found for the lowest energy isomers considered in each case. We found that three factors, i.e., the C_2 dimer, cubic framework, and layered structures, play essential roles in determining the structures and chemical bonding of the titanium carbide clusters. A growth pathway from Ti_3C_8 to $Ti_{13}C_{22}$ with Ti_6C_{13}, Ti_7C_{13}, and Ti_9C_{15} as intermediates was proposed and discussed.

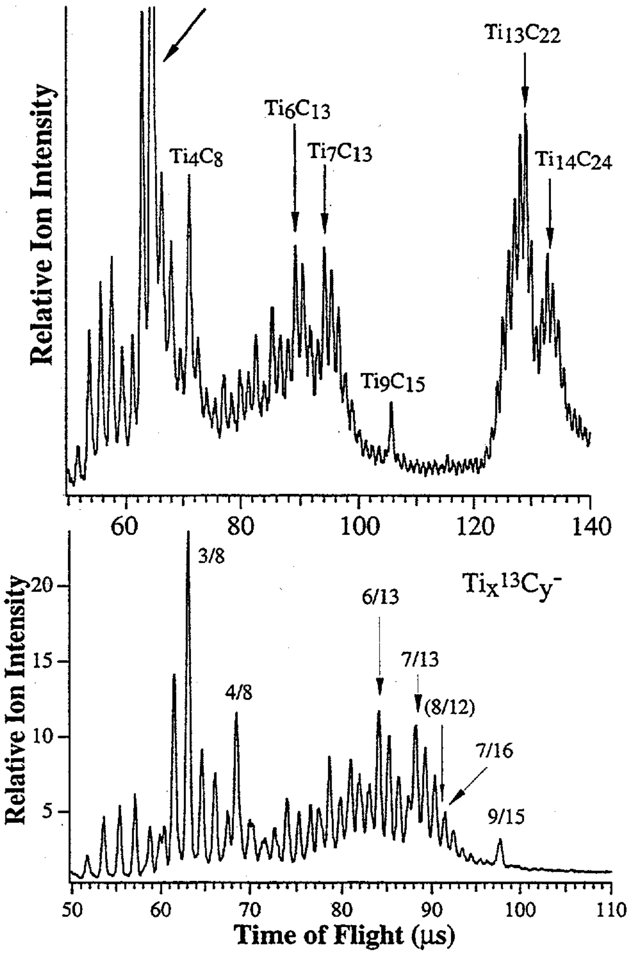

Figure 4.8. Mass spectra of $Ti_xC_y^-$ and anions from laser vaporization of a pure Ti target with a He carrier gas containing 5% CH_4. Note that the $Ti_3C_8^-$ peak (top panel) is out of scale and is twice the full scale.

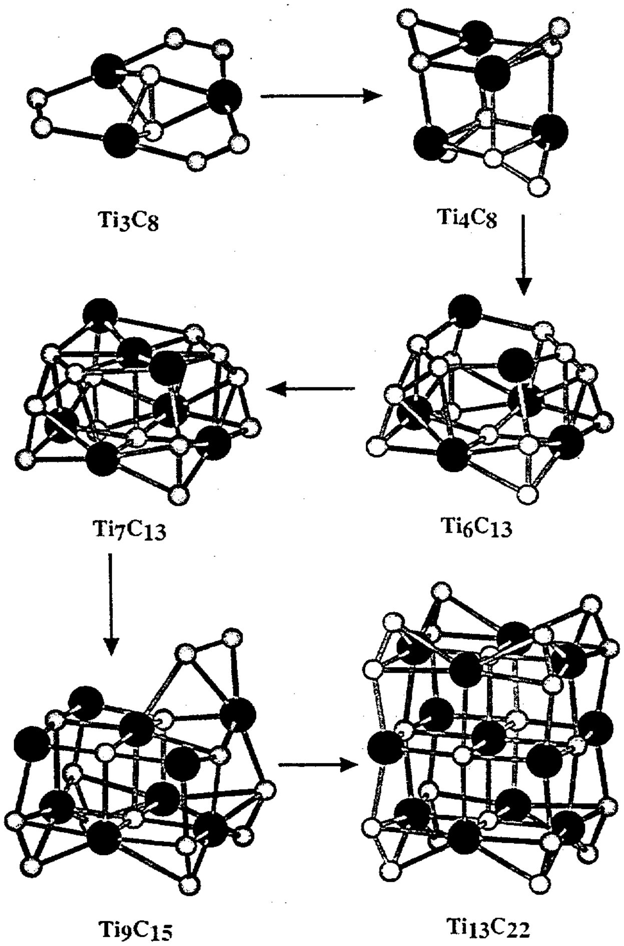

Figure 4.9. Optimized structures of the Ti_3C_8, Ti_4C_8, Ti_6C_{13}, Ti_7C_{13}, Ti_9C_{15}, and $Ti_{13}C_{22}$ clusters using density functional theory.

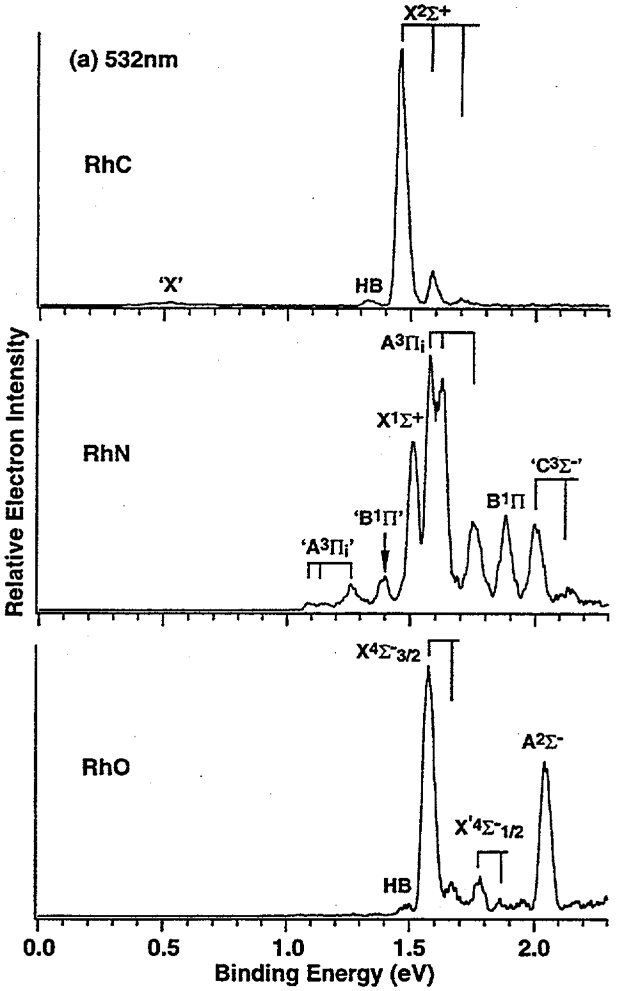

Figure 4.10. Photoelectron spectra of RhC^-, RhN^-, and RhO^- at 532 nm (2.33 eV). HB stands for hot-band transitions. Transitions due to excited states of the anions are labeled in single quotes. Vertical lines represent vibrational levels or spin-orbit components.

2. The Chemical Bonding and Electronic Structure of RhC, RhN, and RhO[2]

The electronic structure and chemical bonding of RhC, RhN, and RhO were experimentally investigated using anion photoelectron spectroscopy. Vibrationally resolved photoelectron spectra of RhC^-, RhN^-, and RhO^- were obtained at two detachment photon energies, 532 nm (2.33 eV) (Fig. 4.10) and 355 nm (3.49 eV). Electron affinities, low-lying electronic states, and vibrational frequencies were reported for the neutral diatomic molecules. The adiabatic electron affinities were similar for the three molecules and increase slightly from RhC to RhO (RhC: 1.46 eV; RhN: 1.51 eV; RhO: 1.58 eV). The low-lying electronic states were rather simple for RhC, with its first electronic excited state occurring at 9,400 cm^{-1} above the ground state, whereas those of RhN and RhO were more complicated, with numerous closely spaced low-lying electronic states. Excited states of the anions were also observed for RhC^- and RhN^-. The trend of the chemical bonding from RhC to RhO was discussed based on the experimental results.

References

1. L. S. Wang, X. B. Wang, H. Wu, and H. Cheng, *J. Am. Chem. Soc.* **120**, 6556 (1998).
2. X. Li and L. S. Wang, *J. Chem. Phys.* **109**, 5264 (1998).

Time-Resolved Spectroscopy of Solute/Solvent Clusters

D. M. Laman, A. G. Joly, and D. Ray*

Supported by DOE Office of Basic Energy Sciences.

*Postdoctoral Research Associate.

We are developing and applying time-domain spectroscopic techniques to measure the geometric structures of solute/solvent clusters, and determine suitable models for the intermolecular interactions operative in solvation in condensed phases. The methods under development are implementations of rotational coherence spectroscopy (RCS). RCS is a high-resolution, time-domain spectroscopic method for the determination of the moments of inertia of molecular species isolated in the gas-phase. It yields the rotational constants of an absorber to an accuracy of 0.1–1% without requiring precise measurement or detailed analysis of individual eigenstates. It has become an established technique, principally through the efforts of Felker and coworkers. In many cases, RCS is complementary to high-resolution spectroscopy in the frequency domain. It has great utility as a method providing gross structural data, and is a particularly useful technique for species that have prohibitively dense or featureless spectra in the frequency domain. In previous years, we have employed techniques that yielded rotational constants averaged over the ground and first electronically excited state for clusters containing chromophores that absorb visible and near-UV light readily. These techniques are adequate for clusters which absorb visible or near-UV radiation and do not undergo significant geometry changes upon electronic excitation, but inadequate for clusters that undergo photoinitiated dynamics or do not absorb light in the visible or near-UV region.

In the past year we have used a psec time-resolved method to measure rotational constants of the first excited state of fluorene-(H_2O) and fluorene-$(H_2O)_2$ (cooled to ~5 K in a continuous molecular beam) via laser-induced fluorescence. Assignment of the optical spectra of these species (both laser-induced fluorescence spectra and multiphoton ionization spectra) to clusters of specific composition is not possible due to spectral overlaps and fragmentation following photionization. Figure 4.11 shows the time-resolved fluorescence from fluorene–water clusters following photoexcitation at 33838 cm^{-1}. In addition to the exponential decay characteristic of a fluorescence lifetime of ~11 ns and a number of recurrences due to fluorene-(H_2O) spaced by ~$2/(B + C)$, smaller recurrences due to fluorene-$(H_2O)_2$ are also present. Analysis of these data will indicate whether the water is bound to one aromatic ring in fluorene or is shared between both aromatic rings. Analysis of a transient at 33833 cm^{-1} only exhibits recurrences due to fluorene-(H_2O), and suggests the presence of internal rotor levels of different nuclear spin symmetry (*ortho-* and *para*-H_2O) in fluorene-(H_2O) which do not interconvert in the rarified environment of a low-temperature molecular beam.

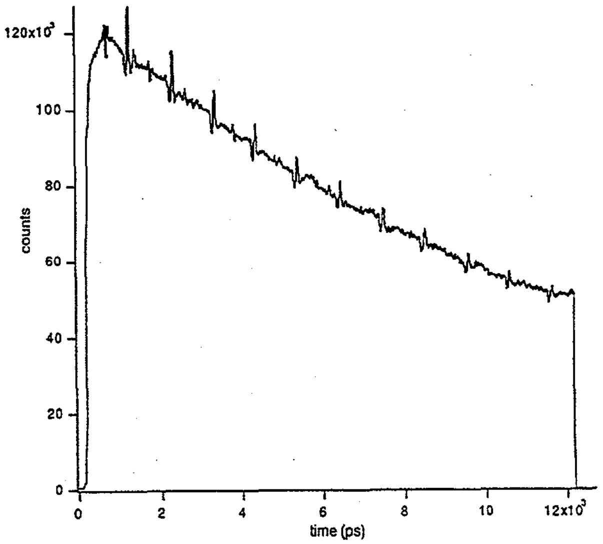

Figure 4.11. Rotational coherence spectrum of fluorene-$(H_2O)_1$ clusters following 33838-cm^{-1} excitation.

Figure 4.12 shows the time-resolved fluorescence from fluorene–water clusters following photoexcitation at 33827 cm^{-1} [resonant with the $S_0 \rightarrow S_1$ transition of fluorene-$(H_2O)_2$ but red-shifted from the $S_0 \rightarrow S_1$ origin of fluorene-(H_2O)]. The fluorescence decay can be fit with a single exponential with a ~9 ns decay constant, and the observed recurrences are consistent with a geometric structure in which both water molecules are on the same side of fluorene. Figure 4.13 shows the time-resolved fluorescence from fluorene–water clusters following photoexcitation at 33849.0 cm^{-1} [resonant with $S_0 \rightarrow S_1$ transitions in both fluorene-$(H_2O)_2$ and fluorene-(H_2O)]. The many recurrences in this transient occur at times consistent with the data in Figs. 4.11 and 4.12. The fluorescence decay can be fit with a single exponential

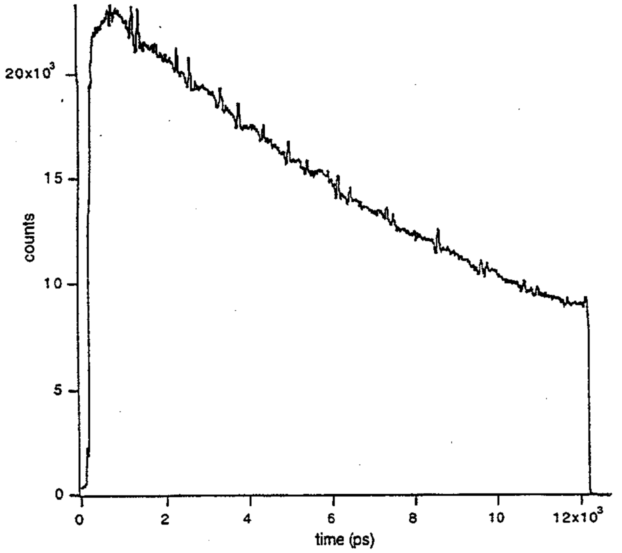

Figure 4.12. Rotational coherence spectrum of fluorene-$(H_2O)_2$ clusters following 33827-cm^{-1} excitation.

with a ~9.5 ns decay constant (it can also be fit to the sum of two exponentials with equal amplitudes and decay constants of 11 and 9 ns). These data indicate the utility of rotational coherence spectroscopy not only in determining rotational constants, but also in properly assigning vibronic spectra to clusters of specific composition.

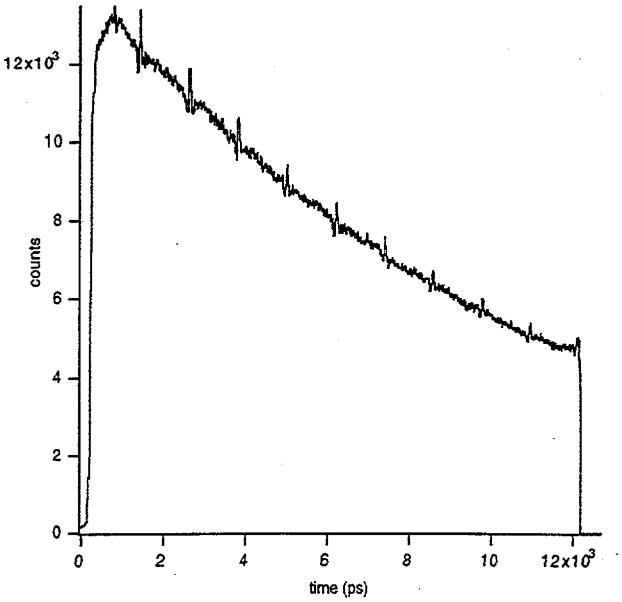

Figure 4.13. Rotational coherence spectrum of mixed fluorene-$(H_2O)_n$ clusters following 33849-cm^{-1} excitation.

5. Miscellaneous

High-Resolution Infrared Spectroscopy: Basic and Applied Research

S. W. Sharpe, T. A. Blake, and R. L. Sams

Supported by EMSL Operations
and U.S. Department of Energy.

Infrared spectroscopy is one of several powerful techniques that the physical chemist can call upon for studying the behavior of matter on an atomic scale. In addition, infrared spectroscopy forms the basis for a suite of analytical techniques that are highly specific and extremely sensitive, and can be directly applied to a number of monitoring problems. Brief descriptions of several ongoing projects in these areas are summarized below.

1. EMSL Molecular Beam–Fourier Transform Infrared Spectroscopy Capabilities

High-resolution gas-phase infrared spectroscopic techniques have traditionally been plagued by a number of problems including spectral congestion, Doppler broadening, and pressure broadening. Spectral congestion is related to the number of quantum states populated at a given temperature, and is dictated by Maxwell-Boltzmann statistics. Doppler broadening is related to temperature through the kinetic energy relationship, but also involves the random three-dimensional motion of the gas molecules. Pressure broadening is related to temperature through the collisional frequency of the molecules, which depends on the density and mean molecular velocity in the sample. By cooling and reducing the pressure of a gas in specially designed cells, these three effects can be minimized, but at the expense of drastically reduced signals.

In a typical experiment, a gas sample is expanded through a slit orifice measuring 12 cm in length by 50 μm wide. The ensuing *ribbon* of gas expands at supersonic velocities, and in the process molecules entrained in this ribbon are cooled to a few degrees above absolute zero. In addition, the random three-dimensional motion of the gas molecules is changed to a two-dimensional flow with little velocity component in the plane of expansion but perpendicular to the mass flow. If infrared light is used to interrogate the gas molecules through the plane of expansion, spectral congestion, Doppler broadening, and pressure broadening are reduced significantly.

In the past, we have made extensive use of tunable infrared lead-salt diode lasers to interrogate the expanding gas. While infrared lasers make ideal light sources in many respects (i.e., extremely high spectral brightness, low noise, narrow bandwidth and rapid tunability), they are severely limited by narrow spectral coverage. Often an experiment will be determined by what laser coverage is available. Recently, we have succeeded in interfacing a high-resolution Fourier-transform infrared spectrometer (FTIRS) with a continuous slit expansion source. This provides an alternative to laser sources and offers continuous spectral coverage from the near to far infrared (ca. 15,000 to 10 cm^{-1}). Although FTIR has been used to interrogate molecular beams in the past, those setups utilized a round expansion orifice at moderate spectral resolution. The PNNL FTIRS–beam machine is capable of recording high-resolution ($\Delta\nu \approx 0.0015$ cm^{-1}) spectra at rotational temperatures of 15 K anywhere in the near- to far-infrared spectral region. A schematic of this apparatus is shown in Fig. 5.1.

Figure 5.2 shows the first spectrum of a weakly bonded (van der Waals) system, Ar–N_2O, produced by the PNNL FTIRS–beam spectrometer. Despite the fact that this spectrum represents only two scans of the interferometer at ultimate resolution (0.0015 cm^{-1}), the signal-to-noise is not too poor. The Ar–N_2O dimer represents a true van der Waals complex, and is much harder to observe

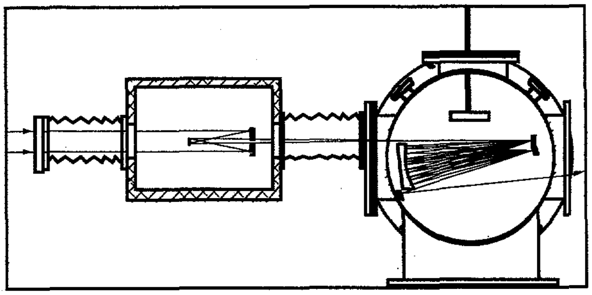

Figure 5.1. Layout of FTIR–beam machine. The box at left contains the beam-reducing optics. The supersonic molecular beam is generated at the top of the round chamber.

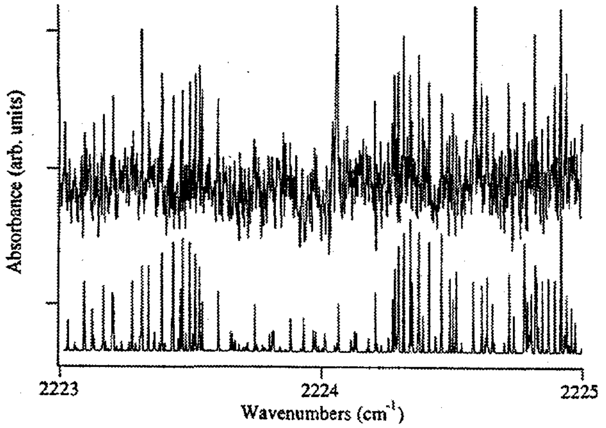

Figure 5.2. A portion of the N=N=O stretching region of the weakly-bonded Ar–N_2O dimer. The upper trace is the observed FTIR spectrum; the lower trace is an asymmetric rotor simulation. The intense absorption features are due to the N_2O monomer.

than previous hydrogen-bonded species examined via FTIR/beam studies. This unique instrument is currently being used to investigate classes of CFHCs or Freon substitutes, and can be made available for outside collaborations. In addition to the FTIR–beam spectrometer, a pulsed-beam lead-salt diode laser spectrometer is available for ultra-cold, high resolution studies.

2. *Hydrogen Fluoride Clusters*

We have recently studied hydrogen fluoride clusters, which are prototypical hydrogen-bonded species. The vapor phase of HF exhibits a number of unusual thermodynamic properties such as high heat capacity and high thermal conductivity; it has long been assumed that these properties are due to the formation of hydrogen-bonded oligomers. In fact, the gas-phase molecular weight has been measured at close to 60 amu.[1] Consequently, small clusters of HF have been of considerable theoretical interest, and recent theoretical results have predicted planar oblate symmetric-top structures for the trimer, tetramer, and pentamer[2] at the global minimum of their potential energy surfaces. The equilibrium structure (C_{4h} symmetry) of the tetramer is shown in Fig. 5.3. These clusters are strongly bonded: the tetramer, for example, has a dissociation energy D_0 of >7000 cm^{-1} with respect to fragmentation into separate monomers. As a result of this deep well, there are a number of intermolecular vibrational modes that should be

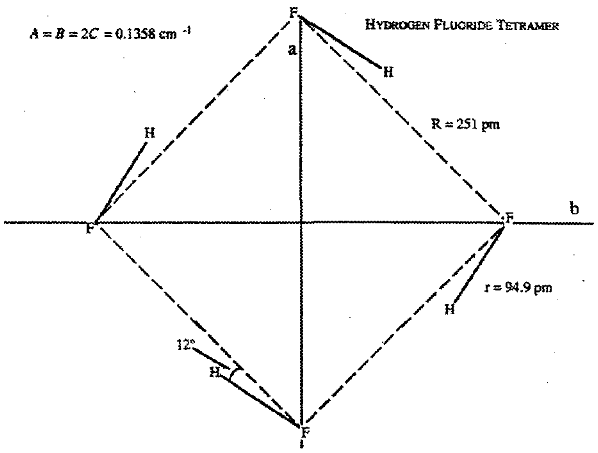

Figure 5.3. The *ab initio* equilibrium structure for hydrogen fluoride tetramer. All atoms lie in the plane and the symmetry is C_{4h}. The structural parameters are from Ref. 2.

accessible to the now-standard molecular beam–infrared laser techniques; but, except for the dimer, there has been little rotationally resolved experimental information for these complexes.

Using our pulsed, slit-jet infrared diode laser spectrometer, we have recorded three rotationally-resolved bands in the 700–800 cm^{-1} region. An intense beam of clusters is formed by expanding a 4% mixture of hydrogen fluoride in helium through a slit nozzle into a vacuum chamber. The beam is interrogated with the output of a lead-salt infrared diode laser. The jet absorption spectrum, along with a reference frequency spectrum, is digitized and recorded by computer. One of the observed bands is of an out-of-plane H–F torsional fundamental (A'') of hydrogen fluoride pentamer centered at 741 cm^{-1}. The band is that of a planar symmetric top (C_{5h} symmetry), as predicted, with a measured ground-state rotational constant B = 0.0755 cm^{-1}; the predicted B value was 0.07667 cm^{-1}. The other bands have been assigned to the hydrogen fluoride tetramer: a perpendicular band centered at 752 cm^{-1} is assigned as an in-plane H–F torsion fundamental (E_u), and a parallel band centered at 714 cm^{-1} is assigned as an out-of-plane H–F torsion fundamental (A_u). Portions of the perpendicular and parallel bands are shown in Figs. 5.4 and 5.5, respectively. The tetramer perpendicular band is strongly perturbed, but a preliminary assignment and fit of the rotational structure gives a ground state B value of 0.130 cm^{-1}. The parallel band fits very well to a semirigid-

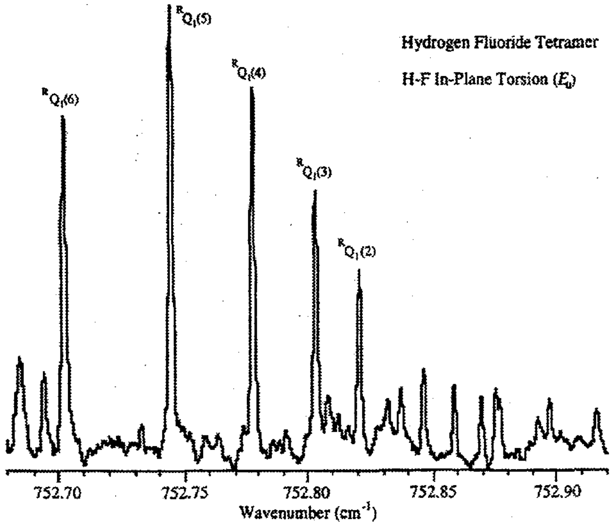

Figure 5.4. A portion of the Q-branch region of the H–F in-plane torsional mode (E_u) of hydrogen fluoride tetramer.

rotor Hamiltonian, and gives a ground state B value of 0.132058(8) cm^{-1}. The predicted B value for the tetramer is 0.1358 cm^{-1}. We are presently extending our spectral searches for other intermolecular bands of $(HF)_n$ and $(DF)_n$ with n = 3–6.

3. *Diborane*

In an effort to improve the spectroscopic constants of the diborane molecule, we have entered into a collaboration with researchers at the National Institute of Standards and Technology and the University of Paris in Orsay. We have recorded several infrared bands from the strong combinations at 3700 cm^{-1} to the far-infrared ring deformation mode at 368 cm^1. These gas-phase spectra were recorded in a room-temperature cell using our Fourier transform spectrometer. The resolution, 0.0017 cm^{-1}, is thirty times better than that of the last "high resolution" study of this molecule in the early 1980s. As a result, we have been able to not only fit a set of ground-state rotational constants from the complete data set, but also have for the first time been able to see the effects of Coriolis coupling perturbations on the rotational structure of the spectra. These effects can now be taken into account when fitting the upper-state vibrational energy levels. The band centers and rotational constants of the resonating dark states have also been determined. The results for the ν_{14}, ν_{17}, and ν_{18} bands have been published.[3] A portion of these spectra is illustrated in Fig. 5.6.

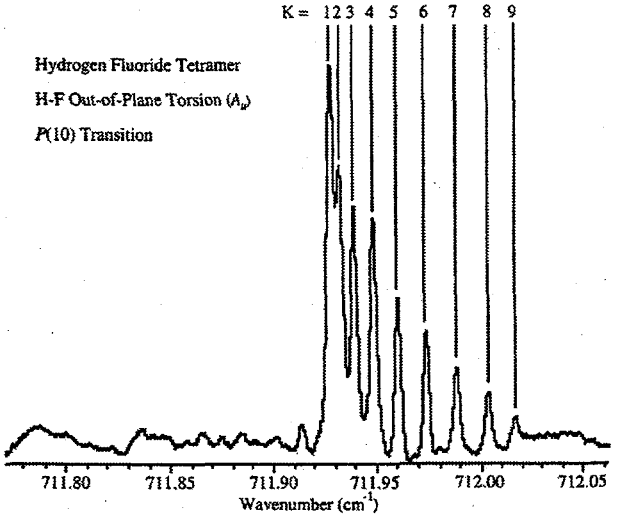

Figure 5.5. A portion of the P-branch region of the H–F out-of-plane torsional mode (A_u) of hydrogen fluoride tetramer.

References

1. M. A. Suhm, *Ber. Bunsenges. Phys. Chem.* **99**, 1159 (1995).
2. C. Maerker, P. R. Schleyer, K. R. Liedl, T.-K. Ha, M. Quack, and M. A. Suhm, *J. Comp. Chem.* **18**, 1695 (1997).
3. R. L. Sams, T. A. Blake, S. W. Sharpe, J.-M. Flaud, and W. J. Lafferty, *J. Mol. Spectrosc.* **191**, 331 (1998).

Characterization of Quantum-Cascade Lasers

S. W. Sharpe, J. F. Kelly, J. S. Hartman,**
C. Gmachl,† F. Capasso,† D. L. Sivco,†
J. N. Baillargeon,† and A. Y. Cho†
Supported by EMSL Operations
and U.S. Department of Energy.
*Energy Division, Engineering and Analytical Sciences Department, Sensors and Measurement Systems Group.
†Bell Laboratories, Lucent Technologies.

Prior to the recent development of quantum cascade lasers,[1] spectroscopists have had a limited selection of compact, high-resolution, tunable, infrared laser sources. Some of these sources include line tunable gas lasers,[2] a variety of systems based on non-linear mixing,[3] and the lead-

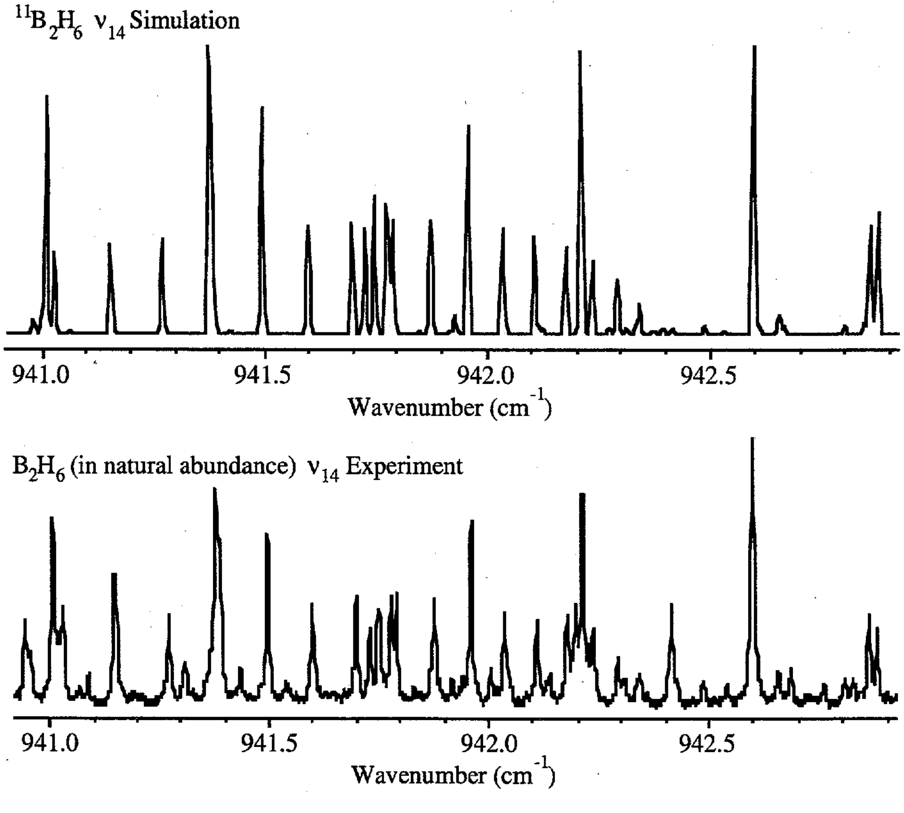

Figure 5.6. A portion of the infrared spectrum of the ν_{14} out-of-plane wag fundamental mode (B_{2u}) of diborane. The upper trace is a simulation of the $^{11}B_2H_6$ isotopomer; the lower trace is the experimental spectrum of diborane in natural abundance: $^{11}B_2H_6$, 64%; $^{11}B^{10}BH_6$, 32%; $^{10}B_2H_6$, 4%.

salt, semiconductor diode laser.[4] It is the latter lasers that have been the work-horse for many high-resolution applications requiring a compact and tunable light source in the mid- to long-wave infrared. Despite their success, lead-salt lasers have a number of serious shortcomings familiar to anyone who has used these devices. In a collaborative effort with Bell Laboratories, Lucent Technologies, PNNL is investigating the lasing characteristics and potential spectroscopic applications for these new devices.

Lasing characteristics were evaluated for distributed-feedback (DFB) quantum-cascade (QC) lasers operating in a continuous mode at cryogenic temperatures. These tests were performed to determine the lasers' suitability for use in high-resolution spectroscopic applications, including Doppler-limited molecular absorption and pressure-limited LIDAR applications. Using a rapid-scan technique, direct absorbance measurements of nitric oxide (NO) and ammonia (NH_3) were performed with several QC lasers operating at either 5.2 or 8.5 μm. Results include time-averaged line widths of better than 40 MHz and long-term laser frequency reproducibility, even after numerous temperature cycles, of 80 MHz or better. Tuning rates of 2.5 cm^{-1} in 0.6 ms can be easily achieved. Noise-equivalent absorbances of 3×10^{-6} have also been obtained without optimizing the optical arrangement.

Laser linewidth was characterized by deconvolving the direct absorbance spectrum of a low-pressure Doppler-limited sample ($P < 2$ Torr) of either nitric oxide (5.2 μm) or ammonia vapor (8.6 μm). The Doppler width for a single rotational-vibrational transition can be calculated using equation (1):

$$\Gamma_D(\text{fwhm}) = 7.162 \times 10^{-7}(T/M)^{1/2}\nu_0, \qquad (1)$$

where T is sample temperature in K, M is molecular mass, and ν_0 is the transition frequency. At T = 293 K and low pressure, NO and NH_3 give rise to absorbance features with full-width-half-maximums (fwhm) of 129.3 MHz (0.00431 cm^{-1}) and 104.9 MHz (0.0035 cm^{-1}), respectively. An absolute frequency scale can be mapped onto the absorption spectrum by scanning the laser over at least two identifiable transitions. Both NO and NH_3 have been well characterized in the mid-infrared spectral regions.

Figure 5.7 shows a trace of the raw digitized spectral data as it would appear on an oscilloscope. Figure 5.8 shows the frequency-scaled absorbance spectrum derived from the trace of Fig. 5.7. The

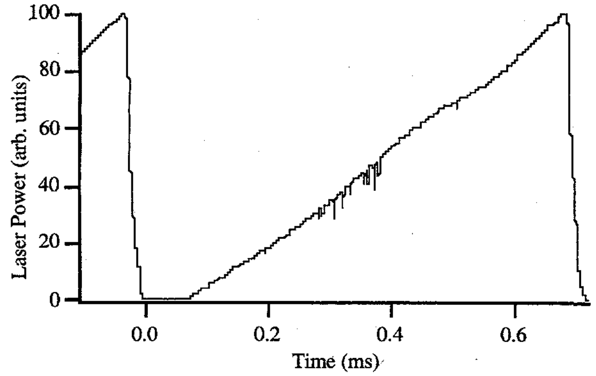

Figure 5.7. Typical raw data trace containing absorbance features corresponding to ammonia vapor. Note that the laser current has been adjusted so that the ramp starts below threshold. The QC lasers tune from blue to red with increasing current.

absorbance plot is created by first generating a baseline and then dividing this baseline, point-by-point, into the raw data array. A polynomial of sufficiently high order is used to generate the baseline, and care is taken not to include the absorbance features in this fit. The $-\log_{10}$ of this ratio (transmittance) yields the absorbance. The frequency scale is generated by fitting the spectral position of each peak as a function of digitizer channel, as shown in Fig. 5.9. A quadratic fit best describes the tuning rate of the DFB-QC laser as a function of applied current. This nonlinear tuning rate with current is similar to that observed for lead-salt diode lasers. Using this current ramping technique, we have been able to scan continuously up to 2.5 cm^{-1}. In separate studies, we have verified that changing the temperature from ~65 to ~85 K allowed us to alter the center frequency continuously over a 10-cm^{-1} region. Throughout this tuning range, we were unable to observe any side-modes, down to –35 dB (technique-limited).

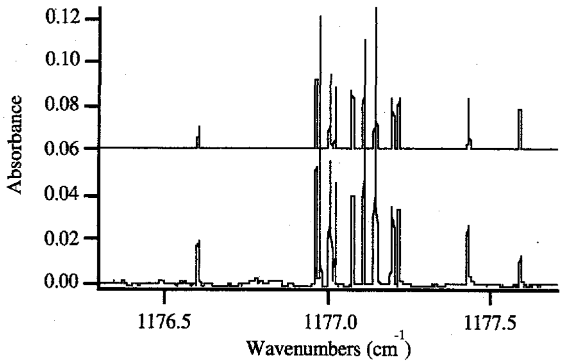

Figure 5.8. Lower trace: absorbance spectrum of ammonia vapor; upper trace: HITRAN simulation.

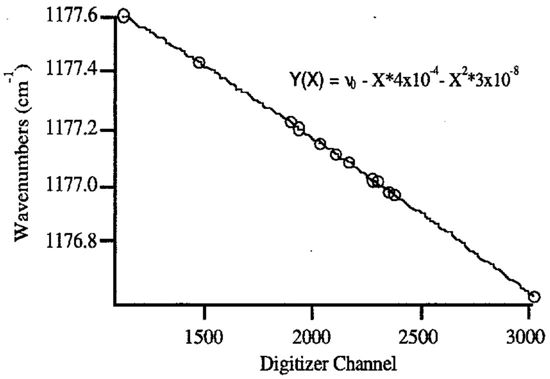

Figure 5.9. Laser frequency vs. digitizer channel. Digitizer channel is equivalent to an increase in time and current.

With an accurate frequency scale in hand, it was possible to fit each absorbance profile to an individual Gaussian function and extract the effective laser linewidth due to instantaneous frequency instabilities and/or drift. For the ammonia trace appearing in Fig. 5.8, we find an average Gaussian width (fwhm) of 134.9 MHz. Assuming that the laser and Doppler profiles add in quadrature, we estimate the average laser line widths over our entire scan to be less than 85 MHz. Several individual profiles yielded abstracted laser linewidths less than 40 MHz. It should be noted that Doppler linewidths for both NO and NH_3 were verified using a high-resolution Fourier transform infrared (FTIR) spectrometer (Bruker HR-120) with a resolution of 40 MHz.

The same basic procedure and analysis was applied to the 5.2-μm DFB-QC lasers by using nitric oxide instead of ammonia vapor. Figure 5.10 shows the characteristic $^2\Pi_{3/2}$ and $^2\Pi_{1/2}$ transitions of NO. In this case, we have chosen to fit the $^2\Pi_{1/2}$ *a* and *f* pair to individual Gaussian profiles. As shown in the inset of Fig. 5.10, the two peaks have fitted widths of 137.9 MHz (fwhm), yielding an abstracted average laser line width of 48 MHz.

In addition to characterizing the laser linewidth, experiments were also performed to determine the noise-averaging characteristics of the QC laser. These experiments involved acquiring 10^n ($n = 0$ to 5) averages over the NO doublet feature. The peak-to-peak noise was then plotted against the

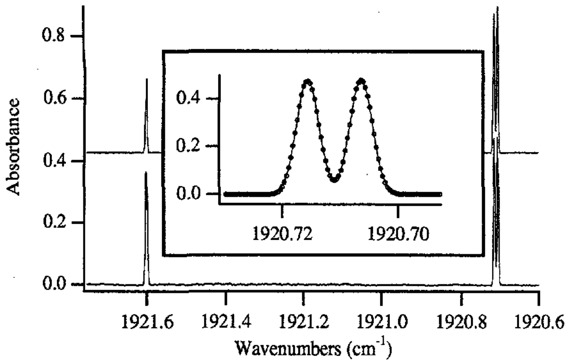

Figure 5.10. Lower trace: absorbance spectrum of NO vapor; upper trace: HITRAN simulation. Inset: Gaussian fit of NO doublet features.

number of averages on a log-log scale. The noise decreased approximately as $\sqrt{N}$ with up to 5 minutes elapsed time, and is consistent with the laser exhibiting low technical noise at these data acquisition bandwidths. Our measured noise equivalent absorbance (NEA) over a 90-μs single scan with 45 mW of received IR power was found to be 1×10^{-3} (P-P), and corresponds to an absorbance sensitivity of 1.9×10^{-5} (P-P) per $\sqrt{Hz}$. Averaging for 10^5 sweeps (11 kHz repetition rate, 3% acquisition duty cycle), we measured a peak-to-peak noise equivalent absorbance of 3×10^{-6}. These values are within a factor of 6.5 from the shot-noise limit for the measured received power.

In conclusion, we have obtained what we believe are the first high-resolution cw spectra obtained with DFB-QC lasers. The results demonstrate that these lasers can be rapidly ramped through a 2.5-cm^{-1} spectral region to obtain direct absorbance spectra. Based on a comparison of the predicted Doppler linewidth with the measured Gaussian width for numerous absorbance features, we estimate the average laser linewidth to be better than 85 MHz under all conditions, and often approach 40 MHz. We believe that these lasers have instantaneous linewidths much narrower than 40 MHz, but effects of optical feedback and power supply noise are limiting. Noise characteristics of the DFB-QC lasers indicate that with some effort it is possible to obtain close to shot-noise limit detection by employing either FM techniques or high-speed ramping schemes with rates of data acquisition greater than 5 MHz. Efforts to demonstrate greater sensitivity and narrower laser line widths are ongoing as we improve our understanding of mitigating power supply noise and optical feedback.

References

1. J. Faist, F. Capasso, D. L. Sivco, C. Sirtori, A. L. Hutchinson, and A. Y. Cho, *Science* **264**, 553 (1994).
2. K. Namjou, S. Cai, E. A. Whittaker, J. Faist, C. Gmachl, F. Capasso, D. L. Sivco, and A. Y. Cho, *Opt. Lett.* **23**, 219–221 (1998).
3. J. Faist, F. Capasso, D. L. Sivco, C. Sirtori, A. L. Hutchinson, M. Beck, S. N. G. Chu, and A. Y. Cho, *Appl. Phys. Lett.* **72**, 680 (1998).
4. J. Faist, C. Gmachl, F. Capasso, C. Sirtori, D. L. Sivco, J. N. Baillargeon, A. L. Hutchinson, and A. Y. Cho, *Appl. Phys. Lett.* **70**, 2670 (1997).

Demonstration of the Asymmetric Ion Trap

S. E. Barlow and M. L. Alexander*
Supported by EMSL Operations.
*EMSL Interfacial and Processing Science.

The Paul trap mass spectrometer is an extremely attractive device for many of mass spectrometric applications. It can be built in a variety of sizes including ones that are readily transportable. Its storage capacity allows for sample integration and MS^n experiments to help resolve analytical issues. Its system requirements for vacuum and electronic support are rather modest, making it among the most cost-effective mass spectrometric detectors known. The Paul trap also has the unique potential capability of operating as a simultaneous cation/anion mass spectrometer, and is the only single instrument with this inherent capability. Several other hybrid type instruments, including the "tandem time-of-flight" mass spectrometer and a combined Penning and Paul trap have also demonstrated similar capabilities. However, these instruments do not generally share the all of the other desirable features of the Paul trap.

For all of its attractive features, the Paul trap has several important limitations that reduce its utility as a general-purpose instrument. Among these are time- and mass-dependent trapping efficiencies and considerable shot-to-shot signal jitter. Further, while the need for a buffer gas to cool ions toward the trap center reduces the absolute vacuum requirements, it also allows for ion-molecule chemistry to occur if the gas composition is not carefully controlled.

We have developed a new electrode and detector design to reduce the shot-to-shot jitter associated with ion ejection.[1-4] Some additional unusual features of our new trap allow excellent access for introducing lasers and solids, either in the form of probe samples or aerosols into the trap. These latter features do not measurably compromise the quality of the observed spectra.

For the Paul trap to function directly as a mass spectrometer, the trapping fields must be dominated by the quadratic (or quadrupolar) terms in the electric potential.[4] Both the radius of the ring electrode (r_0) and the distance of the end electrode from the trap center (z_0) are arbitrary, independent parameters that the trap designer can specify for other purposes. In particular, by moving the exit or detection end cap nearer to the center of the trap than the other one while retaining the harmonic character the trapping field, we greatly increase the likelihood that ions will be ejected from the trap toward the detector rather than in the opposite direction, for the relative energy required to reach one end cap versus the other goes as the ratio of the square of their respective distances.

We chose the end cap dimensions such that when the ring electrode is biased at say 1V, a harmonic well will result when the more distant end cap is biased at –1 V and the near one is set to 0. Using these boundary conditions, we find that

$$z_n^2 = 2z_0^2 - r_0^2,$$

where $z_0 > z_n$ are the end-cap distances. As illustrated in Fig. 5.11, when this relation is used to determine the shape and location of the exit end cap, the biasing of the trap becomes simple. Indeed both the rf and DC (if used) are supplied in essentially the same manner as for a linear quadrupole mass filter. It is the simplicity of the design and its electronic requirements that make this scheme particularly attractive.

Experiments were conducted with a modified Teledyne 3DQ system. Figure 5.12 shows a cross section of the new trap. The new electrodes and spacers were designed to fit in the same space as the original trap, allowing us to use many of the manufacturer-supplied ancillary items such as the solids probe, electron gun, etc. The ring electrode was fashioned in two mating pieces, which allowed us to incorporate large slots through the ring and to implement the internal "cut-back" or relief, which effectively shields the trapping volume from the azimuthal perturbations of the slots. In earlier, unpublished work, we constructed a similar but smaller Paul trap with radial holes and an internal relief. Comparisons between the performance with and without the ring modifications showed no measurable effect on ion storage, ejection, mass resolution, etc. The large slots in the ring electrode do however allow for ready access to the trapping volume for introduction of laser beams, particles and targets for laser desorp-

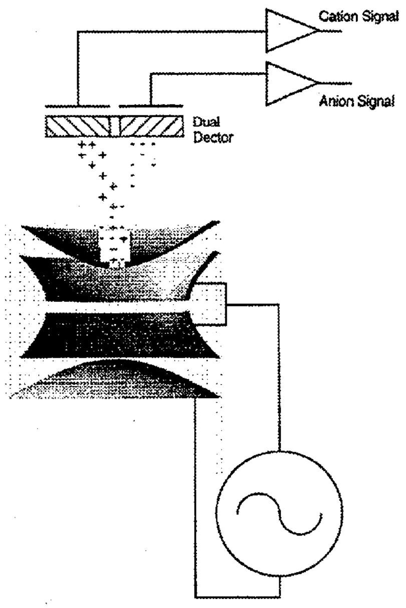

Figure 5.11. Schematic of asymmetric trap and its biasing. Note the split-ring electrode.

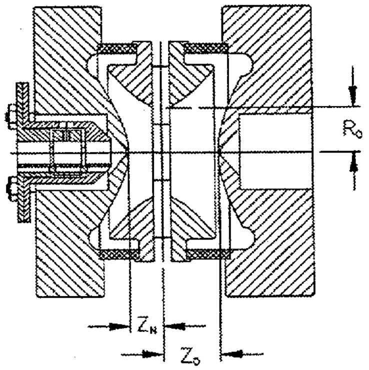

Figure 5.12. Cut-away assembly drawing of asymmetric trap. Note relief cut on the two-piece ring electrode and the large slits.

tion experiments.

In the work reported here ions were scanned out of the trap using a linear ramp on the rf amplitude. Ions were produced both by electron impact ionization and by laser desorption of a solid sample. No rf tickle or secular excitation was used here, although of course it could be readily introduced. For the laser desorption measurements we used a the fourth harmonic of a Nd:YAG laser at 266 nm with a pulse length of 7 ns and a pulse energy of 2 mJ/pulse (0.05 J/cm^2).

Initial tests were conducted by using FC-43 (perflourotributylamine, MW = 671 u) and electron impact ionization and laser desorption/ionization of trichloroethane. Figure 5.13 shows a section of a single-shot dual-polarity spectrum of FC-43. The dips following the two largest peaks in both spectra are due to capacitance mismatching in the detection circuit. Beyond this readily corrected problem, the spectra are surprisingly clean. Figure 5.14 shows a single-shot cation spectrum again of FC-43, but this time we have replaced the two channel microchannel plate with a single channel multiplier with higher gain. Of particular interest in Fig. 5.14 are the surprisingly narrow lines. The line width and apparently improved resolution is probably due to the presence of sixth-order terms in the trapping fields. These terms will arise naturally in the asymmetric trap due to the finite electrode extent.

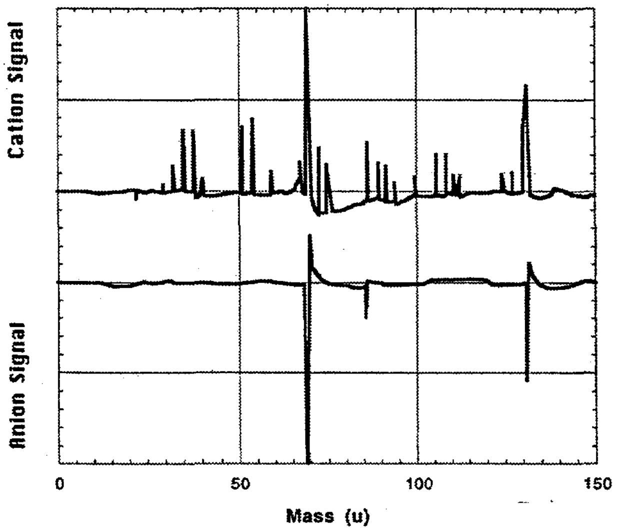

Figure 5.13. Simultaneous cation/anion spectra from FC-43 by electron impact ionization.

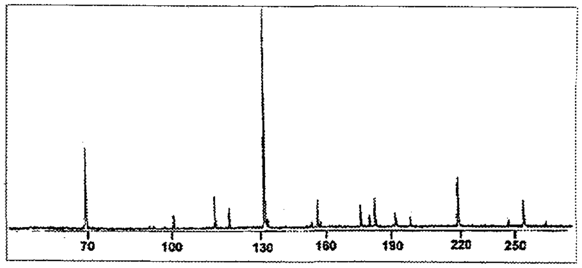

Figure 5.14. Single shot cation spectrum of FC-43 that indicates the inherently narrow line widths obtained using the asymmetric trap.

These preliminary data generated with the new asymmetric Paul trap verify many of the characteristics that were theoretically predicted, including improved signal to noise and the ability to do simultaneous cation/anion mass spectrometry. As an unexpected bonus, we have discovered that the mass resolution of this new trap is at least as good to those of the "stretched" traps, where small sixth-order terms have been added. Consideration of the trap design lead us to conclude that this is due to the unavoidable presence of higher order terms in the actual construction of the instrument. However, this trap should perform in a manner much closer to elementary theory than standard rf traps, because the electric fields are in fact very linear.

References

1. M. L. Alexander, P. H. Hemberger, M. E. Cisper, and N. S. Nogar, *Anal. Chem.* **65**, 1609 (1993).
2. M. L. Alexander, S. E. Barlow, and J. C. Follansbee, *Proc. 46th ASMS Conf.* 1173 (1998).
3. S. E. Barlow, M. L. Alexander, and J. C. Follansbee, "The Asymmetric Ion Trap," U.S. Patent 5,693,941 (1997).
4. D. Gerlich, *Adv. Chem. Phys.* **82**, 1 (1992).

Radiative Association of Cs^+ with 12-crown-4 Ether at 288 K

*S. E. Barlow and M. D. Tinkle**

Supported by EMSL Operations and DOE Office of Basic Energy Sciences.

*Postdoctoral Research Associate.

We have developed a new Fourier-transform ion cyclotron resonance mass spectrometer (ICR) specifically designed for chemical kinetics experiments.[1] During the course of the initial testing, we were able to repeat the radiative association measurements of Chu et al.,[2] but with improved precision.

This improvement in precision can be attributed to several design feature of the instrument. First, the ion trap itself has almost no fourth-order terms in the electrostatic trapping field, so the frequency response is quite linear over a broad range of excitation amplitudes and ion numbers. The quadratic trap also allows us to operate with much deeper trapping wells than is standard practice with conventional instruments, so evaporative ion losses are largely eliminated. Second, the simple trap geometry (basically a closed cylinder) allows us to calculate *a priori* the expected image charge effect on magnetron motion. Third, the instrument is fitted with very stable, externally mounted electron and cesium ion guns, giving excellent reproducibility of ion samples. Fourth, it has an auxiliary gas handling system that provides a constant flow of reactant gas into the trap volume. Finally, we make use of improved theoretical treatments in our data analysis.

We have measured the rate constant for the attachment of 12-crown-4 ether (12c4) to cesium ions, and also the rate constant for attachment of a second crown to the resulting complex. Crown ethers are being studied at PNNL for the specificity with which they bind particular alkali cations, which may make possible the extraction of radioactive strontium and cesium from high-level radioactive wastes at Hanford.[3] At low pressures in the gas phase, the attachment is believed to be stabilized by the emission of radiation, rather than by additional collisions.[2]

The measurement is straightforward. A stable low pressure of 12c4 is maintained in the chamber by admitting a steady flow through a capillary from a gas manifold. The compound is condensable, so sufficient time must be allowed for a steady condition to be reached. A cesium ion beam with energy 10 eV and current 115 pA is passed through the trap for 2 seconds with the trapping potential set to $V_T = 8$ volts, corresponding to a 5.21-volt well depth. Some of these ions lose enough energy by collisions with molecules of 12c4 to be trapped. After an additional delay during which association reactions occur, the product ions are analyzed by FTICR. Only three mass peaks are seen, at m/z values of 132.9, 309.0, and 485.1, corresponding to Cs^+, $Cs^+(12c4)$, and Cs^+-$(12c4)_2$ respectively.

The peak heights recorded as a function of the delay time are shown in Fig. 5.15, along with the sum of the three peaks. For about four seconds after the ion beam is shut off, the sum continues to rise, even though no new ions are being trapped. During this time, the Cs^+ ions are cooling by collisions with neutrals, and the ICR motion of the initially hot cloud is more strongly damped than usual. From four seconds on, the sum of the peak heights is nearly constant for the remainder of the data, indicating that no ions are lost to other channels, and that the individual peak heights are good measures of the relative numbers of ions of each species. Other than the early cooling period, the data indicate two sequential attachment reactions. The attachment rates found from fits to the exponential portions of the data are $0.18 \pm 0.01\ s^{-1}$ for the reaction

$$Cs^+ + 12c4 \rightarrow Cs^+(12c4) \qquad (1)$$

and $0.018 \pm 0.001\ s^{-1}$ for

$$Cs^+(12c4) + 12c4 \rightarrow Cs^+(12c4)_2. \qquad (2)$$

The curves in Fig. 5.15 are solutions of a simple pseudo–first-order kinetics model using these rates.

To convert the measured rates into absolute rate constants, we need to know the neutral gas density. This is a difficult problem in a UHV chamber, especially with a strong magnetic field, and it is the dominant source of uncertainty in measurements of gas-phase rate constants at pressures below 10^{-5} Torr. With the pressure steady (as indicated by an ionization gauge outside the magnet bore), an electron beam is passed through the trap with trapping potentials applied to the endcaps. The number of ions trapped per second is

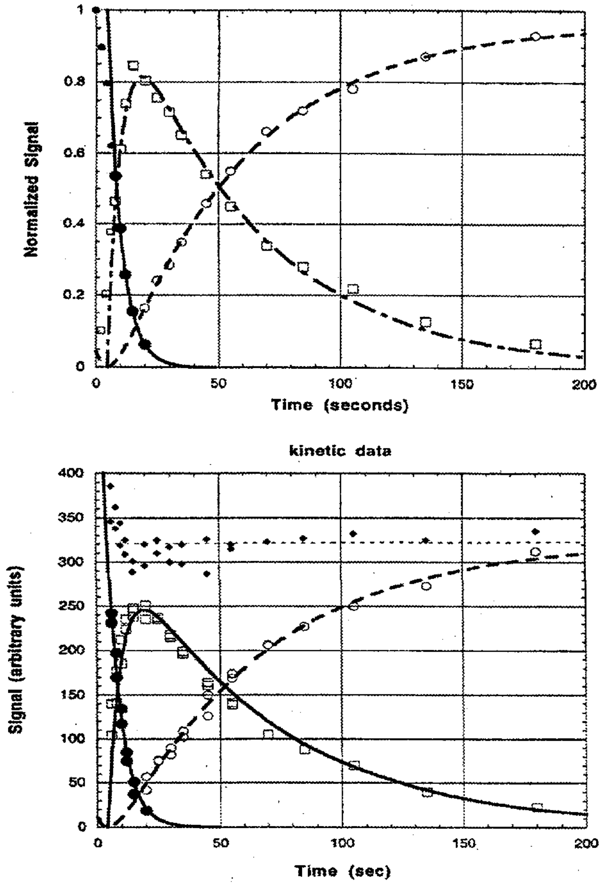

Figure 5.15. ICR response vs. time for Cs^+ (solid circles), $Cs^+(12c4)$ (squares), $Cs^+(12c4)_2$ (open circles) and total signal (diamonds). The data in Fig 1a (above) are normalized and the lines are sequential least-squares fits to the analytic solutions of the coupled kinetic equations. Fig 1b (below) shows unnormalized data using the same fits. Data from the first six seconds was not used in the rate fitting. These data appear with the same symbols, but made smaller for clarity, in Fig. 1a. The deviation from the theoretical fit is clear.

$$dN/dt = n_0 \sigma_i L I / q,$$

where n_0 is the density of neutrals, σ_i is the ionization cross-section, L is the length of the trap plus the length of the endcap entrance and exit tubes,[1] I is the electron beam current, and q is the charge of the electron. Thus if σ_i is known, n_0 can be found from a measurement of dN/dt. From comparison with ion gauge sensitivities for similar compounds that have known ionization cross sections, we estimate $\sigma_i \approx 5.6 \pm 1.2 \times 10^{-15}$ cm^2 for 12c4 with 100-eV electrons. To find dN/dt, we vary the time the electron beam is left on and measure the magnetron frequency in each case (see Fig. 5.16). The frequency shift is proportional to the stored charge, and the proportionality factors have been calculated for the standard ICR trap geometries.[1] For our trap in our magnetic field, the shift is 3.06 Hz per million elementary charges. The slope of the data in Fig. 5.16 divided by this factor gives an ion production rate of 1.06 million ions per second with a 10-nA beam current, for a measured neutral density of $n_0 = 1.5 \pm 0.4 \times 10^9$ cm^{-3}. The absolute rate constants are thus $k_1 = 1.2 \pm 0.3 \times 10^{-10}$ cm^3/s for attachment of the first 12c4, $k_2 = 1.2 \pm 0.3 \times 10^{-11}$ cm^3/s for attachment of the second.

Using available estimates of the dipole moment (1.78 D) and optical index of refraction for 12-crown-4 (1.4621), we find the polarizability to be $\alpha = 1.76 \times 10^{-3}$ cm^3. Using the standard theory,[4] we find the collision rate constants are 1.7×10^{-9} cm^3/s for Cs^+ with 12c4 and 1.4×10^{-9} cm^3/s for collisions with a second crown ether; the difference between these two numbers comes from the change in reduced mass due to reaction. Dividing the measured association rate constants by these collision rate constants, we find that the probability for attachment during a collision is 0.07 ± 0.02 for the first 12c4 and 0.009 ± 0.002 for attachment of the second.

We also conducted a short set of measurements

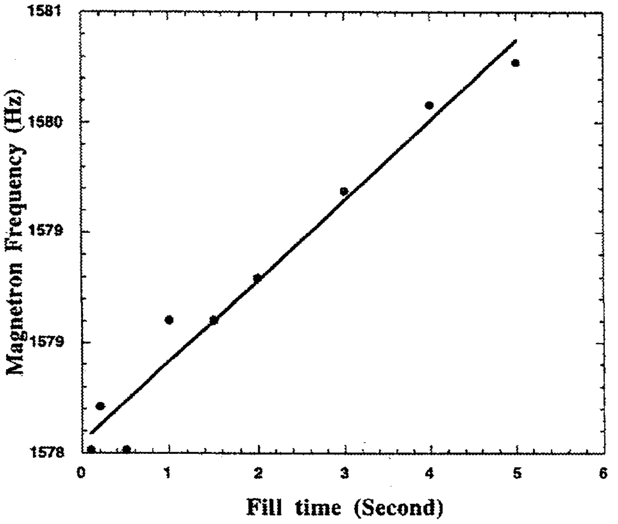

Figure 5.16. Magnetron frequency vs. "fill time." This is a direct measure of total ion number in the trap. Fill time is the time of operation of the electron beam ionizer at 100 eV with 10.0 nA of current.

that examined collision-induced dissociation (CID) of $Cs^+(12c4)_2$ by background 12c4. We found that with center of mass collision energies of about 0.15 eV, one quarter of the dimer was dissociated to the monomeric form with little or no formation of Cs^+. By the time the energy was raised to 0.5 eV we found about 40% dissociation with substantial loss of both ligands. Raising the energy still further to about 1.5 eV caused complete loss of the dimer—about 80% had been driven back to the bare cesium ion. These results are in qualitative agreement with the much more detailed CID measurements of Moore et al.[3] These workers found serious disagreement between their measured $Cs^+(12c4)$ binding energy and high-level calculations. To explain their results, they hypothesized that a barrier exists in the complex for the 12c4 to flip from its S_4 gas-phase equilibrium conformation to the lower-energy C_4 state that it should assume as a ligand. Our results qualitatively support this conclusion; further, they imply that the barrier between the two states must be quite substantial. The reason for this is that in the ICR the ions have several minutes to relax, during which time the ions are undergoing collisions with 12c4, which should effectively remove excess energy and achieve radiative equilibrium with the trap walls. Further, we may infer that when the second ligand attaches to the cluster, it also adds exclusively in the S_4 conformation.

The improved precision of the measurement is due to a combination of factors related to the instrumentation. First, we employ a "precision"' ion trap that allows us to operate effectively in a much deeper electrostatic well than is common practice in most ICR work; the result, shown in Fig. 5.20, is that we do not lose ions to axial evaporation. A second benefit of the precision of the trap is that we have a large linear volume of parameter space as illustrated in Fig. 5.16. Third, advances by us in understanding trap phenomena and calculation image charge effects allow us to independently quantify ion number without regard to ion mass. Finally, we have a high quality, actively-controlled gas handling system that allow us to deliver a very stable flow of reactant gas to the ion trap.

References

1. S. E. Barlow and M. D. Tinkle, *Int. J. Mass Spectrom. Ion Proc.*, in preparation.
2. I. H. Chu, H. Zhang, and D. V. Dearden, *J. Am. Chem. Soc.*, 115, 5736 (1993).
3. M. B. Moore, D. Ray, and P. B. Armentrout, *J. Phys. Chem. A* **101**, 7007 (1997).
4. B. P. Hay, personal communication.

A New Approach to Near-Field Fluorescence Microscopy: Two-Photon Excitation with Metal Tips

E. J. Sánchez,* L. Novotny,† and X. S. Xie

Supported by EMSL Operations.
*Graduate Student, Portland State University.
†Postdoctoral Research Associate.

The general aim of near-field optics is to extend optical microscopy beyond the diffraction limit. The widely adapted aperture approach is based on an aluminum-coated fiber tip,[1] of which the foremost end is left uncoated to form a small aperture. Unfortunately, only a tiny fraction ($<10^{-4}$ for a 100-nm aperture) of the light coupled into the fiber is emitted by the aperture because of the cut-off of propagation of the waveguide modes. The low light throughput and the finite skin depth of the metal are the limiting factors for resolution. Many applications require spatial resolutions that are not obtainable with the aperture technique. For example, in our effort on spectroscopic imaging of photosynthetic membranes,[2] a spatial resolution of at least 20 nm was desired in order to resolve closely-packed individual proteins in a lipid membrane. Moreover, the aperture technique has other practical complications: (1) it is difficult to obtain a smooth aluminum coating on the nanometric scale, which introduces non-reproducibility in probe fabrication as well as measurements; (2) the flat ends of the aperture probes are not suitable for simultaneous topographic imaging at high resolution; and (3) the absorption of light in the metal coating causes significant heating and poses a problem for biological applications. To overcome these limitations, we have developed a new approach for high-resolution fluorescence imaging based on a sharp, laser-illuminated metal tip.

We use the metal tip to provide a local excitation source for the spectroscopic response of the sample under investigation. Excitation light of proper polarization induces a strongly enhanced field at the tip. The enhanced field consists mainly of non-propagating (evanescent) components and is, thus, strongly confined to the tip end.

Figure 5.17a shows a field emission electron micrograph of a gold tip with an end diameter of 15 nm that we fabricated with etching and subsequent focused ion beam (FIB) milling. Because of the bent shape, the field enhancement can be excited by light polarized in the horizontal direction. Figure 5.17b shows the calculated field intensity distribution at the end of a symmetrical gold tip tilted from the vertical direction, mimicking the situation in Figure 5.17a. The electric field intensity at the tip end is found to be enhanced by a factor of $f \approx 1000$. The calculated fields are rigorous three-dimensional solutions of Maxwell's equations obtained by the multiple multipole approach.[3] The field enhancement arises from a high surface charge density at the tip that is induced by the incident light polarized along the tip axis.[3]

The enhanced field at a gold tip is used here as an excitation source for molecular fluorescence. In order to enhance the near-field contrast, we utilized two-photon excitation of fluorescence that has found wide applications in far-field microscopy. Since two-photon excitation is a non-linear process with quadratic dependence on excitation intensity, the detected fluorescence signal becomes proportional to the square of the intensity enhancement factor, $f^2 \approx 10^6$. Therefore, two-photon excitation leads to a significantly improved contrast.

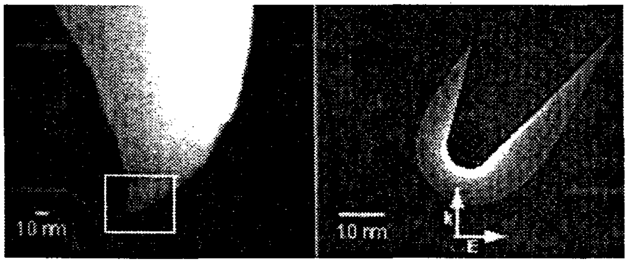

Figure 5.17. (a, left) Scanning electron micrograph of an asymmetrical gold tip fabricated by FIB in order to achieve field enhancement with the horizontal polarization of a focused laser beam. (b, right) Calculated intensity distribution near a gold tip mimicking the tip in (a); *k* and *E* indicate the propagation direction and polarization of the incident field, respectively. An enhancement factor of 1000 in intensity over the incident light is present at the tip end. The calculation is a three-dimensional solution of Maxwell's equations obtained by the MMP method.

The metal tip is maintained within 2 nm above the sample surface by using a tuning-fork feedback mechanism. The use of a metal tip only a few nanometers away from a chromophore raised concerns about fluorescence quenching by the metal tip. Fortunately, this problem was minimized for samples of molecular aggregates such as J-aggregates and fluorescent proteins in photosynthetic membranes. In particular, psuedo-isocyanine (PIC) dye molecules in J-aggregates have extremely fast energy transfer along the aggregate length with an upper bound of coherent length of 50 nm, whereas the chlorophyll a (Chl a) and chlorophyll b (Chl b) molecules in Light Harvesting Complex (LHC-II) are separated by only a couple of nanometers, according to the crystal structure. Rapid energy transfer in these systems allows the fluorescence emission to take place far from the metal tip so that fluorescence quenching by the metal is reduced.

Figure 5.18 shows the simultaneous images of topography and near-field two-photon excited fluorescence for J-aggregates of PIC dye molecules in polyvinyl sulfate (PVS). After preparation of the aggregates in the PVS matrix, we applied deionized water to remove much of the PVS polymer. This left a thin aggregate layer on the surface, ranging from ~50 nm to ~5–10 nm in height, as seen by the topographic image. All fluorescence features occurred both in the trace and retrace of the same scan line. The lower portions of Fig. 5.18 show the simultaneous cross-sections taken across the aggregate strands (dotted white line). The arrows in the topography cross-section indicate a feature with fwhm of ~35 nm, while the corresponding fluorescence cross-section has a fwhm of 30nm. This width is narrower than previously seen with the aperture approach. This image demonstrates the superior spatial resolution of the present approach.

We have demonstrated a new approach for near-field fluorescence imaging with an unprecedented spatial resolution. The technique takes advantage of a localized excitation induced by the highly enhanced *E*-field around a nanometrically fabricated metal tip, as well as by multi-photon excitation, and overcomes difficulties of the aperture

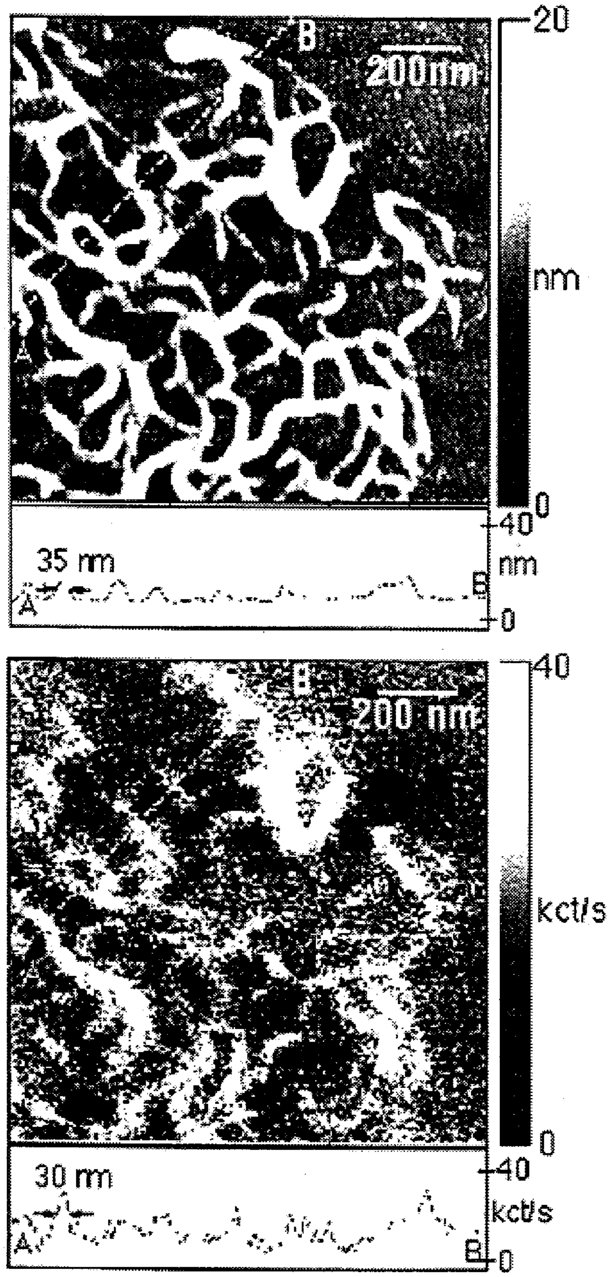

Figure 5.18. Simultaneous topographic image (a) and near-field two-photon excited fluorescence image (b) of J-aggregates of PIC dye in a PVS film on a glass substrate. The topographic cross-section along the dashed line (A–B) has a particular feature of 35-nm fwhm (indicated by arrows) and a corresponding 30-nm fwhm in the emission cross-section.

approach, opening the possibility of spectroscopic mapping on the nanometer dimension, to resolve individual proteins in lipid membranes.

References

1. E. Betzig et al., *Science* **251**, 1468 (1991); E. Betzig and J. K. Trautman, *Science* **257**, 189 (1992).
2. R. C. Dunn, G. R. Holtom, L. Mets, and X. S. Xie, *J. Phys. Chem.* **98**, 3094 (1994).
3. L. Novotny, E. J. Sánchez, X. S. Xie, *Ultramicroscopy* **71**, 21 (1998); L. Novotny, R. X. Bian, and X. S. Xie, *Phy. Rev. Lett.* **79**, 645 (1997).

Three Dimensional Vibrational Imaging by Coherent Anti-Stokes Raman Scattering

A. Zumbusch,* G. R. Holtom, and X. S. Xie

Supported by EMSL Operations.
*Postdoctoral Research Associate.

A variety of new imaging capabilities capable of producing three-dimensional profiles of biological and chemical samples is emerging, especially confocal microscopy and multiphoton fluorescence methods. These techniques require either intrinsic fluorescent species or addition of a label. We have developed a Raman imaging technique that is based on vibrational properties of the sample, and that is sensitive to species not excited electronically by visible light.

We employ coherent anti-Stokes Raman scattering (CARS) to overcome the low signals typical of spontaneous Raman methods. Sub-picosecond pulses in the near infrared, separated in frequency by a molecular vibrational mode, are focused to sub-micron spots with a microscope objective. At the focal point a new light beam is generated with a wavelength shorter than the incident beams, and whose intensity reports the concentration of the molecular species in resonance. Due to the high peak power of our light source, we generate detectable signals at 0.1 mW average power, which is tolerated by most samples. The sample is raster scanned to generate a two-dimensional image, then repeated to generate a series of image planes for a three-dimensional image.

Figure 5.19 shows CARS images of live cells, demonstrating the capability of this system.

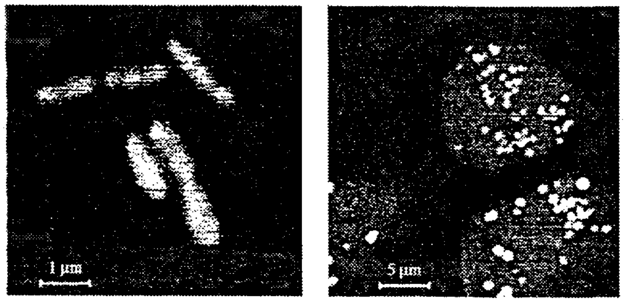

Figure 5.19. (a) CARS image of six live, unstained bacteria of the type *Shewanella putrefaciens*, strain CN-32, in D_2O. The Raman shift is 2878 cm^{-1}, in the spectral region of aliphatic C–H vibrations. (b) CARS image of three live, unstained HeLa cells in aqueous HEPES buffer solution. The Raman shift is 2913 cm^{-1}, in the spectral region of aliphatic C–H vibrations. The bright features are mitochondria that are rich in aliphatic CH.

Single-Molecule Enzymatic Dynamics

H. P. Lu, L. Xun, and X. S. Xie*

Supported by DOE Office of Basic Energy Sciences.

*Washington State University.

Single-molecule studies of chemical and biological systems have provided new information that is not obtainable from ensemble-averaged measurements.[1] The single-molecule approach is particularly powerful in investigating dynamical behaviors of macromolecules in real time, such as interfacial electron transfer,[2] molecular conformational change at interfaces[3] and in proteins,[1,4] and enzymatic reactions.[4]

Cholesterol oxidase (COx) from *Brevibacterium sp.* is a monomeric protein of 53 kDa. Flavin adenine dinucleotide (FAD) is a coenzyme and non-covalently bound to protein matrix at an active site. Each COx molecule contains only one FAD. In the oxidized form, FAD absorbs excitation photons at 450 nm and emits fluorescence at 520 nm. During cholesterol oxidation in an enzymatic turnover cycle, FAD is first reduced to $FADH_2$, and then reoxidized back to its original form by oxygen. The reduced $FADH_2$ is non-fluorescent. The blinking behavior in single-molecule fluorescence trajectories can also be explained by the following scheme:

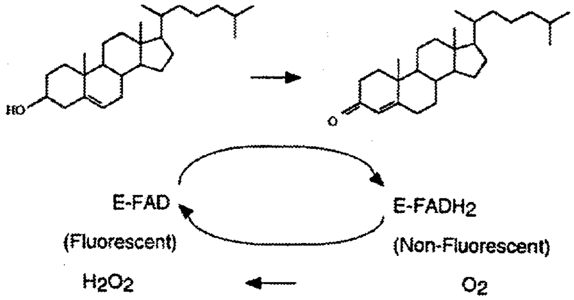

The enzymatic turnover reaction can be expressed by the Michaelis-Menten mechanism:

$$\mathrm{FAD} + \mathrm{S} \underset{k_{-1}}{\overset{k_1}{\rightleftharpoons}} \mathrm{FAD\text{-}S} \xrightarrow{k_2} \mathrm{FADH_2} + \mathrm{P}$$

$$\mathrm{FADH_2} + \mathrm{O_2} \underset{k''_{-1}}{\overset{k''_1}{\rightleftharpoons}} \mathrm{FADH_2\text{-}O_2} \xrightarrow{k''_2} \mathrm{FAD} + \mathrm{H_2O_2} \qquad (1)$$

where S and P represent substrate and product, respectively.

Figure 5.20 (lower panel) shows a portion of a long fluorescence intensity trajectory recorded from a single COx molecule with 0.2 mM cholesterol and 0.25 mM oxygen at pH 7.4. Stochastic blinking behavior that gives on-times and off-times in this intensity trajectory is evident. Extensive control experiments had shown that the origin of the intensity-blinking behavior in this single-molecule system is enzymatic turnovers: toggling the redox form of FAD in enzymatic reaction cycles.[4]

Figure 5.21A shows a typical on-time distribution derived from a long intensity trajectory at 2-mM cholesterol substrate. The apparent deviation of the distributions from Poisson distributions indicates that the forward reaction, Eq. (1), involved an intermediate state, and the intermediate complex formation step is the rate-limiting step. The FAD reduction process, k_2, became the rate-limiting step when 5-pregene-3β-20α-diol was used as substrate with 10 times higher concentration. The 5-pregene-3β-20α-diol substrate gives a slower k_2 than cholesterol substrate does. In this case, we found that k_2 varies from 3 to 14 s^{-1} among the molecules examined,[4] and k_2' are nearly uniform, 3.2 ± 0.5 s^{-1}. Seemingly identical COx molecules have significant different k_2, reflecting static disorder in the FAD reduction process.

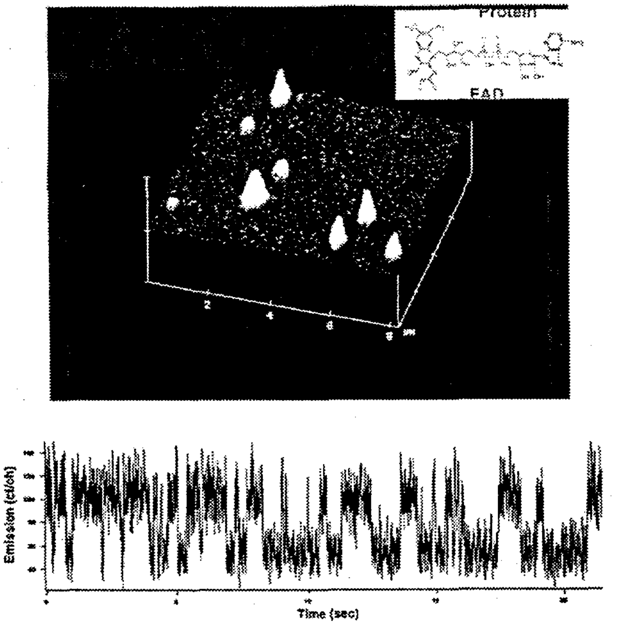

Figure 5.20. Fluorescence image (8 μm × 8 μm) of single COx molecules immobilized in a thin film of agarose gel of 99% buffer solution (pH 7.4). This image was taken in 4 minutes with an inverted fluorescence microscope by raster-scanning the sample with a focused laser beam of 500 nW at 442 nm. Each individual peak is attributed to a single COx molecule. The fluorescent FAD active site is shown in the inset. The intensity variation between the molecules is due to different longitudinal positions in the light depths. The single molecules of COx were confined in agarose gel of 99% water with no observable translational diffusion. However, the COx molecules were freely rotating within the gel. The lower panel shows a portion of an emission intensity trajectory of a single COx with 2-mM steroid substrate. The enzymatic turnovers of a single COx molecule catalyzing oxidation of cholesterol molecules are observed in real time.

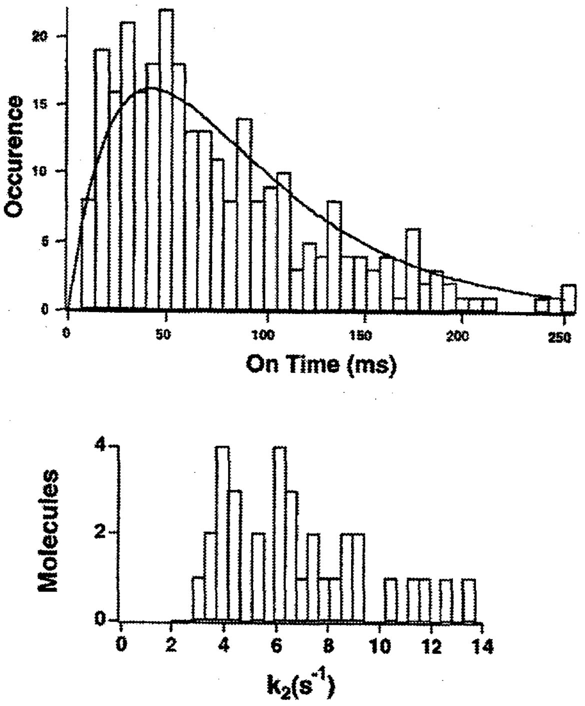

Figure 5.21. (A, above) Distribution of on-times (bars) derived from the emission trajectory of another single COx molecule recorded at 2-mM cholesterol concentration. The simulated curve (solid line) is based on Eq. (1), assuming $k_1 = 33 \pm 6$ s^{-1}, $k_2 = 17 \pm 2$ s^{-1}, and $k_{-1} = 0$. (B, below) The distribution of k_2 derived from the on-time distributions of 33 COx molecules in the same sample. The static disorder of k_2 is evident.

Dynamic disorder originates from reaction rate fluctuations. The dynamic disorder can be evaluated by the conditional probability distribution, $p(X,Y)$, for pairs of on-times (X and Y) separated by a certain number of turnovers. Figure 5.22A and B are, respectively, the two-dimensional (2-D) histograms of a pair of on-times adjacent to each other and separated by 10 turnovers. In the absence of dynamic disorder, $p(X,Y)$ should be independent of the separation between the two on-times. In contrast, for adjacent pairs of on-times (Fig. 5.22A), there is a diagonal feature, indicating that a short on-time tends to be followed by another short on-time, and a long on-time tends to be followed by another long on-time. For the separation of 10 turnovers (Fig. 5.22B), the memory is lost.

To further evaluate the memory times in the COx, we calculated the autocorrelation functions of on-time trajectories. Fig. 5.22C shows an autocorrelation function of on-times, $r(m)$, where m is the index number in on-time sequence derived from a single-molecule turnover trajectory measured at 2-mM 5-pregene-3β-20α-diol substrate. Under these conditions, FAD reduction, k_2, is the rate-limiting step. The non-zero $r(m)$ at $m > 0$ with a decay constant of 1.8 ± 0.4 sec indicates a memory effect among on-times. Converting the decay constant of $r(m)$ based on an average turnover of about 0.6

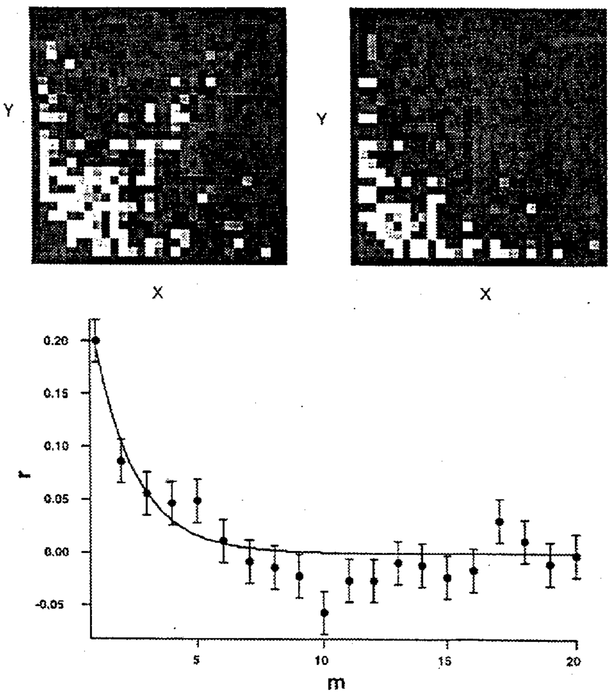

Figure 5.22. (A, upper left) The two-dimensional (2-D) conditional probability distribution for a pair of on-times (*X* and *Y*) separated by a certain number of turnovers. The scale of the *X* and *Y* axes are from 0 to 1 s. The 2-D conditional histogram for on-times of two adjacent turnovers is derived from the trajectories of 33 COx molecules with 2-mM 5-pregene-3β-20α-diol substrate. A subtle diagonal feature is present. (B, upper right) The 2-D conditional histogram for two on-times separated by 10 turnovers for the COx molecules in (A). The diagonal feature vanishes because the two on-times become independent at the 10-turnover separation. (C, below) The autocorrelation function of on-times, *r*(*m*), *m* being the index number of turnovers, for a single COx molecule with 2 mM of steroid substrate. The solid line is a single exponential fit with a decay constant of 1.6 ± 0.5 turnovers. With the averaged turnover cycle of 600 ms, we deduce a correlation time of 1.0 ± 0.3 s for the fluctuating k_2 of this molecule. If there were no dynamic disorder, $r(m) = 0$ for $m > 0$. The decay of *r*(*m*) indicates the fluctuation of k_2.

sec, we found the memory time was 1.1 ± 0.4 sec. Interestingly, this is the same time scale of turnover time (0.5 ~ 2 sec). In contrast, we did not find a memory effect in off-time time sequence, i.e., *r*(*m*) of off-times are zero when $m > 0$. This memory effect in FAD reduction arises from the fluctuation of reaction rate k_2. The correlation time derived from *r*(*m*) represents the time scale of fluctuation. Rate fluctuation can be directly related to the fluctuation of reaction barrier height. The height of a reaction barrier can be changed by conformational fluctuation of the protein.

Possible origins of the enzyme protein conformational changes are spontaneous, ligand-binding-induced or reaction-induced. The conformational changes around the FAD should be related to the reactivity and the fluorescence fluctuation of the FAD. To further investigate the physical nature of dynamic disorder of the COx enzyme, we measured the fluorescence spectral trajectory in the single-FAD active site without adding substrate, i. e., without the substrate- and reaction-induced conformational changes. Figure 5.23 shows the autocorrelation function of spectral mean trajectories derived from a sequence of spectra collected at 100-ms exposure time. The decay time from a single exponential fit is 1.5 ± 0.4 s. This result demonstrated the existence of the spontaneous conformational fluctuation. Interestingly, the time

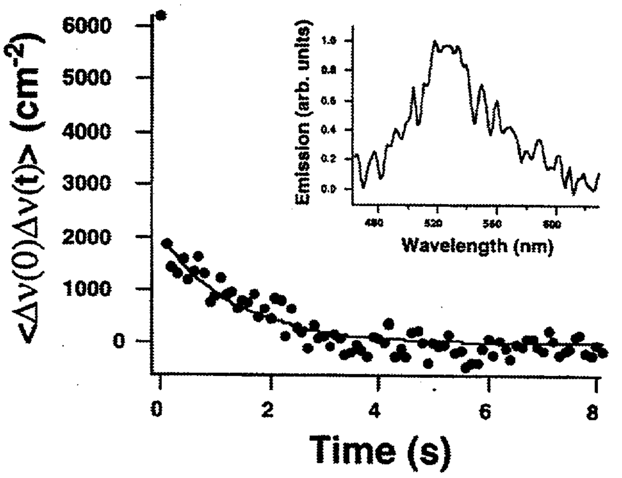

Figure 5.23. The autocorrelation function (dots) of spectral mean for a spectral mean trajectory. The solid line is a fit by a single exponential with a time constant of 1.3 ± 0.3 s. We attribute the fluctuation of k_2 to conformational fluctuation of the protein, which can be probed by the emission spectra of the FAD active site. The decay constant is of the same time scale as k_2 fluctuation, providing strong evidence that an equilibrium fluctuation in conformation results in variation of the enzymatic rate, k_2. The inset shows the emission spectrum of a COx molecule taken in 100 ms.

scale of the conformational fluctuation is of the same time scale as enzymatic turnovers and the memory effect of COx.

We have shown that single-molecule spectroscopy can provide detailed information about the enzymatic reaction of COx, beyond the Michaelis-Menten mechanism, and not obtainable in ensemble-averaged measurements. We also find that the spontaneous conformational fluctuation leads to the memory effect in the enzymatic activity of COx.

References

1. For a recent review, see X. S. Xie and J. K. Trautman, *Ann. Rev. Phys. Chem.* **59**, 441 (1998).
2. H. P. Lu and X. S. Xie, *J. Phys. Chem. B* **101**, 2753 (1997).
3. H. P. Lu and X. S. Xie, *Nature* **385**, 143 (1997).
4. H. P. Lu, L. Xun and X. S. Xie, *Science* **282**, 1877 (1998).

Fluorescence Spectroscopy and Exciton Dynamics of Single Allophycocyanin Trimers

L. Ying* and X. S. Xie

Supported by DOE Office of Basic Energy Sciences.

*Graduate Student, Peking University.

One of the interesting applications of single-molecule spectroscopy is the study of the exciton dynamics of molecular aggregates, which have been explored by a few groups. With confocal microscopy, two detailed studies of the single light-harvesting complex LH2 from *Rhodopseudomonas acidophila* and single conjugated polymers have been carried out recently by Hochstrasser and coworkers[1] and by Barbara and coworkers,[2] respectively. Both groups showed that in addition to one-step bleaching, single aggregate emission can be switched between on and off states by the formation of exciton traps, which quench the fluorescence during the emission off-time. The exact chemical nature and mechanism of formation for the exciton traps are not yet known. In the case of light-harvesting complex LH2, it was suggested that radical cations of bacterial chlorophyll *a* are formed via photo-induced electron transfer.[1,2] We report a series of single-molecule experiments done on allophycocyanin (APC), a simpler and well-characterized molecular aggregate. The motivation of this work is to reveal the underlying mechanisms for photochemistry and photophysics of single APC trimers.

APC is located in a light-harvesting apparatus in cyanobacteria, responsible for efficient capturing and funneling electronic excitation to the membrane-bound photosynthetic reaction centers (PS II), where fast electron transfer occurs with high efficiency, converting solar energy to chemical energy. A schematic representation of the structure is shown in Fig. 5.24. Three $\alpha\beta$ monomers are arranged around a threefold symmetry axis to form a trimer $(\alpha\beta)_3$ which has a diameter of ~11 nm, a thickness of ~3 nm, and a central channel 3.5 nm in diameter. In each monomer, an α or β polypeptide chain covalently binds a phycocyanobilin (open-chain tetrapyrrole) chromophore through a cystein residue α84 or β84. Upon aggregation to a trimer, the α84 chromophore in one monomer is brought close to the β84 chromophore in an adjacent monomer, forming a strongly interacting pair with a center-to-center distance of 2 nm. The absorption spectrum of APC trimer is significantly different from that of the monomer, with a red-shifted sharp peak at 654 nm.

We have investigated individual APC trimers under ambient conditions with fluorescence spectra, lifetimes, intensity trajectories, and polarization modulation.[3] Our results support the picture that an APC trimer can be regarded as three pairs of two excitonic states of the strongly coupled α84 and β84 chromophores with much weaker interac-

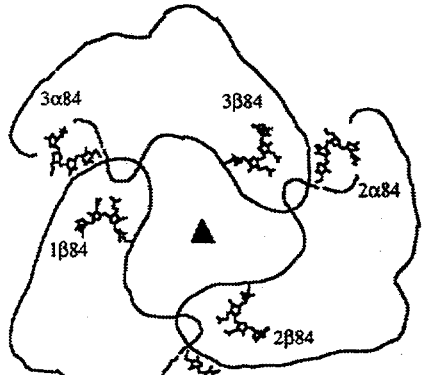

Figure 5.24. The structure of APC.

tions among the pairs. The fluorescence spectra of individual APC trimers are identical to the ensemble-averaged spectrum, and are homogeneous on the time scale of seconds. The fluorescence lifetimes, on the other hand, are found to be widely distributed, and are shorter than the ensemble-averaged lifetime because of formation of long lived exciton traps.

Polarization modulation of the excitation light can yield detailed information on the orientation of the transition dipoles. According to the C_3 symmetry of the trimer, the fluorescence intensity can be regarded as the incoherent summation of emission from three quasi-independent chromophore pairs. Assuming that the disk-like APC trimer lies flat on the glass surface, fluorescence intensity induced by excitation to the higher exciton band can be written as

$$I = P\sigma_1\eta_1\cos^2(\omega t + \theta) + P\sigma_2\eta_2\cos^2(\omega t + \theta + 2\pi/3) + P\sigma_3\eta_3\cos^2(\omega t + \theta + 4\pi/3), \quad (1)$$

where P is the laser power density; σ_1, σ_2, and σ_3 are the absorption cross-sections of the lower exciton band at the excitation wavelength; η_1, η_2, and η_3 are the fluorescence quantum yields of the three pairs, ω is the frequency of polarization modulation; and θ is the initial phase. Figure 5.25 shows a calculation of the emission intensity influenced by polarization modulation for an APC trimer laid down flat on a substrate. For three identical pairs, $\sigma_1 = \sigma_2 = \sigma_3 = \sigma$ and $\eta_1 = \eta_2 = \eta_3 = \eta$, so Eq. (1) can be simplified to

$$I = P\sigma\eta[\cos^2(\omega t + \theta) + \cos^2(\omega t + \theta + 2\pi/3) + \cos^2(\omega t + \theta + 4\pi/3)] = 1.5P\sigma\eta. \quad (2)$$

Therefore, no modulation of the fluorescence intensity should be seen (solid line in Fig. 5.25). After the formation of an exciton trap in one of the three pairs ($\eta_3 = 0$, for example), a moderate modulation should be seen (dotted line in Fig. 5.25, assuming that the trap does not quench the emission of the adjacent pairs, i.e. $\eta_1 = \eta_2 = \eta$). When emission from two pairs is gone because of either trap formation or photobleaching, emission from the remaining pair results in a 100% modulation (dashed line in Fig. 5.25).

An experimentally measured polarization modulation trace shown in Fig. 5.26. The zoomed-in figures for time periods 0–1.0 sec, 13.0–15.0 sec, and 19.0–20.0 sec correspond to three-pair, two-pair, and one-pair states, respectively, with their averaged level and modulation depth consistent with the simulations in Fig. 5.25.

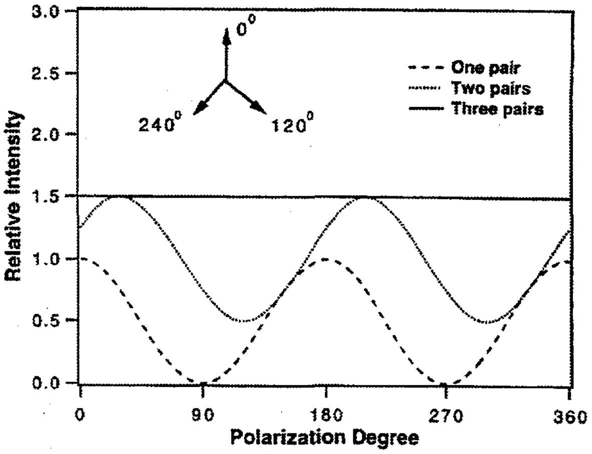

Figure 5.25. Calculated polarization modulation traces for one, two, and three pairs of α84 and β84 chromophores. The disk-like APC trimer is assumed to be flat on a flat sample surface. The polarization direction of the excitation light is rotated within the sample plane.

It is important to distinguish trap formation from photobleaching. Trap formation results in the one-step disappearance of emission within a pair, caused by formation of an absorbing radical cation, which substantially (but not completely) quenches the emission of the other chromophore in the pair. Photobleaching is caused by irreversible excited-state photochemical reactions, such as photoxidation or hydrogen abstraction, generating nonabsorbing species. The traps and bleached chromophores can be distinguished by polarization modulation traces and the simultaneous fluorescence lifetime and intensity trajectories. The portion between 5.5 and 7.5 s in Fig. 5.26 corresponds to the situation that one chromophore is photobleached. The trap formation is approximately three times more probable than the bleaching.

The exciton trap formation and/or photobleaching of an individual APC trimer is over an order of magnitude faster for pulse than for cw excitation, indicating nonlinear mechanisms for exciton trap formation and/or photobleaching. Singlet–singlet annihilation is most likely the dominating mechanism under pulsed excitation. The exciton–exciton annihilation exists even under cw excitation, as evidenced by a size-dependent bleaching rate. Singlet–triplet annihilation is most likely the

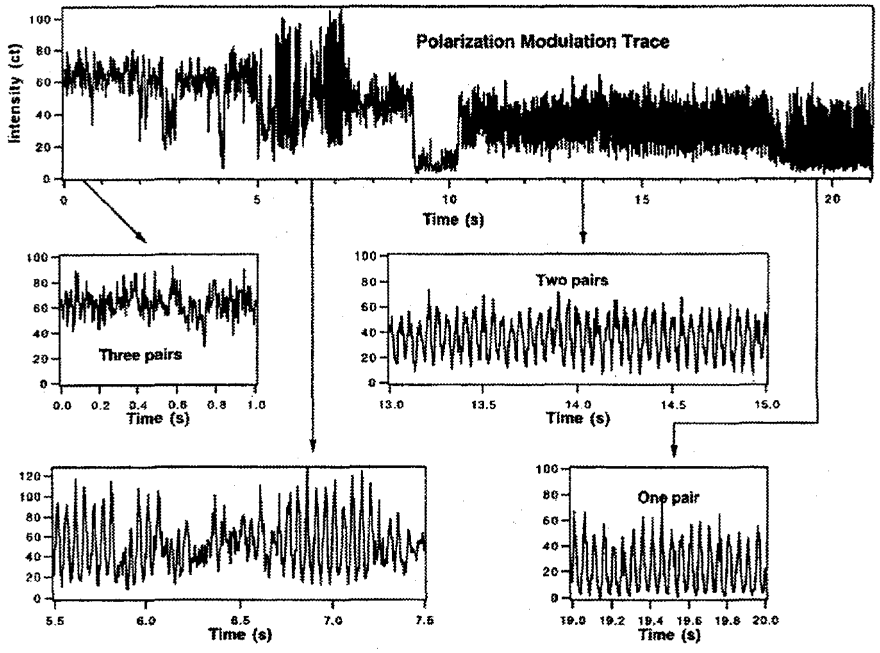

Figure 5.26. An experimentally measured polarization modulation trace. The zoomed-in portions show that the three pairs are all emitting (0.0–1.0 s) initially, then two pairs emitting (13.0–15.0 s) and finally only one pair emitting (19.0–20.0 s), similar to the calculated traces in Fig. 5.25. This experiment proves that the emission disappears in pairs due to exciton traps formed within the strong interacting α84 and β84 pairs. The portion between 5.5–7.5 s corresponds to a situation under which one of the six chromophores is bleached.

dominating mechanism under cw excitation. The exciton traps are long-lived and spontaneously reversible. Such photochemistry of light harvesting complexes is difficult to investigate with ensemble-averaged experiments, due to extremely low quantum yields for the photochemical species.

References

1. M. A. Bopp, Y. Jia, L. Li, R. J. Cogdell, and R. M. Hochstrasser, *Proc. Natl Acad. Sci.* **94,** 10630 (1997).
2. D. A. Vanden Bout, W.-T. Hip, D. Hu, D.-K. Fu, T. M. Swager, and P. F. Barbara, *Science* **277,** 1074 (1997).
3. L. Ying and S. X. Xie, *J. Phys. Chem.* B **102,** 10399 (1998).

6. Appendix

CS&D Staff

Associate Director, EMSL

Steven D. Colson

B.S. Utah State University 1963; Ph.D. California Institute of Technology 1968; Postdoctoral Fellow, National Research Council (Ottawa) 1968; Assistant Professor to Professor of Chemistry, Yale University, 1968–1989; joined PNNL as Associate Director for Chemical Structure and Dynamics June 1989. Research interests: photochemistry, photophysics, and molecular dynamics; electronic structures of molecules; processes at the molecule/surface interface.

(509) 376-4598 sd_colson@pnl.gov

Program Manager

Robin S. (Rod) McDowell

B.A. Haverford College 1956; Ph.D. M.I.T. 1960; Staff Member, Assistant Group Leader, and Laboratory Fellow, Los Alamos National Laboratory, 1960–1991; joined PNNL as Program Manager for Chemical Structure and Dynamics April 1991. Research interests: high-resolution infrared and Raman spectroscopy applied to molecular structure and bonding; molecular dynamics and force fields; statistical mechanics; infrared analytical techniques.

(509) 376-1421 rs.mcdowell@pnl.gov

Staff

Stephan E. Barlow

B.A. Southern Oregon State College 1976; Ph.D. University of Colorado 1984, Postdoctoral Fellow 1984–1989; Senior Instructor in Chemistry, University of Denver 1989–1991; joined PNNL June 1991. Research interests: development and application of mass spectrometric techniques to gas-phase chemical kinetics, reaction mechanisms, and structure.

(509) 376-9051 se_barlow@pnl.gov

James P. Cowin

B.S. Case Western Reserve University 1974; Ph.D. University of Chicago 1981; Postdoctoral Fellow, University of Toronto 1981–1983; Assistant Professor of Chemistry, University of California, Santa Barbara, 1983–1990; joined PNNL July 1990. Research interests: molecular motions at interfaces, especially energy and charge transfer, bond formation dynamics, and light-stimulated surface reactions.

(509) 376-6330 jp_cowin@pnl.gov

Robert S. Disselkamp

B.S. University of Minnesota 1985; Ph.D. Indiana University 1990; Postdoctoral Fellow, Colorado State University 1990–1993 and University of Colorado 1993–1995; Assistant Professor, University of Alaska, 1995–1998; joined PNNL 1998 on a joint appointment with EHSD Atmospheric Sciences group and CS&D. Research interests: atmospheric heterogeneous chemistry; atmospheric aerosols and clouds; optical properties of particle ensembles; remote sensing of clouds.

(509) 372-6061 robert.disselkamp@pnl.gov

Wayne P. Hess

B.A. University of Colorado 1981; M.S. University of Oregon 1983; Ph.D. University of Colorado 1988; Postdoctoral Fellow, Sandia Livermore Combustion Research Facility 1988–1990; joined PNNL January 1990. Research interests: modeling condensed phase chemistry through the study of energetic reactive processes in molecular solids and thin films (dissociation and fragmentation, electronic and vibrational energy transfer), using laser-induced desorption and ablation of adsorbed molecules and solid surfaces.

(509) 376-9907 wp_hess@pnl.gov

Gary R. Holtom

B.A. Pfeiffer College 1969; Ph.D. University of California, Berkeley, 1978; Postdoctoral Fellow, Wesleyan University 1978–1979; Head of Laser Operations, University of Pennsylvania Regional Laser and Biotechnology Laboratory, 1979–1989; joined PNNL September 1989. Research interests: short-pulse laser spectroscopy; condensed-phase photochemistry, in particular the dynamics of electronically-excited organic molecules.

(509) 376-5331 gr_holtom@pnl.gov

Stephen A. Joyce

B.S. Boston College 1982; Ph.D. M.I.T. 1987; Postdoctoral Fellow, National Institute of Standards and Technology 1987–1989; Sandia National Laboratories 1989–1991; joined PNNL October 1991. Research interests: scanning probe microscopies for studying molecularly-resolved chemistry on solid surfaces.

(509) 376-3532 sa_joyce@pnl.gov

Bruce D. Kay

B.S. University of Illinois 1976; Ph.D. University of Colorado 1982; Senior Member of the Technical Staff, Sandia National Laboratories, 1982–1991; joined PNNL November 1991. Research interests: chemical dynamics and kinetics of molecular processes occurring at the gas-surface interface; dissociative chemisorption of halogenated hydrocarbons on model oxide surfaces; quantum-resolved H-atom reactive scattering from halogenated surfaces; trapping and "solvation" of ions and molecules on multilayer ice surfaces.

(509) 376-0028 bd_kay@pnl.gov

Thomas M. Orlando

B.S. Southampton College 1982; Ph.D. State University of New York at Stony Brook 1988; Postdoctoral Fellow, Universität Basel 1988–1989, Sandia National Laboratory 1990–1991; joined PNNL September 1991. Research interests: non-thermal interfacial reaction dynamics; electron- and photon-induced surface chemistry; liquid interfaces; low-temperature plasmas; dissociative electron attachment; laser spectroscopy.

(509) 376-9420 tm_orlando@pnl.gov

Douglas Ray

B.A. Kalamazoo College 1979; Ph.D. University of California, Berkeley, 1985; Postdoctoral Fellow, Joint Institute for Laboratory Astrophysics 1985–1990; joined PNNL June 1990. Research interests: the experimental study of dynamical processes in clusters and at liquid interfaces using techniques of laser spectroscopy and mass spectrometry.

(509) 376-8069 d_ray@pnl.gov

Steven W. Sharpe

B.S. University of Bridgeport 1979; Ph.D. State University of New York at Stony Brook 1986; Postdoctoral Fellow, University of Southern California 1987–1990; joined PNNL May 1990. Research interests: high-resolution molecular spectroscopy.

(509) 376-7769 sw_sharpe@pnl.gov

Lai-Sheng Wang

B.S. Wuhan University 1982; Ph.D. University of California, Berkeley, 1989; Postdoctoral Fellow, Rice University 1990–1992; joint Washington State University/PNNL appointment January 1993. Research interests: clusters of metals, semiconductors, and insulators important as model systems for catalysis, interfaces, and surface chemistry; photoelectron spectroscopy and pulsed laser-vaporization techniques; novel gas-phase molecules involving metal atoms with oxygen, carbon, and nitrogen and the nature of M–O, M–C, and M–N chemical bonding; electrospray and solvation of singly- and multiply-charged anions.

(509) 376-8709 ls_wang@pnl.gov

Xiaoliang (Sunney) Xie

B.S. Peking University 1984; Ph.D. University of California at San Diego 1990; Postdoctoral Fellow, University of Chicago 1990–1991; joined PNNL January 1992. Research interests: single-molecule and ultrafast spectroscopy, near-field microscopy, chemical physics in biological systems.

Current address: Department of Chemistry, 12 Oxford St., Harvard University, Cambridge, Mass. 02138.

Research Scientists

Kenneth M. Beck

B.A. Northwestern University 1972; M.S. University of Illinois 1985, Ph.D. 1988; Postdoctoral Fellow University of Pennsylvania 1988–1990, PNNL 1990–1991; Asst. Professor, University of Central Florida 1991–1995; PNNL 1996; joined PNNL staff September 1996.

(509) 376-9152 kenneth.beck@pnl.gov

Thomas A. Blake

B.S. University of Bridgeport 1981; Ph.D. Wesleyan University 1989; Postdoctoral Fellow, University of Washington 1988–1991; NRC Research Associate, NASA Ames Research Center 1991–1994; joined PNNL September 1994.

(509) 376-8974 ta.blake@pnl.gov

Martin J. Iedema

B.S. University of Southern California 1988; Technician, Mt. Wilson Observatory 1987–1990; joined PNNL September 1990.

(509) 376-6039 mj_iedema@pnl.gov

Alan G. Joly

B.S. University of Rochester 1985; Ph.D. M.I.T. 1990; Postdoctoral Fellow, PNNL 1990–1993; joined PNNL staff June 1993.

(509) 376-7707 ag_joly@pnl.gov

Gregory A. Kimmel

B.S. Cornell University 1984, Ph.D. 1992; Postdoctoral Fellow PNNL, 1992–1995; joined PNNL staff September 1995.

(509) 376-2501 ga_kimmel@pnl.gov

Hong (Peter) Lu
B.A. Beijing University 1982, M.Sc. 1984; M. Phil. Columbia 1987, Ph.D. 1991; Postdoctoral Fellow, Northwestern 1991–1995; Postdoctoral Fellow, PNNL, 1995–1996; joined PNNL staff November 1996.
(509) 376-3897 hong.lu@pnl.gov

Matthew T. Sieger
B.S. University of Missouri at Rolla 1990; M.S. University of Illinois 1991, Ph.D. 1995; Postdoctoral Fellow, CS&D, with Thom Orlando, 1996–1998; joined PNNL staff October 1998.
(509) 376-9104 mt_sieger@pnl.gov

R. Scott Smith
B.S. Northern Arizona University 1983; Ph.D. University of Utah 1988; Postdoctoral Fellow, University of Arizona 1988–1989, PNNL 1990–1992; joined PNNL staff October 1992.
(509) 376-0907 rs_smith@pnl.gov

Russell G. Tonkyn
B.A. Reed College 1978; Ph.D. University of Wisconsin 1988; Postdoctoral Fellow, Brookhaven National Laboratory 1988–1991, PNNL 1991–1992; joined PNNL staff November 1992.
(509) 376-8817 rg.tonkyn@pnl.gov

Visiting Scientists

Alexandr B. Alexandrov
Ph.D. Technical University of Leningrad 1984; Senior Scientist with Research Institute of Complex Power Technology (VNIPIET), St. Petersburg 1980–1998; AWU Visiting Scientist Fellowship at PNNL with Thom Orlando, 1998– .

Carey K. Johnson
B.S., B.A. Tabor College 1973; Ph.D. Iowa State University 1981; Postdoctoral Fellow, University of Pennsylvania 1982–1984; Associate Professor of Chemistry, University of Kansas; AWU Visiting Scientist Fellowship at PNNL with Sunney Xie, June–July 1996, 1997–1998.

Nikolai G. Petrik
M.S. St. Petersburg Institute of Technology 1977, Ph.D. 1980, D.Sc. 1994; Senior Scientist with All-Russian Project and Research Institute of Complex Power Technology (VNIPIET), St. Petersburg, 1982–1998; SABIT (Special American Business Internship Training Program) appointment at PNNL with Thom Orlando, 1996; Visiting Scientist 1997– .
(509) 376-5379

Robert L. Sams
B.A. Western Washington University 1962; M.S. University of Washington 1967; National Bureau of Standards/National Institute of Standards and Technology 1967–1995; AWU Visiting Scientist Fellowship at PNNL with Steve Sharpe from December 1995.
(509) 376-8995 rl_sams@pnl.gov

Athanassios A. Tsekouras
B.S. National University of Athens 1987; Ph.D. Stanford University 1992; Postdoctoral Fellow M.I.T. 1992–1996; University of Athens 1997– ; AWU Visiting Scientist at PNNL with Jim Cowin, summers 1997, 1998.

Operations Administrator

Cynthia A. Irwin

Office Support

Jayme R. Crow
Debra M. Hinton (to Sept. 1998)
Leann Peterson
Kate Renee Ruby (COE, from Sept. 1998)

Postdoctoral Fellows

Augusta Alberico
Grad. University of Turin 1994, Ph.D. 1997; Postdoctoral Fellow, CS&D, with Jim Cowin, 1998; now at Tecnolab, Tecnoparco del Lago Maggiore S.p.A., Verbania, Italy.

David C. Arnett
Ph.D. University of Pennsylvania 1998; Postdoctoral Fellow, CS&D, with Sunney Xie, 1998- .

Michael Carpenter
B.S. State University of New York at Geneseo 1991; M.S. Rochester 1993, Ph.D. 1996; Postdoctoral Fellow, Cornell University 1996–1998; Postdoctoral Fellow, CS&D, with Jim Cowin, 1998– .

Wenwu Chen
B.S. University of Science and Technology of China 1984; M.S., Institute of Chemistry, Academia Sinica 1994; Ph.D. Technische Universität München, Germany 1997; Postdoctoral Fellow with Lai-Sheng Wang, 1998– .

Chuan-Fan Ding
B.S. University of Science and Technology of China 1984; Ph.D. Fudan University, Shanghai; Research Fellow, Institute of Chemistry, Chinese Academy of Sciences 1991–1995; Post-

doctoral Fellow with Lai-Sheng Wang, 1996–1998; now at University of Victoria, B.C.

Zdenek Dohnálek
B.S. Institute of Chemical Engineering, Prague, 1989, M.S. 1991; Ph.D. University of Pittsburgh 1997; Postdoctoral Fellow, CS&D, with Bruce Kay, 1997– .

David S. Karpovich
B.S. Saginaw Valley (Mich.) State University 1992; Ph.D. Michigan State University 1996; Postdoctoral Fellow, CS&D, with Doug Ray, 1996–1998; now at University of Wisconsin–Eau Claire.

David M. Laman
B.S. Florida International University 1986; M.S. Syracuse University 1988; Ph.D. University of Maryland 1997; Postdoctoral Fellow, CS&D, with Doug Ray, 1997– .

Lukas Novotny
Dipl.El.-Eng. Swiss Federal Institute of Technology (ETH) 1992, Dr.Sc.Nat. 1996; Postdoctoral Fellow, CS&D, with Sunney Xie, 1996– .

James Bradley Rowland
B.S. Southeastern Oklahoma State University 1990; Ph.D. Oklahoma State University 1995; Postdoctoral Fellow, CS&D, with Wayne Hess, 1996–1998; now at Battelle Dugway Operations, Dugway Proving Ground, Utah.

Matthew T. Sieger
B.S. University of Missouri at Rolla 1990; M.S. University of Illinois 1991, Ph.D. 1995; Postdoctoral Fellow, CS&D, with Thom Orlando, 1996–1998; now Associate Scientist on permanent staff.

William C. Simpson
B.S. Willamette University 1990; Ohio State University 1990–1991; M.S. University of California, Riverside, 1992, Ph.D. 1995; Postdoctoral Fellow, CS&D, with Thom Orlando, 1996–1998; now at Bankers Systems, St. Cloud, Minn.

Kip Stevenson
B.S. University of Puget Sound 1989; Ph.D. University of Washington 1997; Postdoctoral Fellow, CS&D, with Bruce Kay, 1997– .

Mark D. Tinkle
B.S. California Institute of Technology 1984; M.S. California State University, Fullerton 1987; M.S. University of California, San Diego 1989, Ph.D. 1994; Postdoctoral Fellow, CS&D, with Steve Barlow, 1996–1998.

Xue-Bin Wang
B.S. University of Science and Technology of China 1988; Ph.D. Institute of Chemistry, Chinese Academy of Sciences 1995; Postdoctoral Fellow Columbia 1995–1996; Postdoctoral Fellow, CS&D, with Lai-Sheng Wang, 1997–1998.

Richard M. Williams
B.S. University of Idaho 1991; Ph.D. University of Colorado/JILA, 1997; Postdoctoral Fellow, CS&D, with Wayne Hess, 1997–1998; now Postdoctoral Fellow with PNNL Energy Division.

Kai Wu
B.S. Zhejiang University, Hangzhou, 1987; Ph.D. Dalian Institute of Chemical Physics, Chinese Academy of Sciences, 1991; Research Associate, State Key Laboratory of Catalysis, Dalian Institute, 1992–1995; Fritz-Haber-Institut, Max Planck Gesellschaft, Berlin, 1996–1998; Postdoctoral Fellow, CS&D, with Jim Cowin, 1998– .

Andreas Zumbusch
Ph.D. University of Karlsruhe 1996; Postdoctoral Fellow, CS&D, with Sunney Xie, 1996–1998; now at Institut für Physikalische Chemie, Ludwig-Maximilians Universität München, Munich.

Graduate Students

Nick Boivin
Princeton University, working with Wayne Hess, 1998– .

Kimberly Briggman
Northwestern University, working with Thom Orlando, 1998.

Sherry Lin
Washington State University, working with Lai-Sheng Wang, 1998– .

Sreela Nandi
University of Colorado, working with Wayne Hess, 1997–

Erik J. Sánchez
Portland State University, working with Sunney Xie, 1995– .

Paul R. Winter
University of Colorado, working with Wayne Hess, 1997– .

Liming Ying
Peking University, working with Sunney Xie, 1998; Ph.D., Peking University, 1998.

Undergraduate Students

Ryan Ciolli
University of Oklahoma, working with Bruce Kay, 1998.

Chris J. Fuller
University of Washington, working with Wayne Hess, 1997–1998.

Christian D. Howd
University of Michigan, working with Rob Disselkamp, 1998.

Publications and Presentations

Publications

C. C. Ainsworth, D. M. Friedrich, P. L. Gassman, Z. Wang, and A. G. Joly, "Characterization of Salicylate–Alumina Surface Complexes by Polarized Fluorescence Spectroscopy," *Geochim. Cosmochim. Acta* **62**, 595–612 (1998).

M. L. Balmer, R. G. Tonkyn, A. Y. Kim, J. Hoard, I. S. Yoon, D. Jimenez, T. M. Orlando, S. E. Barlow, "Diesel NO_x Reduction on Surfaces in Plasma," *Soc. Automot. Eng. Proc. on Emissions Control (1998); SAE Paper* 982511. (USCAR CRADA)

K. M. Beck and W. P. Hess, "Quantum-State Resolved Products via Vacuum Ultraviolet Photostimulated Desorption from Geologic Calcite," *Appl. Surf. Sci.* **127–129**, 21–25 (1998). (BES)

K. M. Beck, T. Sasaki, and N. Koshizaki, "Preparation of Pt/TiO_2 Nanocomposite Materials via Laser Ablation of Bi-Combinant Targets," *Chem. Phys. Lett.* **301**, 336–342 (1999). (NSF, BES)

J. P. Biesecker, G. B. Ellison, H. Wang, M. J. Iedema, A. A. Tsekouras, and J. P. Cowin, "Ion Beam Source for Soft-Landing Deposition," *Rev. Sci. Instr.* **69**, 485–495 (1998). (BES)

C.-F. Ding, X.-B. Wang, and L.-S. Wang, "Photoelectron Spectroscopy of Doubly Charged Anions: Intramolecular Coulomb Repulsion and Solvent Stabilization," *J. Phys. Chem. A* **102**, 8633–8636 (1998). (BES)

D. M. Friedrich, Z. Wang, C. C. Ainsworth, P. L. Gassman, and A. G. Joly, "Effect of Leaving Group Lability on Kinetics of Organic Anion Sorption at Aqueous Mineral Interfaces," Extended Abstracts, Symposium on Humic Substance–Mediated Environmental Reactions, ACS Division of Environmental Chemistry (216th American Chemical Society National Meeting, Boston, Aug. 23–27, 1998) 38:63–65 (American Chemical Society, Washington, D.C., 1998).

B. Hecht, H. Bielefeld, D. W. Pohl, L. Novotny, and H. Heinzelmann, "Influence of Detection Conditions on Near-Field Optical Imaging," *J. Appl. Phys.* **84**, 5873–5882 (1998).

M. A. Henderson and S. A. Joyce, "Interaction of Water with the (1*x*1) and (2*x*1) Surfaces of α-$Fe_2O_3(012)$," *Surf. Sci.* **417**, 66–81 (1998). (LDRD)

W. P. Hess, S. Deshmukh, B. Rowland, P. R. Winter, and G. B. Ellison, "The Gas and Condensed Phase Ultraviolet Photochemistry of Organic Acid Chlorides," *Recent Res. Devel. in Photochem. & Photobiol.* **1**, 277–290 (1997). (BES)

W. P. Hess, H. K. Park, O. Yavas, and R. F. Haglund Jr., "IR-MALDI of Low Molecular Weight Compounds Using a Free Electron Laser," *Appl. Surf. Sci.* **127–129**, 235–241 (1998). (BES)

M. J. Iedema, M. J. Dresser, D. L. Doering, J. B. Rowland, W. P. Hess, A. A. Tsekouras, and J. P. Cowin, "Ferroelectricity in Water Ice," *J. Phys. Chem. B* **102**, 9203–9214 (1998). (BES)

M. J. Iedema, N. Kizhakevariam, and J. P. Cowin, "Mixed Oxide Surfaces: Ultrathin Films of $Ca_xMg_{(1-x)}O$," *J. Phys. Chem B* **102**, 693–700 (1998). (BES)

D. S. Karpovich and D. Ray, "Adsorption of Dimethyl Sulfoxide to the Liquid/Vapor Interface of Water and the Thermochemistry of Transport across the Interface," *J. Phys. Chem. B* **102**, 649–652 (1998). (BES)

K. Knutsen and T. M. Orlando, "Low-Energy (5–100 eV) Electron- and Ultraviolet (6.4 eV) Photon-Stimulated Degradation of Neutral Fragments from $NaNO_3$ Single Crystals," *Appl. Surf. Sci.* **127–129**, 1–6 (1998). (BES)

X. Li and L.-S. Wang, "The Chemical Bonding and Electronic Structure of RhC, RhN, and RhO by Anion Photoelectron Spectroscopy," *J. Chem. Phys.* **109**, 5264–5268 (1998). (NSF)

X. Li, H. Wu, X.-B. Wang, and L.-S. Wang, "*s-p* Hybridization and Electron Shell Structures in Aluminum Clusters: A Photoelectron Spectroscopy Study," *Phys. Rev. Lett.* **81**, 1909–1912 (1998). (NSF)

H. P. Lu, L. Xun, and X. S. Xie, "Single-Molecule Enzymatic Dynamics," *Science* **282**, 1877–1882 (1998). (BES, NABIR)

R. McDowell, "Spectroscopy and Detection Techniques for Laser Remote Sensing," *Arms Control and Nonproliferation Technologies* (DOE Office of Nonproliferation and National Security), Third/Fourth Quarters 1996 (actually publ. 1998), pp. 24–25. (NN-20)

M. B. More, D. Ray, and P. B. Armentrout, "Intrinsic Affinities of Alkali Cations for 15-Crown-5 and 18-Crown-6: Bond Dissociation Energies of

Gas-Phase M^+–Crown Ether Complexes," *J. Am. Chem. Soc.* **121**, 417–423 (1999). (BES)

L. Novotny, B. Hecht, and D. W. Pohl, "Implications of High Resolution to Near-Field Optical Microscopy," *Ultramicroscopy* **71**, 341–344 (1998).

L. Novotny, E. J. Sánchez, and X. S. Xie, "Near-Field Optical Imaging Using Metal Tips Illuminated by Higher-Order Hermite–Gaussian Beams," *Ultramicroscopy* **71**, 21–29 (1998). (BES)

L. Novotny, E. J. Sánchez, and X. S. Xie, "Optical Microscopy and Spectroscopy Beyond the Diffraction Limit," *Proc. SPIE* **3273**, 194–202 (1998). (BES)

R. L. Sams, T. A. Blake, S. W. Sharpe, J.-M. Flaud, and W. J. Lafferty, "High-Resolution Infrared Study of the ν_{14}, ν_{17}, and ν_{18} Bands of $^{11}B_2H_6$ and $^{10}B^{11}BH_6$," *J. Mol. Spectrosc.* **191**, 331–342 (1998). (EMSL Operations)

S. W. Sharpe, J. F. Kelly, J. S. Hartman, C. Gmachl, F. Capasso, D. L. Sivco, J. N. Baillargeon, and A. Y. Cho, "High-Resolution (Doppler-Limited) Spectroscopy Using Quantum-Cascade Distributed-Feedback Lasers," *Opt. Lett.* **23**, 1396–1398 (1998). (DOE, EMSL Operations)

M. T. Sieger, W. C. Simpson, and T. M. Orlando, "Production of O_2 on Icy Satellites by Electronic Excitation of Low-Temperature Water Ice," *Nature* **394**, 554–556 (1998). (BES)

W. C. Simpson, T. M. Orlando, L. Parenteau, K. Nagesha, and L. Sanche, "Dissociative Electron Attachment in Nanoscale Ice Films: Thickness and Charge Trapping Effects," *J. Chem. Phys.* **108**, 5027–5034 (1998). (BES)

D. P. Taylor, W. C. Simpson, K. Knutsen, M. A. Henderson, and T. M. Orlando, "Photon Stimulated Desorption of Cations from Yttria-Stabilized Cubic $ZrO_2(100)$," *Appl. Surf. Sci.* **127–129**, 101–104 (1998). (LDRD)

R. G. Tonkyn, M. Balmer, S. Barlow, T. M. Orlando, J. Hoard, and D. Goulette, "Vehicle Exhaust Treatment Using Electrical Discharge and Materials Chemistry," *Proc. 1997 Diesel Exhaust Reductions Workshop; SAE Paper* 971716 (1998). (USCAR CRADA)

A. A. Tsekouras, M. J. Iedema, and J. P. Cowin, "Amorphous Water-Ice Relaxations Measured with Soft-Landed Ions," *Phys. Rev. Lett.* **80**, 5798–5801 (1998). (BES)

A. A. Tsekouras, M. J. Iedema, G. B. Ellison, and J. P. Cowin, "Soft-Landed Ions: A Route to Ionic Solution Studies," *J. Mass Spectrom. Ion Processes* **174**, 219–230 (1998). (BES, SERDP)

L.-S. Wang, C.-F. Ding, X.-B. Wang, and J. B. Nicholas, "Probing the Potential Barriers and Intramolecular Electrostatic Interactions in Free Doubly Charged Anions," *Phys. Rev. Lett.* **81**, 2667–2670 (1998). (BES)

L.-S. Wang, X.-B. Wang, H. Wu, and H. Cheng, "New Magic Numbers in $Ti_xC_y^-$ Anion Clusters and Implications for the Growth Mechanisms of Titanium Carbide Clusters," *J. Am. Chem. Soc.* **120**, 6556–6562 (1998). (NSF)

L.-S. Wang and H. Wu, "Photoelectron Spectroscopy of Transition Metal Clusters," *Z. Phys. Chem.* **203**, 45–55 (1998). (NSF)

X.-B. Wang, C.-F. Ding, and L.-S. Wang, "Photodetachment Spectroscopy of a Doubly-Charged Anion: Direct Observation of the Repulsive Coulomb Barrier," *Phys. Rev. Lett.* **81**, 3351–3354 (1998). (NSF)

P. R. Winter, B. Rowland, W. P. Hess, J. G. Radziszewski, M. R. Nimlos, and G. B. Ellison, "The UV Photodissociation of Matrix Isolated Propionyl Chloride," *J. Phys. Chem. A* **102**, 3238–3248 (1998). (BES)

H. Wu, X. Li, X.-B. Wang, C.-F. Ding, and L.-S. Wang, "Al_3O_y (y = 0–5) Clusters: Sequential Oxidation, Metal-to-Oxide Transformation, and Photoisomerization," *J. Chem. Phys.* **109**, 449–458 (1998). (BES)

H. Wu and L.-S. Wang, "A Photoelectron Spectroscopic Study of Monovanadium Oxide Anions: VO_x^- (x = 1–4)," *J. Chem. Phys.* **108**, 5310–5318 (1998). (NSF)

H. Wu and L.-S. Wang, "Photoelectron Spectroscopy and Electronic Structure of ScO_n^- (n = 1–4) and YO_n^- (n = 1–5): Strong Electron Correlation Effects in ScO^- and YO^-," *J. Phys. Chem.* **102**, 9129–9135 (1998). (NSF)

X. S. Xie and J. K. Trautman, "Optical Studies of Single Molecules at Room Temperature," *Ann. Rev. Phys. Chem.* **49**, 441–480 (1998). (BES)

L. Ying and X. S. Xie, "Fluorescence Spectroscopy, Exciton Dynamics and Photochemistry of Single Allophycocyanin Trimers," *J. Phys. Chem.* **102**, 10399–10409 (1998). (BES)

In Press and Submitted

A. Al-Kahtani, D. L. Williams, J. W. Nibler, and S. W. Sharpe, "High Resolution Infrared Studies of $Al(BH_4)_3$ and $Al(BD_4)_3$," *J. Chem. Phys.*, submitted. (BES)

H. Bahnmaier, A. G. Joly, J. M. Price, and D. Ray, "Rotational Coherence Spectroscopy of Mass-Selected Fluorene–Ar Heterodimers by Time-Resolved Ionization Depletion," *Chem. Phys. Lett.*, submitted. (BES)

M. L. Balmer, R. Tonkyn, A.Y. Kim, J. Hoard, I. S. Yoon, D. Jimenez, T. M. Orlando, and S. Barlow, "Nitrogen Measurement from NO_x Reduction for a Plasma-Catalyst System in Simulated Diesel Exhaust," *Proc. 1998 Diesel Engine Emissions Reduction Workshop*, in press. (USCAR CRADA)

M. L. Balmer, R. G. Tonkyn, I. Yoon, S. Barlow, T. Orlando, and J. Hoard, "Surface Mediation of NOx Reduction/Oxidation in a Plasma," *Proc. Mat. Res. Soc.*, submitted. (USCAR CRADA)

S. E. Barlow and M. L. Alexander, "Demonstration of the Asymmetric Ion Trap," *J. Amer. Soc. Mass Spectrom.*, submitted. (BES)

A. I. Boldyrev, J. Simons, X. Li, W. Chen, and L.-S. Wang, "A Combined Photoelectron Spectroscopy and Ab Initio Study of the Hypermetallic Al_3C Molecule," *J. Chem. Phys.*, submitted.

S. A. Chambers and S. A. Joyce, "Surface Termination, Composition, and Reconstruction of Fe_3O_4 (001) and γ-Fe_2O_3(001)," *Surf. Sci.*, in press. (EMSP)

W. Chen, X. Li, S. S. Liu, and L.-S. Wang, "The Electronic Structure of MoC and WC by Anion Photoelectron Spectroscopy," *J. Chem. Phys.*, submitted. (NSF)

H. S. Cheng and L.-S. Wang, "Quantum Mechanical Modeling of Structure Evolution of Transition Metal Clusters and Metallocarbohedrenes," *NATO Conference Series*, in press.

S. D. Colson, R. E. Gephart, V. L. Hunter, J. Janata, and L. G. Morgan, "A Risk and Outcome Based Strategy for Justifying Characterization to Resolve Tank Waste," in *Science and Technology for Disposal of Radioactive Tank Wastes* (Plenum Publishing, New York), in press.

J. P. Cowin, A. A. Tsekouras, M. J. Iedema, K. Wu, and G. B. Ellison, "Immobility of Protons in Ice from 30 to 190 K," *Nature*, in press. (BES)

C.-F. Ding, X.-B. Wang, and L.-S. Wang, "Photodetachment Photoelectron Spectroscopy of Doubly-Charged Anions: $S_2O_8^{2-}$," *J. Chem. Phys.* **110**, xxx–xxx (1999). (BES)

Z. Dohnálek, R. L. Ciolli, G. A. Kimmel, K. P. Stevenson, R. S. Smith, and B. D. Kay, "Substrate Induced Crystallization of Amorphous Solid Water at Low Temperatures," *J. Chem. Phys.*, in press. (BES)

D. M. Friedrich, Z. Wang, A. G. Joly, K. A. Peterson and P. R. Callis, "The Ground State Proton-Transfer Tautomer of Salicylate Anion," *J. Phys. Chem.*, submitted.

M. C. Gallagher, M. S. Fyfield, and S. A. Joyce, "Structural Transformations in the Stranski-Krastanov Growth of Mg on Mo(001)," *Phys. Rev. B*, in press. (BES Materials Sciences)

M. V. Gorshkov, J. A. Mack, S. E. Barlow, D. Ray, and J. M. Price, "Frequency-Sweep Radiofrequency Ion Trap Mass Spectrometry," *J. Am. Soc. Mass. Spectrom.*, submitted. (BES, LDRD)

L. M. Goss, S. W. Sharpe, T. A. Blake, V. Vaida, and J. W. Brault, "Direct Absorption Spectroscopy of Water Clusters," *J. Phys. Chem.*, submitted. (ARM)

G. S. Herman, E. P. McDaniel, and S. A. Joyce, "Interaction of D_2O with the Fe_3O_4(111) and the Biphase Ordered Structures on α-Fe_2O_3," *J. Electron. Spect. Related Phenomena*, in press. (LDRD)

Th. Huser, L. Novotny, Th. Lacoste, R. Eckert, and H. Heinzelmann, "Observation and Analysis of Near-Field Optical Diffraction," *J. Opt. Soc. Am. A*, submitted.

R. S. McDowell and J. F. Kelly, "Spectroscopy, Optical," *The Concise Encyclopedia of Chemical Technology*, J. I. Kroschwitz, ed. (John Wiley & Sons, New York, 1998), in press. (BES)

S. K. Nayak, B. K. Rao, P. Jena, X. Li, and L.-S. Wang, "Observation of a Spin-Protected High Energy Isomer of Al_4N^- Cluster," *Chem. Phys. Lett.*, in press.

C. H. F. Peden, G. S. Herman, I. Z. Ismagilov, B. D. Kay, M. A. Henderson, Y. J. Kim, and S. A. Chambers, "Model Catalyst Studies with Single Crystals and Epitaxial Thin Oxide Films," *Catalysis Today*, submitted. (BES)

N. G. Petrik, D. P. Taylor, and T. M. Orlando, "Laser-Stimulated Luminescence of Yttria-Stabilized Cubic Zirconia Crystals," *J. Appl. Phys.*, submitted. (EMSP)

N. G. Petrik, D. P. Taylor, W. C. Simpson, and T. M. Orlando, "Laser-Stimulated Luminescence Studies of ZrO_2(100) and (110) Single Crystals," *J. Appl. Phys.*, in press. (BES).

B. Rowland, P. R. Winter, G. B. Ellison, J. G. Radziszewski, and W. P. Hess, "Photochemistry of Matrix Isolated and Thin Film Acid Chlorides: Quantum Yields and Product Structures," *J. Phys. Chem.*, in press. (BES)

E. J. Sánchez, L. Novotny, and X. S. Xie, "Near-Field Fluorescence Microscopy Based on Two-Photon Excitation with Metal Tips," *Phys. Rev. Lett.*, submitted. (BES)

M. T. Sieger and T. M. Orlando, "Low-Temperature Water Ice Phases Probed by Electron-Stimulated Desorption," *Surf. Sci.*, submitted. (BES)

M. T. Sieger, G. K. Schenter, and T. M. Orlando, "Stimulated Desorption by Surface Electron Standing Waves," *Phys. Rev. Lett.*, submitted. (BES)

W. C. Simpson, W. K. Wang, J. A. Yarmoff, and T. M. Orlando, "Photon- and Electron-Stimulated Desorption of O^+ from Zirconia," *Surf. Sci.*, in press. (BES)

R. S. Smith and B. D. Kay, "Evidence for the Existence of Supercooled Water at 150 K," *Nature*, in press. (BES)

K. P. Stevenson, G. A. Kimmel, Z. Dohnálek, R. S. Smith, and B. D. Kay, "Controlling the Morphology of Laboratory Analogs of Astrophysical Amorphous Ice," *Science*, in press. (BES)

S. C. Stone, L. A. Philips, G. T. Fraser, F. J. Lovas, L.-H. Xu, and S. W. Sharpe, "High-Resolution Microwave and Infrared Molecular Beam Studies of the Conformers of 1,1,2,2-Tetrafluoroethane," *J. Mol. Spectrosc.*, submitted. (BES)

M. D. Tinkle and S. E. Barlow, "Improved Measurement of Radiative Association of Cs^+ with 12-Crown-4 at 288±2 K," *Rapid Commun. Mass. Spectrom.*, submitted. (BES)

L.-S. Wang, "Photodetachment and Photoelectron Spectroscopy of Transition Metal Oxide Species," *Advanced Series in Physical Chemistry* **10**, in press. (BES, NSF)

L.-S. Wang, C.-F. Ding, X.-B. Wang, and S. E. Barlow, "Photodetachment Photoelectron Spectroscopy of Multiply Charged Anions Using Electrospray Ionization" *Rev. Sci. Instr.*, in press. (BES)

X.-B. Wang, C.-F. Ding, J. B. Nicholas, D. A. Dixon, and L.-S. Wang, "Investigation of Free Singly and Doubly Charged Alkali Metal–Sulfate Ion Pairs: $M^+(SO_4^{2-})$ and $[M^+(SO_4^{2-})]_2$ (M = Na, K)," *J. Phys. Chem. A*, submitted. (BES)

X.-B. Wang, C.-F. Ding, and L.-S. Wang, "Electron Tunneling through the Repulsive Coulomb Barrier in Photodetachment of Multiply Charged Anions," *Phys. Rev. Lett.*, submitted. (BES)

X.-B. Wang, C.-F. Ding, and L.-S. Wang, "High Resolution Photoelectron Spectroscopy of C_{60}^-: Inelastic Loss and Thermionic Emission," *J. Chem. Phys.*, submitted. (NSF)

X.-B. Wang, C.-F. Ding, L.-S. Wang, A. I. Boldyrev, and J. Simons, "First Experimental Photoelectron Spectra of Superhalogens and Their Theoretical Interpretations," *J. Chem. Phys.* **110**, xxx–xxx. (BES)

X.-B. Wang and L.-S. Wang, "Photodetachment of Benzenedicarboxylate Dianions and Solvent Complexes in the Gas Phase: Probing the Effect of Charge Delocalization and Intramolecular Coulomb Repulsion," *J. Am. Chem. Soc.*, submitted. (BES)

Z. Wang, C. C. Ainsworth, D. M. Friedrich, P. L. Gassman, and A. G. Joly, "Kinetics and Mechanism of Surface Reaction of Salicylate on Alumina in Colloidal Aqueous Suspension," *Geochim. Cosmochim. Acta*, submitted.

R. M. Williams, K. M. Beck, A. G. Joly, J. T. Dickinson, and W. P. Hess, "Pulse-Width Influence on Laser Induced Desorption from Ionic Solids," *Proc. SPIE*, in press. (BES)

K. Wu, M. J. Iedema, A. A. Tsekouras, and J. P. Cowin, "Probing Aqueous–Organic Interfaces with Soft-Landed Ions," *Nucl. Instrum. Meth. Phys. Res. B*, submitted. (BES)

X. S. Xie and H. P. Lu, "Single-Molecule Enzymology," *J. Biol. Chem.*, in press. (BES, NABIR)

A. Zumbusch, G. R. Holtom, and X. S. Xie, "Three Dimensional Vibrational Imaging by Coherent Anti-Stokes Raman Microscopy," *Phys. Rev. Lett.*, submitted. (EMSL Operations; von Humboldt Foundation)

Patents

M. L. Balmer, R. G. Tonkyn, A. Y. Kim, D. Jimenez, T. M. Orlando, and S. E. Barlow, "Materials for NOx Reduction in Conjunction with a Non-Thermal Plasma, invention disclosure filed Sept. 1998.

S. E. Barlow, T. M. Orlando, and R. G. Tonkyn, "Design for Monolithic Dielectric Packing Discharge Reactor," patent pending. (USCAR CRADA)

S. E. Barlow, R. G. Tonkyn, and T. M Orlando, "Method and Apparatus for Processing Exhaust Gas with Corona Discharge," patent pending. (USCAR CRADA)

K. M. Beck, "Photoacoustic Touch-Off Probe," U.S. Patent 5,739,433 (granted April 14, 1998).

G. R. Holtom, X. S. Xie, and A. Zumbusch, "Microscopic Imaging by CARS," application submitted July 1998. (BES)

A. J. Peurrung and S. E. Barlow, "Confinement of Weakly Ionized Gas in the Presence of a Neutral Gas," patent pending.

Presentations

*Presenter underlined; * = invited talk.*

K. M. Beck, "Atomic and Molecular Laser-Stimulated Desorption from Complex Ionic Crystals," Department of Chemistry, University of Illinois at Chicago, Feb. 12, 1998.*

K. M. Beck, "Photostimulated Desorption from Molecular Ionic Crystals," First International Symposium on Photoreaction Control and Photofunctional Materials, Tsukuba, Japan, Mar. 16–18, 1998.* (NSF, BES)

K. M. Beck, "Laser-Stimulated Energetics in Mineral Substrates," University of Tokyo Dept. of Chemical Systems Engineering, Apr. 23, 1998.* (NSF, BES)

K. M. Beck, "Atomic and Molecular Laser-Stimulated Desorption from Complex Ionic Crystals," National Institute of Materials and Chemical Research, Tsukuba, Japan, May 3, 1998.* (NSF, BES)

K. M. Beck, "Characterization of Geologic Mineral and Crystal Substrates via LAMS, XPS, EXAFS, and Microprobe Techniques," Jet Propulsion Laboratory, Pasadena, Cal., Oct. 16, 1998.* (BES)

K. M. Beck, W. P. Hess, S. M. Heald, D. L. Blanchard, and M. I. McCarthy, "An Initial EXAFS and Microprobe Study of Pb and Co Uptake by Calcite and Columbia River Caliche," Ninth Users' Meeting for the Advanced Photon Source, Argonne, Ill., Oct. 13–15, 1998. (LDRD)

K. M. Beck, T. Sasaki, and N. Koshizaki, "Preparation of Pt/TiO_2 Nanocomposite Materials by Laser Ablation of Bi-Combinant Targets," Gordon Research Conference on Laser Interactions with Materials, Andover, N.H., June 7–12, 1998. (BES)

T. A. Blake and S. W. Sharpe, "Jet Spectroscopy of the $2\nu_8$ Band of Hydrogen Fluoride Trimer in the 750 cm^{-1} Region," Fifty-third Ohio State University International Symposium on Molecular Spectroscopy, Columbus, June 15–19, 1998. (BES)

S. A. Chambers, S. Thevuthasan, Y. J. Kim, S. A. Joyce, and Y. Liang, "Surface Structure Determination of MBE Grown Iron and Manganese Oxides," 216th American Chemical Society National Meeting, Boston, Aug. 23–27, 1998.* (EMSP)

J. P. Cowin, "Soft Landing of Ions to Re-Create Electrochemical Double Layers in UHV," Gordon Research Conference on Electrochemistry, Ventura, Cal., Jan. 18–23, 1998.* (BES)

J. P. Cowin, "Ferroelectric Ices, and Soft-Landed Ion Studies of Water Ice," Surface Science Symposium, University of California, Berkeley, Feb. 5, 1998.* (BES)

J. P. Cowin, "Transport of H-Bonding Defects and Ions in Ices," SORIS (Structure of Oxygen Radicals in Irradiated Solids) 98 Workshop, Nieboro, Poland, May 30 – June 3, 1998.* (BES)

J. P. Cowin, "Spent Nuclear Fuel Materials: Issues of Radiolysis," European Institute for Transuranic Elements, Karlsruhe, Germany, June 4, 1998.* (BES)

J. P. Cowin, C. M. Berkowitz, R. S. Disselkamp, and C. C. Spicer, "Aerosol Chemistry in the Nighttime Boundary Layer," Atmospheric Chemistry Program, Falls Church, Va., Feb. 24–27, 1998 (poster).

J. P. Cowin, T. M. Orlando, T. E. Madey, P. E. Haustein, S. C. Marschman, and J. Yarmoff, "Radiolytic and Thermal Processes Relevant to Storage of Spent Nuclear Fuels," DOE Environmental Management Science Program, Chicago, July 27–30, 1998 (poster). (EMSP)

J. P. Cowin and A. A. Tsekouras, "Electrochemistry in vacuo: Ion Studies on Thin Ice Films," Department of Chemistry, University of Athens, Apr. 27, 1998.* (BES)

J. P. Cowin and A. A. Tsekouris, "Studies of Thin Ice Films with Low-Energy ions," IESL Seminar, University of Athens, June 15, 1998.* (BES)

J. P. Cowin, A. A. Tsekouras, and M. J. Iedema, "UHV Water–Solid Interfaces with Soft-Landed Ions," 215th American Chemical Society National Meeting, Dallas, Mar. 29 – Apr. 2, 1998.* (BES)

J. L. Daschbach, M. J. Stirniman, R. S. Smith, S. A. Joyce, and B. D. Kay, "Kinetics of Water Adsorption, Desorption, and Hydroxylation on MgO(100)," 215th American Chemical Society National Meeting, Dallas, Symposium on Interfacial Water, Mar. 29, 1998.* (BES)

C.-F. Ding, X. Wang, and L.-S. Wang, "Photoelectron Spectroscopy of Multiply Charged Anions," 216th American Chemical Society National Meeting, Boston, Aug. 23–27, 1998. (BES)

Z. Dohnalek, G. A. Kimmel, K. P. Stevenson, R. S. Smith and B. D. Kay "The Crystallization Kinetics of Amorphous Solid Water," 45th International Meeting of the American Vacuum Society, Baltimore, Nov. 2–6, 1998. (BES)

Z. Dohnalek, K. P. Stevenson, G. A. Kimmel, R. S. Smith, and B. D. Kay, "The Crystallization Kinetics of Amorphous Solid Water," Surface Analysis '98 (20th Symposium on Applied Surface Analysis and 10th Annual Symposium of the Pacific Northwest Chapter, American Vacuum Society), Richland, Wash., June 16–19, 1998. (BES)

M. A. Henderson, S. A. Joyce, and J. R. Rustad, "Probing the Effect of Surface Reduction on the Structure and Chemistry of Hematite Surfaces," 216th American Chemical Society National Meeting, Boston, Aug. 23–27, 1998.* (LDRD)

G. R. Holtom, A. Zumbusch, and X. S. Xie, "Imaging by Nonlinear Spectroscopy," Gordon Conference on Vibrational Spectroscopy and Molecular Dynamics, Plymouth, N.H., July 27, 1998.* (EMSL Operations)

B. D. Kay, "Beam Studies of Adsorption, Desorption, Diffusion, and Phase Transformation Kinetics," Chemical Engineering Seminar, University of Washington, Jan. 12, 1998.* (BES)

B. D. Kay, "Opportunities for Collaborative Research in Environmental Molecular Science at Pacific Northwest National Laboratory," First Annual UCSD Environmental Chemistry Meeting, University of California at San Diego, La Jolla, Apr. 25, 1998.* (BES)

B. D. Kay, "Thermodynamics and Kinetics of Nanoscale Films of Amorphous Water Ice," Surface Science Seminar, National Institute of Standards and Technology, Gaitherburg, Md., May 4, 1998.* (BES)

B. D. Kay, "Beam Studies of Kinetic Processes in Nanoscale Films of Amorphous Ice," Gordon Conference on Atomic and Molecular Interactions, New London, N.H., June 28 – July 3, 1998.* (BES)

B. D. Kay, "Beam Studies of Kinetic Processes in Nanoscale Films of Amorphous Ice," Ice Physics and Chemistry and the Environment Workshop, Richland Wash., Aug. 13–14, 1998.* (BES)

B. D. Kay, "Thermodynamic Continuity and Mobility in Amorphous Solid Water: Evidence for the Existence of Supercooled Liquid Water at 150 K," Gordon Conference on Water and Aqueous Solutions, Holderness, N.H., Aug. 26, 1998.* (BES)

B. D. Kay, "Beam Studies of Kinetic Processes in Nanoscale Films of Amorphous Ice," Geophysical Seminar, Air Force Research Laboratory, Hanscom Air Force Base, Mass., Nov. 9, 1998. * (BES)

B. D. Kay, "Beam Studies of Kinetic Processes in Nanoscale Films of Amorphous Ice," Chemistry Department Seminar, Tufts University, Medford, Mass., Nov. 10, 1998. * (BES)

B. D. Kay, "Beam Studies of Kinetic Processes in Nanoscale Films of Amorphous Ice," Physical Chemistry Seminar, Boston University, Nov. 11, 1998. * (BES)

B. D. Kay and G. A. Kimmel, "Beam Studies of Kinetic Processes in Nanoscale Films of Amorphous Ice," Space Science Seminar, Johns Hopkins Applied Physics Laboratory, Baltimore, Nov. 2, 1998.* (BES)

Y. Liang, J. Daschbach, A. Joly, D. Baer, M. Na, and H. Luo, "Enhancement of Catalytic Properties Using Surface and Interface Engineering," Materials Research Society, Boston, Dec. 1998.

H. P. Lu, "Single-Molecule Enzymatic Dynamics: Static Disorder and Dynamic Disorder," University of Kansas, Lawrence, Sept. 1998. (BES)

H. P. Lu and X. S. Xie, "Single-Molecule Spectroscopy Studies of Molecular Dynamics in Chemical and Biological Systems," 12th International Conference on Photochemical Conversion and Storage of Solar Energy, Berlin, Aug. 1998. (BES)

H. P. Lu, L. Xun, and X. S. Xie, "Probing Dynamics of Single Enzyme Molecules," 42nd American Biophysical Society Annual Meeting, Kansas City, Mo., Feb. 1998. (BES)

R. S. McDowell, J. E. Bertie, P. R. Bunker, J. K. G. Watson, J.-M. H. Flaud, J. T. Hougen, P. Rosmus, and B. P. Winnewisser, "IUPAC Recommendations for Notations and Conventions in Vibrational-Rotational Spectroscopy," Fifty-third Ohio State University International Symposium on Molecular Spectroscopy, Columbus, June 15–19, 1998.

L. Novotny, "Optical Microscopy and Spectroscopy Beyond the Diffraction Limit," SPIE Conference on Laser Techniques for Condensed Phase and Biological Systems, San Jose, Cal., Jan. 1998.

L. Novotny, "Optical Spectroscopy and Trapping Beyond the Diffraction Limit," Pacific Northwest National Laboratory, Richland, Wash., Feb. 10, 1998. (M. T. Thomas Award for Oustanding Postdoctoral Achievement lecture.)

L. Novotny, R. X. Bian, and X. S. Xie, "Near-Field Optical Trapping," Fifth International Conference on Near-Field Optics, Shirahama, Japan, Dec. 1998. (BES)

T. M. Orlando, "Quantum State-Resolved Desorption Studies of Wide Band-Gap Materials," Department of Physics, Rutgers University, Piscataway, N.J., Jan. 15, 1998.* (BES)

T. M. Orlando, "The Production of Atomic and Molecular Oxygen in Low Temperature Ice via Electronic Excitation," 2nd International Workshop on the Structure of Oxygen Radicals in Irradiated Solids, SORIS-98, Nieborow, Poland, May 30 – June 2, 1998.* (BES)

T. M. Orlando, "Quantum State-Resolved Desorption Studies of Wide Band-Gap Materials," Department of Physics and Astronomy, Nanophysics Laboratory, Univ. of Birmingham, Birmingham, England, June 8, 1998.* (BES)

T. M. Orlando, "Low-Energy Electron Interactions with Solids," Department of Earth and Geosciences, Stanford University, Palo Alto, Cal., Oct. 8, 1998.* (BES)

T. M. Orlando, "Low-Energy Electron Interactions with Solids from the Atomic to Astrophysical Scale," Argonne National Laboratory, Oct. 26, 1998.* (BES)

T. M. Orlando, "Low-Energy Electron Interactions with Solids from the Atomic to Astrophysical Scale," Department of Chemistry, Notre Dame University, Oct. 27, 1998.* (BES)

T. M. Orlando, "Low-Energy Electron Interactions with Solids from the Atomic to Astrophysical Scale," Catalysis Center, Northwestern University, Evanston, Ill., Oct. 29, 1998.* (BES)

T. M. Orlando, "Low-Energy Electron Interactions with Solids," Physical Chemistry Colloquium, Department of Chemistry, Johns Hopkins University, Baltimore, Nov. 3, 1998.* (BES)

T. M. Orlando, "Low-Energy Electron Interactions with Solids from the Atomic to Astrophysical Scale," Department of Engineering, University of Virginia, Charlottesville, Nov. 3, 1998.* (BES)

T. M. Orlando, M. T. Sieger, K. Briggman, and W. C. Simpson, "Quantum-Resolved Electron-Stimulated Interface Reactions," Twelfth International Workshop on Inelastic Ion–Surface Collisions, South Padre Island, Texas, Jan. 24–29, 1998.* (BES)

N. G. Petrik, A. B. Alexandrov, A. I. Vall, and T. M. Orlando, "Gamma Radiolysis of Water on Oxide Surfaces: Parameters Controlling the Energy Transfer," Surface Analysis '98 (20th Symposium on Applied Surface Analysis and 10th Annual Symposium of the Pacific Northwest Chapter, American Vacuum Society), Richland, Wash., June 16–19, 1998. (BES)

N. G. Petrik, A. B. Alexandrov, A. I. Vall, and T. M. Orlando, "Gamma Radiolysis of Water on Oxide Surfaces: Parameters Controlling the Energy Transfer," Gordon Research Conference on Radiation Chemistry, Newport, R.I., July 5–10, 1998. (BES)

N. G. Petrik, R. G. Tonkyn, W. C. Simpson, S. E. Barlow, and T. M. Orlando, "266-nm Laser Photolysis of a Liquid Water Jet," Gordon Research Conference on Radiation Chemistry, Newport, R.I., July 5–10, 1998. (BES)

D. Ray, "Structures and Energetics of Cation–Ether Clusters," Gordon Research Conference on Molecular and Ionic Clusters, Ventura, Cal., Jan. 1998.* (BES)

D. Ray, "Nonlinear Spectroscopy of Molecules at the Liquid/Vapor Interface of Water," XXIII Informal Conference on Photochemistry, Pasadena, Cal., May 30, 1998.* (BES)

D. Ray, L. X. Dang, J. L. Daschbach, B. C. Garrett, and G. K. Schenter, "Mass Transfer Between Phases: from Molecular Simulations of Interfaces to Macroscopic Models of Transport," American Physical Society, Los Angeles, Mar. 1998. (BES)

R. L. Sams, T. A. Blake, S. W. Sharpe, J.-M. Flaud, and W. J. Lafferty, "ν_{18} Spectral Region of $^{10}B^{11}BH_6$: Observation of the Dark State $\nu_5 + \nu_{10}$," Fifty-third Ohio State University International Symposium on Molecular Spectroscopy, Columbus, June 15–19, 1998. (EMSL Operations)

E. J. Sánchez, L. Novotny, and X. S. Xie, "A Novel Scheme for High Resolution Using an Illuminated Metal Tip," Fifth International Conference on Near-Field Optics, Shirahama, Japan, Dec. 1998. (BES)

S. W. Sharpe, J. F. Kelly, and J. Hartman, "High-Resolution (Doppler-Limited) Spectroscopy Using Quantum-Cascade Distributed-Feedback Lasers," Optical Society of America/CLEO '98, San Francisco, May 3, 1998.

S. W. Sharpe, J. Kelly, J. Hartman, F. Capasso, C. Gmachl, D. L. Sivco, A. Y. Cho, K. Namjou, S. Cai, and E. A. Whittaker, "Characterization of Distributed-Feedback Quantum-Cascade (QC) Lasers," Fifty-third Ohio State University International Symposium on Molecular Spectroscopy, Columbus, June 15–19, 1998.

M. T. Sieger, W. C. Simpson, and T. M. Orlando, "Stimulated Processes at Water–Ice Interfaces," American Physical Society, Los Angeles, Mar. 16-20, 1998.* (BES)

M. T. Sieger, W. C. Simpson, and T. M. Orlando, "Electron-Stimulated Desorption of D_2O Ice: Surface Structure and Electronic Excitations," Symposium on Interfacial Water, 215th American Chemical Society National Meeting, Dallas, Mar. 29 – Apr. 2, 1998.* (BES)

M. T. Sieger, W. C. Simpson, and T. M. Orlando, "Low-Energy Electron-Stimulated Production of O_2 in D_2O Ice," Surface Analysis '98 (20th Symposium on Applied Surface Analysis and 10th Annual Symposium of the Pacific Northwest Chapter, American Vacuum Society), Richland, Wash., June 16–19, 1998.* (BES)

M. T. Sieger, W. C. Simpson, and T. M. Orlando, "Low-Energy Electron Stimulated Processes in Nanoscale Ices," Gordon Research Conference on Radiation Chemistry, Newport, R.I., July 5–10, 1998. (BES)

M. T. Sieger, W. C. Simpson, G. K. Schenter, and T. M. Orlando, "Electron Interactions with Solid Surfaces: From the Astrophysical to the Atomic Scale," Virginia Commonwealth University, Richmond, Mar. 1998.* (BES)

M. T. Sieger, W. C. Simpson, G. K. Schenter, and T. M. Orlando, "Electron Interactions with Solid Surfaces: From the Astrophysical to the Atomic Scale," Washington State University, Pullman, Apr. 16, 1998.* (BES)

R. S. Smith, C. Huang, and B. D. Kay, "Thermodynamic Continuity and Mobility in Amorphous Solid Water: Evidence for the Existence of Supercooled Liquid Water," West Coast Theoretical Chemistry Conference, Richland, Wash., June 21–23, 1998.* (BES)

R. S. Smith, C. Huang, G. A. Kimmel, K. P. Stevenson, and B. D. Kay, "Thermodynamic Continuity and Mobility in Amorphous Solid Water: Evidence for the Existence of Supercooled Liquid Water," 215th American Chemical Society National Meeting, Symposium on Interfacial Water, Dallas, Mar. 29, 1998.* (BES)

R. S. Smith and B. D. Kay, "Determining the Self-Diffusivity in Amorphous Solid Water above the Glass Transition and Prior to Crystallization," Gordon Research Conference on Water and Aqueous Solutions, Holderness, N.H., Aug. 2–6, 1998 (poster). (BES)

R. S. Smith and B. D. Kay, "The Continuity Between Supercooled Liquid Water and Amorphous Solid Water," Symposium in Honor of C. Austen Angell, Pisa, Italy, Sept. 26, 1998.* (BES)

K. P. Stevenson, Z. Dohnalek, G. A. Kimmel, R. S. Smith, and B. D. Kay, "Surface Area and Porosity of Amorphous Solid Water Probed via N_2 Gas Adsorption and Temperature Programmed Desorption," Surface Analysis '98 (20th Symposium on Applied Surface Analysis and 10th Annual Symposium of the Pacific Northwest Chapter, American Vacuum Society), Richland, Wash., June 16–19, 1998. (BES)

K. P. Stevenson, Z. Dohnálek, G. A. Kimmel, R. S. Smith and B. D. Kay "A Study of Amorphous Solid Water (ASW) Morphology using N_2 Gas

Adsorption and Thermal Desorption," 45th International Meeting of the American Vacuum Society, Baltimore, November 2-6, 1998. (BES)

D. P. Taylor, W. C. Simpson, K. Knutsen, and T. M. Orlando, "Electron-and Photon-Stimulated Desorption Studies of Zirconia," American Physical Society, Los Angeles, March 16–20,1998. (BES)

M. D. Tinkle and S. E. Barlow, "Experimental Characterization of a Fourth-Order Cylindrical Penning Trap," American Society for Mass Spectrometry, Orlando, Fla., May 31, 1998. (BES)

L.-S. Wang, "Electronic Structure of Cold and Hot Al_n Clusters (n = 1–162) by Anion Photoelectron Spectroscopy: Nonmetal–Metal Transition, Electron Shell Structure, and Possible Solid–Liquid Transition," University of Washington, Seattle, given while a Visiting Fellow at the Atomic Clusters Program, Institute for Nuclear Theory, June 29 – July 10, 1998.*

L.-S. Wang, "Probing the Electronic Structure of Atomic Clusters Using Anion Photoelectron Spectroscopy," Gordon Research Conference on Electron Spectroscopy, Henniker, N.H., July 26, 1998.* (BES, EMSL)

L.-S. Wang, "Electronic Structure of Cold and Hot Al_n Clusters (n = 1–162) by Anion Photoelectron Spectroscopy: Nonmetal–Metal Transition, Electron Shell Structure, and Possible Solid–Liquid Transition," Institute of Physics and Chemistry of Materials, CNRS, Strasbourg, France, Aug. 28, 1998.*

L. S. Wang, "Transition Metal–Carbon Mixed Clusters by Photoelectron Spectroscopy," Naval Research Laboratory, Washington D.C., Sept. 29, 1998.*

L.-S. Wang, X. Li, X. Wang, and H. Wu, "New Magic Numbers in Ti_xC_y-Anion Clusters And Implications for the Growth Mechanisms of Titanium Carbide Clusters," Ninth International Symposium on Small Particles and Inorganic Clusters (ISSPIC-9), Lausanne, Switzerland, Sept. 1, 1998. (EMSL)

L.-S. Wang, X. Li, H. Wu, and X. Wang, "Observation Of *s-p* Hybridization and Electron Shell Structures in Aluminum Clusters Using Photoelectron Spectroscopy," Ninth International Symposium on Small Particles and Inorganic Clusters (ISSPIC-9), Lausanne, Switzerland, Sept. 1, 1998. (EMSL)

L.-S. Wang, H. Wu, X. Li, X. Wang, and C.-F. Ding, "$A1_3O_y$ (y = 0–5) Clusters: Sequential Oxidation, Metal-to-Oxide Transformation, and Photoisomerization," Ninth International Symposium on Small Particles and Inorganic Clusters (ISSPIC-9), Lausanne, Switzerland, Sept. 1, 1998. (BES)

X.-B. Wang, C.-F. Ding, and L.-S. Wang, "Photoelectron Spectroscopy of Multiply-Charged Anions," (poster), Gordon Research Conference on Electron Spectroscopy, Henniker, N.H., July 26, 1998. (BES, EMSL)

Z. Wang, D. M. Friedrich, A. G. Joly and K. A. Peterson, "The Ground State Proton-Transfer Tautomer of Salicylate Anion," 216th American Chemical Society National Meeting, Boston, Aug. 23–27, 1998.

R. M. Williams, K. M. Beck, W. P. Hess, and J. T. Dickinson, "Femtosecond and Nanosecond Laser Induced Desorption from Ionic Solids," Gordon Research Conference on Laser Interactions with Materials, Andover, N.H., June 8–12, 1998. (BES)

X. S. Xie, "Applications of Single-Molecule Spectroscopy and Microscopy to Photochemistry Research," 22nd Solar Photochemistry Research Conference, Washington D.C., June 1998.* (BES)

X. S. Xie, "Imaging, Spectroscopy and Dynamics of Single Proteins, Single Cells, and Biological Membranes," Symposium on Near-Field Nano-Optics, Osaka, Japan, June 30 – July 2, 1998.* (BES, NABIR)

X. S. Xie and H. P. Lu, "Spectral and Chemical Behaviors of Single Enzyme Molecules," US–Japan Cooperative Workshop on Photoconversion and Photosynthesis, Napa Valley, Cal., Jan. 1998.* (BES, NABIR)

X. S. Xie and H. P. Lu, "Chemical and Conformational Dynamics of Single Flavoenzyme Molecules," American Physical Society, Los Angeles, Mar. 1998.* (BES, NABIR)

X. S. Xie and H. P. Lu, "Probing Single-Molecule Electron Transfer," Gordon Conference on Electron Donor– Acceptor Interactions, Newport, R.I., Aug. 1998.* (BES)

X. S. Xie and H. P. Lu, "Probing Chemistry of Single Molecules," First Annual Symposium on Chinese–American Frontiers of Science, Irvine, Cal., Aug. 1998.* (BES, NABIR)

X. S. Xie, H. P. Lu, E. J. Sánchez, L. Novotny, D. C. Arnett, A. Zumbusch, and G. R. Holtom, "Imaging, Spectroscopy and Dynamics of Single Enzyme Molecules and Biological Membranes," Gordon Conference on Macromolecular Organization and Cell Function, Queens College, Oxford, England, Sept. 13–18, 1998. (BES)

X. S. Xie, H. P. Lu, and L. Xun, "Probing Dynamics of Single Enzyme Molecules," 216th American Chemical Society National Meeting, Boston, Aug. 23–27, 1998.* (BES)

X. S. Xie, E. J. Sánchez, L. Novotny, D. Arnett, and G. R. Holtom, "New Developments of Two-Photon Microscopy," Focus on Microscopy 1998, Sydney, Australia, Apr. 1998. (BES)

X. S. Xie, E. J. Sánchez, L. Novotny, D. Arnett, and G. R. Holtom, "New Developments of Two-Photon Microscopy," Workshop on Multiphoton Microscopy, MSA, Atlanta, July 1998.* (BES)

X. S. Xie, E. J. Sánchez, L. Novotny, D. Arnett, and G. R. Holtom, "Imaging and Spectroscopy of Single Molecules by Two-Photon Excitation," Annual Meeting, Optical Society of America, Baltimore, Oct. 4–9, 1998.* (BES)

Honors and Recognition

Steve Barlow was recognized on Technology Transfer Day, March 26, 1998, for his achievement in the creation and transfer of science and technology, as co-inventor of an Asymmetric Ion Trap, U.S. Patent 5,693,941.

Ken Beck was nominated by NSF for a Japanese Science Technology Agency short-term fellowship for a research collaboration at Tsukuba Science City, based on a proposal entitled "The Preparation and Characterization of Functional Nanocomposite Films by Laser Ablation." He had a visiting appointment at Tsukuba March–May 1998.

Steve Joyce assumed the past chair of the Pacific Northwest Section, American Vacuum Society, in January 1998. He also serves on the AVS Surface Science Executive Committee.

Bruce Kay organized a symposium on "Interfacial Water" at the 215th National Meeting, American Chemical Society, Dallas, March 29–31; and a workshop on "Ice Physics and Chemistry and the Environment," Richland, Wash., Aug., 13–14, 1998.

Bruce Kay was elected Vice Chairman for 1999 and Chairman for 2001 of the Gordon Conference on Dynamics at Surfaces.

Bruce Kay was appointed Affiliate Professor of Chemical Engineering, University of Washington, September 1998.

The paper "Single-Molecule Enzymatic Dynamics" by **Peter Lu**, Luying Xun, and **Sunney Xie** [*Science* **282**, 1877 (1998)] was featured in "This Week in Science," *ibid.*, 1781.

Rod McDowell was appointed to a four-year term as a Titular Member of the International Union of Pure and Applied Chemistry's Commission I.5 (Physical Chemistry Division, Commission on Molecular Structure and Spectroscopy) starting January 1998. He is responsible for preparing for publication a IUPAC Recommendations document, *Notations and Conventions in Molecular Spectroscopy: Part 4. Vibrational-Rotational Spectroscopy*.

Matt Sieger received the 1998 M. T. Thomas Award for Outstanding Postdoctoral Achievement, recognizing significant scientific contributions to projects relevant to the EMSL mission. He received a cash prize and his name has been added to a plaque in the EMSL lobby. The citation reads, "For his research on electron-stimulated desorption from environmentally important interfaces, and for the theoretical and experimental development of new surface probe techniques based on electron standing waves."

Under the title "Experiments clarify O_2 production on icy moons," the paper by **M. T. Sieger, W. C. Simpson**, and **T. M. Orlando**, "Production of O_2 on Icy Satellites by Electronic Excitation of Low-Temperature Water Ice," *Nature* **394**, 554 (1998), was featured in *Chemical & Engineering News'* "Science/Technology Concentrates," Aug. 17, 1998, p. 37.

Lai-Sheng Wang was awarded the Washington State University Westinghouse Distinguished Professorship in Materials Science and Engineering for the 1997–1998 academic year, in recognition of his pioneering work in the synthesis and characterization of novel clusters of oxide materials.

Lai-Sheng Wang was promoted to Associate Professor with tenure by Washington State University, March 1998.

Visitors

George Flynn, Columbia University
Seminar (Jan. 6): "STM of Physisorbed Molecules Self-Assembled at the Liquid-Solid Interface."

Peter Griffiths, University of Idaho
Seminar (Feb. 4) : "Data Processing Techniques for Open-Path FT-IR Atmospheric Monitoring."

Richard E. Palmer, University of Birmingham
Seminar (March 13): "Negative Ion Resonances and the 'Electronic Catalyst.'"

Tony Heinz, Columbia University
Seminar (March 20): "Surface Chemistry at High Electronic Temperatures: Inducing Surface Processes by Femtosecond Laser Radiation."

Christoph Bräuchle, Ludwig-Maximilians-Universität, Munich
Seminar (March 23): "Single Molecule Spectroscopy: Some Examples of Low Temperature High Resolution Spectroscopy and Room Temperature Confocal Microscopy."

G. Wilse Robinson, Texas Tech University
Seminar (April 13): "The Decisive Role of Outer Bonding in the Molecular-Level Understanding of Liquid Water."

Dan Imre, Brookhaven National Laboratory
Seminar (April 21): "Phase Transformation in Atmospheric Aerosols: Why Are the Models So Far Off?"

Louis J. Terminello, Lawrence Livermore National Laboratory
Seminar (April 28): "Materials Characterization with Soft X-Rays: Atomic, Electronic and Bonding Structural Information."

Gerard Parkin, Columbia University
Seminar (April 29): "Synthetic Analogues for Zinc Enzymes, The Phenomenon of Bond Stretch Isomerism and the Perils of a Polar Axis."

Shihe Yang, Hong Kong University
Seminar (May 1): "Resonant Two-Photon Ionization Spectroscopy of van der Waals Complexes with Aromatic Chromophores."

Stephen Schwartz, Brookhaven National Laboratory
Seminar (May 12): "Aerosols and Climate: Monkey Wrench or Knob?"

Jeff Gaffney, Argonne National Laboratory
Seminar (July 14): "Instrumentation Development of Peroxyacetyl Nitrates (PANs), Nitrogen Dioxide and Hydrocarbons Using Luminol and Ozone Chemiluminescent Detection."
Seminar (July 15): "DOE/OBER Global Change Education Program (GCEP): Some Recent Developments."

Nancy Marley, Argonne National Laboratory
Seminar (July 14): "Optical Properties of Atmospheric Aerosols."

Thomas Gouder, European Institute for Transuranium Elements, Karlsruhe, Germany
Seminar (Aug. 14): "Surface and Thin Film Research on Actinides."

Mark Johnson, Yale University
Seminar (Aug. 17): "Structural Aspects of Anionic Hydration via Cluster Ion Vibrational Spectroscopy."

Thomas McCord, University of Hawaii
Seminar (Oct. 14): "Surface Composition of the Icy Galilean Satellites from the NASA Galileo Mission to Jupiter."

Trevor J. Sears, Brookhaven National Laboratory
Seminar (Nov. 20): "High Sensitivity and High Resolution: New Techniques in Laser Absorption Spectroscopy."

Collaborations

External Collaborations

Type of collaborator: (1) = non-visiting; (2) = short-term (<1 month); (3) = long-term (≥1 month).

S. E. Barlow
Oak Ridge National Laboratory (S. Nunn) (1)
Vehicle Exhaust Treatment

S. E. Barlow
Institute of Inorganic Chemistry, Siberian Branch, Russian Academy of Sciences, Novosibirsk (V. Mikheev and V. Pervukhin) (3)
Nucleation in Atmospheric Chemistry

K. M. Beck
University of Central Florida (R. Peale, PASS Affiliated Scientist) (3)
Optically Detected Magnetic Resonance (ODMR) and Time-Resolved FTIR of Immobilized Heavy Metals on Calcite Surfaces

K. M. Beck
National Institute of Materials and Chemical Research, Japan (T. Sasaki) (3)
Preparation and Characterization of Pt/SiO_2 and Pt/MgO Functional Nanocomposite Films by Laser Ablation

J. P. Cowin
University of Colorado (G. B. Ellison) (2)
Soft-Landing Ions

J. P. Cowin
Washington State University (M. Dresser) and Associated Western Universities (D. Doering) (2)
Ferroelectric Ice

J. P. Cowin
Arrowhead University (M. C. Gallagher) (1)
Thin-Film Al_2O_3

J. P. Cowin
Washington State University (B. Pate) (2)
Soft-Landing Ion Studies

W. P. Hess
Vanderbilt University (R. F. Haglund, Jr.) (1)
Studies of Laser/Solids Interactions

W. P. Hess
University of Colorado (G. B. Ellison) (1,2)
Photochemistry of Thin Molecular Films

W. P. Hess
Washington State University (J. T. Dickinson) (1,2)
Laser Ablation Characterization of Solids

W. P. Hess
University of Central Florida (R. Peale); National Institute for Materials Center (NIMC), Tsukuba, Japan (T. Sasaki); Princeton University (S. Bernasek) (1,2)
Reaction of Metal–Oxide Materials

W. P. Hess
University of Washington (J. Rehr) (1)
EXAFS Studies of Metal Ions in Caliche

W. P. Hess
Jet Propulsion Laboratory (G. Cardell) (1,2)
Laser Ablation for Isotope Determination

A. G. Joly
Washington State University (K. A. Peterson) (1)
Montana State University (P. R. Callis) (1)
Structure of the Proton Transfer Tautomer of Salicylate

A. G. Joly
State University of New York, Buffalo (M. Na and H. Luo) (2)
Enhancement of Catalytic Properties using Surface and Interface Engineering

A. G. Joly
University of Idaho (R. von Wandruszka, M. McCarroll) (2)
Time-Resolved Fluorescence Anisotropies in Mixed Surfactant Solutions

S. A. Joyce
Tulane University (U. Diebold) (2)
Structure and Chemistry of Metal Oxides

B. D. Kay
University of Washington (Hannes Jonsson) (1)
Growth, Structure, and Reactivity of Amorphous Ice

T. M. Orlando
Argonne National Laboratory (D. Meisel) (1)
Interfacial Radiolysis Effects in Tank Waste Speciation

T. M. Orlando
University of Sherbrooke (L. Sanche) (1)
Low-Energy Electron Interactions with Molecular Films

T. M. Orlando
Istituto di Struttura della Materia, CNR, Frascati, Rome (N. Zema, E. Papparazzo) and University of Rome (M. Piancentini) (1)
Photon-Stimulated Desorption from Alkali Halides

T. M. Orlando
Research Institute of Complex Power Technology (VNIPIET), St. Petersburg (N. G. Petrik, A. Alexandrov) (3)
Laser-Stimulated Luminescence

T. M. Orlando
University of Birmingham (R. Palmer) (1)
Electron-Stimulated Desorption of Physisorbed O_2

T. M. Orlando and J. P. Cowin
Rutgers University (T. E. Madey), Brookhaven National Laboratory (P. E. Haustein), and University of California, Riverside (J. Yarmoff) (1)
Radiolytic and Thermal Processes Relevant to Dry Storage of Spent Nuclear Fuels

T. M. Orlando, R. G. Tonkyn, and S. E. Barlow
Ford Motor Company (J. Hoard) and General Motors Company (T. M. Sloane) (1)
Vehicle Exhaust Treatment Using Electrical Discharge and Materials Chemistry

D. Ray
University of Utah (P. B. Armentrout) (1)
Gas-Phase Cation–Ether Complexes

S. W. Sharpe
Oregon State University (J. W. Nibler) (2)
Jet Spectroscopy of Metal Borohydrides

S. W. Sharpe
State University of New York at Stony Brook (P. Varanasi) (1)
High-Resolution Infrared Spectroscopy of Atmospheric Interest

S. W. Sharpe
University of Colorado (V. Vaida) (2)
Spectroscopy of Water Clusters and Small Droplets: Relevance to Atmospheric Radiative Transfer

S. W. Sharpe
Sandia National Laboratory (P. Hargis) (2)
Atmospheric Hydrolysis Chemistry

S. W. Sharpe
Wesleyan University (S. E. Novick) (1)
High-Resolution Spectroscopy of Hydrogen-Bonded Dimers

S. W. Sharpe and T. A. Blake
National Institute for Standards and Technology (G. T. Fraser and W. J. Lafferty) (1)
Rovibrational Spectral Analysis of Molecules and Molecular Clusters

R. G. Tonkyn
Delphi Energy and Engine Management Systems, Flint, Mich. (T. Silvus) (2)
Vehicle Exhaust Treatment

L. S. Wang
Air Products and Chemicals, Inc., Allentown, Pa. (H. S. Chen) (1)
Combined Density Functional and Experimental Studies of Transition-Metal Clusters

L. S. Wang
Harvard University (R. H. Holm) (1)
Electronic Structures of Fe–S Cluster Analogs Important in Fe–S Proteins

L. S. Wang
Princeton University, Materials Institute (S. K. Nayak) (1)
Theoretical and Experimental Studies of Aluminum Oxide Clusters

L. S. Wang
University of Utah (J. Simon and A. I. Boldyrev) (1)
Experimental and Theoretical Studies of Superhalogens and Hypervalent Molecules

L. S. Wang
University of Jyvaskyla, Finland (M. Manninen) (1)
Theoretical Simulations and Temperature-Dependent Studies of Aluminum Clusters

L. S. Wang
Virginia Commonwealth University (P. Jena and B. Rao) (1)
Theoretical and Experimental Studies of Aluminum Nitride and Aluminum Clusters

L. S. Wang
Washington State University (X. Li) (3)
Photoelectron Spectroscopy of Clusters

L. S. Wang
Washington State University (C.-F. Ding) (3)
Study of Solvated Clusters

L. S. Wang
Washington State University (X. B. Wang) (3)
Photoelectron Spectroscopy of Met-Cars

L. S. Wang
Washington State University (H. Wu) (3)
Electronic Structure of Transition-Metal Clusters

X. S. Xie
University of Sheffield, England (N. Hunter) (1)
Single-Molecule Studies of Light-Harvesting Complexes and Single-Cell Studies of Biogenesis of photosynthetic membrane

X. S. Xie
Washington State University (L. Xun) (1)
Single-Molecule Studies of Biodegrading Enzymes

X. S. Xie
University of Kansas (C. Johnson) (3)
Single-Molecule Studies of Protein Conformational Motions

X. S. Xie
Institut für Physikalische Chemie, Ludwig-Maximilians Universität München, Munich (A. Zumbusch) (3)
Nonlinear Optical Imaging

Collaborations within PNNL

S. E. Barlow
EHSD Materials and Chemical Sciences Department, Nuclear Chemistry Section (A. J. Peurrung)
Stabilization of Nonneutral Plasmas

S. D. Colson
Staff throughout PNNL (L. G. Morgan, J. Janata, J. G. Hill, M. S. Hanson, and R. E. Gephart)
Hanford Tank Characterization and Safety Issue Resolution Project

S. D. Colson and R. S. McDowell
Energy Division, Engineering and Analytical Sciences Department, Sensors and Measurement Systems Section (J. S. Hartman); and EHSD Materials and Chemical Sciences Department, Atomic and Molecular Chemistry Section (M. L. Alexander)
Waste Tank Speciation Methods

J. P. Cowin
Atmospheric Sciences Department (R. S. Disselkamp, C. M. Berkowitz); Battelle Columbus (C. W. Spicer); Atmospheric and Environmental Research, Inc., Boston (Y. Zhang); Argonne National Laboratory (C. Bishop)
Effects of Heterogeneous Chemistry on NO_y in the Troposphere

J. P. Cowin and T. M. Orlando
Environment, Safety and Health Division, Radiological Control Group (S. C. Marschman)
Dehydration and Radiolysis of Spent Nuclear Fuels

W. P. Hess
EHSD Analytical Chemistry Resources, Advanced Organic & Analytical Methods (J. A. Campbell and S. C. Goheen)
Laser Ablation Characterization of Solids

W. P. Hess
EMSL Theory, Modeling, and Simulation (M. I. McCarthy, S. S. Xantheas, and J. D. Myers)
Studies of Laser/Solid Interactions

A. G. Joly
EMSL Interfacial and Processing Science (Y. Liang, J. L. Daschbach, and D. R. Baer)
Enhancement of Catalytic Properties using Surface and Interface Engineering

A. G. Joly
EMSL Environmental Dynamics & Simulation (D. M. Friedrich, Z. Wang, and P. L. Gassman)
Structure of the Proton Transfer Tautomer of Salicylate; Phenanthrene Distribution and Desorption in Porous Silica

S. A. Joyce
EHSD Materials Resources, Molecular and Solid State Research (G. Exarhos)
Physics and Chemistry of Ceramic Surfaces

S. A. Joyce
EMSL Interfacial and Processing Science (M. A. Henderson); and EHSD Earth Systems Sciences Department, Thermodynamic and Molecular Geochemistry Group (J. R. Rustad)
Surface Chemistry of Iron Oxides

S. A. Joyce
EMSL Interfacial and Processing Science (S. A. Chambers)
Contaminant Interactions with Iron and Manganese Oxides

B. D. Kay
EMSL Interfacial and Processing Science (C. H. F. Peden)
Physics and Chemistry of Ceramic Surfaces

T. M. Orlando
EHSD Materials and Chemical Sciences Department, Atomic and Molecular Chemistry Section (D. M. Camaioni)
Tank Waste Chemistry

T. M. Orlando
Environmental and Health Sciences Division, Materials Group (M. L. Balmer)
Plasma-Activated Surface Catalysis

D. Ray
EMSL Theory, Modeling, and Simulation (D. F. Feller)
Gas-Phase Cation–Ether Complexes

D. Ray
EMSL Theory, Modeling, and Simulation (B. C. Garrett, G. K. Schenter) and Interfacial and Processing Science (J. L. Daschbach)
Transport Across Liquid Interfaces

S. W. Sharpe
National Security Division (R. G. Clemmer and S. W. Martin)
Standoff Infrared Sensors for Detection of Clandestine Methamphetamine Production

S. W. Sharpe
Energy Division, Engineering and Analytical Sciences Department, Sensors and Measurement Systems Section (J. S. Hartman) (1)
Development of Infrared Sniffer System

S. W. Sharpe
Energy Division, Engineering and Analytical Sciences Department, Sensors and Measurement Systems Section (J. W. Griffin)
Infrared Analysis in Head-Space Sampling for Paper and Pulp Digesters

S. W. Sharpe
Energy Division, Engineering and Analytical Sciences Department, Sensors and Measurement Systems Section (J. S. Hartman and M. A. Khaleel)
Sensors and Modeling for Auto Glass Production

S. W. Sharpe
Energy Division, Engineering and Analytical Sciences Department, Sensors and Measurement Systems Group (J. F. Kelly) (2)
Spectroscopic Techniques for Atmospheric Monitoring

L. S. Wang and S. D. Colson
EMSL Theory, Modeling, and Simulation (J. B. Nicholas)
Cluster Model Studies of Environmentally-Important Oxide Clusters

X. S. Xie
Atmospheric Sciences Department (R. X. Bian)
Near-Field Optical Tweezers Manipulation of Enzymatic Reactions on Biological Membranes

X. S. Xie
EMSL Theory, Modeling, and Simulation (G. K. Schenter)
Theory of Single-Enzyme Dynamics

Acronyms and Abbreviations

ACS	American Chemical Society
APC	allophycocyanin
ARM	Atmospheric Radiation Measurement Program
ASMS	American Society for Mass Spectrometry
ASW	amorphous solid water
AVS	American Vacuum Society
AWU	Associated Western Universities
BES	DOE Office of Basic Energy Sciences
BET	Brunauer–Emmett–Teller
BL	bilayer
CARS	coherent anti-Stokes Raman spectroscopy
CFHC	chlorofluorohydrocarbon
CI	crystalline ice
CID	collision-induced dissociation
CLEO	Conference on Lasers and Electro-Optics
COE	Cooperative Office Education
COx	cholesterol ocidase
CRADA	Cooperative Research and Development Agreement
CS&D	Chemical Structure and Dynamics
cw	continuous-wave
DC	direct current
DFB	distributed feedback
DNA	deoxyribonucleic acid
DOE	U. S. Department of Energy
DOS	density of states
EA	electron affinity
EDTA	ethylenediaminetetraacetic acid
EELS	electron energy-loss spectroscopy
EHSD	Environmental and Health Sciences Division
EMSL	William R. Wiley Environmental Molecular Sciences Laboratory
EMSP	DOE Environmental Management Science Program
EPR	electron paramagnetic resonance
ESD	electron-stimulated desorption
ESW	electron standing wave
ETH	Swiss Federal Institute of Technology
EXAFS	extended X-ray absorption fine structure
FAD	flavin adenine dinucleotide
FC	fluorocarbon
FIB	focused ion beam
FM	frequency modulation
FTICR	Fourier-transform ion cyclotron resonance
FTIR	Fourier-transform infrared
FTIRS	Fourier-transform infrared spectroscopy/spectrometer
fwhm	full width at half maximum
GCEP	Global Change Education Program
ICR	ion cyclotron resonance
IR	infrared
IUPAC	International Union of Pure and Applied Chemistry
JILA	Joint Institute for Laboratory Astrophysics, Boulder
KDP	potassium dihydrogen phosphate
LAMS	laser-assisted mass spectrometry
LDRD	Laboratory Directed Research and Development
LDS	liquid droplet source
LHS	light-harvesting complex
LIDAR	laser infrared radar
LSL	laser-stimulated luminescence
MALDI	matrix-assisted laser desorption–ionization
MBE	molecular-beam epitaxy
MCH	methyl cyclohexane
ML	monolayer
MMP	multiple monopole
MPI	multiphoton ionization
MS	mass spectrometer/spectrometry
MW	molecular weight
NABIR	Natural and Accelerated Bioremediation Research
NASA	National Aeronautics and Space Administration
NATO	North Atlantic Treaty Organization
NEA	noise-equivalent absorbance
NIMC	National Institute for Materials Center, Tsukuba, Japan
NMR	nuclear magnetic resonance
NN	DOE Office of Nonproliferation and National Security
NRC	National Research Council
NSF	National Science Foundation
OBER	DOE Office of Biological and Environmental Research
ODMR	optically detected magnetic resonance
PAN	peroxyacetyl nitrate
PASS	PNNL Affiliate Staff Scientist
PES	photoelectron spectroscopy
PIC	pseudo-isocyanine
PLD	pulsed laser deposition
PNNL	Pacific Northwest National Laboratory
P-P	peak-to-peak
ppm	parts per million
PSD	photon-stimulated desorption
PVS	polyvinyl sulfate

QC	quantum cascade
QMS	quadrupole mass spectrometer
RCB	repulsive Coulomb barrier
RCS	rotational coherence spectroscopy
REMPI	resonance-enhanced multiphoton ionization
rf	radiofrequency
SABIT	Special American Business Internship Training Program
SERDP	Strategic Environmental Research and Development Program
SPIE	Society of Photo-Optical and Instrumentation Engineers
STM	scanning tunneling microscopy/microscope
TEM	transmission electron microscopy
TOF	time-of-flight
TPD	temperature-programmed desorption
UHV	ultra high vacuum
USCAR	U.S. Council for Automotive Research
UV	ultraviolet
VNIPIET	Russian Research Institute of Complex Power Technology
XPS	X-ray photoelectron spectroscopy
XRD	X-ray diffraction
YAG	yttrium aluminum garnet
YSZ	yttria-stabilized cubic zirconia

Where CS&D Fits in PNNL

- Pacific Northwest National Laboratory (W. J. Madia, *Director*)
  - Energy Technology Division (*vacant, Associate Laboratory Director*)
  - **Environmental and Health Sciences Division** (G. M. Stokes, *Associate Laboratory Director*)
    - Analytical Chemistry Resources (J. F. Wacker)
    - Atmospheric Sciences and Global Change Resources (W. T. Pennell)
    - Biogeochemistry Resources (H. Bolton Jr.)
    - Materials Resources (M. R. Thompson)
    - Molecular Biosciences Resources (R. A. Walters)
    - Statistics Resources (B. A. Pulsipher)
    - **W. R. Wiley Environmental Molecular Sciences Laboratory (EMSL)** (J. H. Futrell, *Director*)
      - **Chemical Structure and Dynamics (CS&D)** (S. D. Colson)
      - Interfacial Processing Science (IPS) (C. H. F. Peden)
      - Macromolecular Structure and Dynamics (MS&D) (D. W. Koppenaal)
      - Theory, Modeling, and Simulation (TM&S) (D. A. Dixon)
      - Environmental Dynamics and Simulation (ED&S) (J. M. Zachara)
      - Computing and Information Sciences (C&IS) (R. A. Bair)
  - Environmental Technology Division (B. D. Shipp, *Associate Laboratory Director*)
  - National Security Division (M. Kluse, *Associate Laboratory Director*)